Research & Development

2018

Mechanical Engineering Letters, Szent István University

Annual Technical-Scientific Journal of the Mechanical Engineering Faculty,
Szent István University, Gödöllő, Hungary

HU ISSN 2060-3789

Páter K. u. 1., Gödöllő, H-2103 Hungary
dekan@gek.szie.hu, www.gek.szie.hu,
Volume 17 (2018)

Contents

Institute for Environmental Engineering Systems

Dr. István SERES
Director of the Institute

Dear Reader,

The structure of the Institute for Environmental Engineering Systems has been changed in the last time period, as beside the two traditional departments, the Department of Environmental and Building Engineering and the Department of Physics and Process Control, the Department of Mathematics became also the part of the Institute. This fact opened new possibilities of the cooperation in the field of the education (the Mathematics and Physics education can help each other more strongly) and in the research as well. Fortunately, already there are common projects of the Departments as well, for example a project of the maintenance of talented students in the Mathematics and Physics education.

This improving cooperation can be observed also in the research activities as well, for example one of the published articles came to the light in the cooperation of a mathematician and an engineer. Another important task to maintain the national and international cooperation between the partner institutes. As a matter of fact, the institute members enjoy good relations with several foreigner partners. One of the publications has been realized as a result of a Hungarian – Indonesian cooperation.

Form the results of the current research activity the following topics are selected out to publish in the recent issue of the MEL Journal:

Effect of cooling on the performance of a small-scale solar power plant system – In this research, the cooling system of the 1 kWp solar power plant have been realized and tested in order to maintain the cell temperature of the PV module. Based on the test, it has been shown that the efficiency of PV without cooling system is about 1.5% lower than the same for the cooled system (without cooling: 9.21%, average cell temperature 32.2 ^{o}C, with cooling: 10.64 %, average cell temperature of 31.3 ^{o}C).

Environmental and healthcare risks of refrigerants – This paper deals with the application of refrigerant in the industry. The most important cooling systems and refrigerants, their application range in temperature, their properties and risk factors to the environment and health is shown. Special attention is paid to the natural refrigerant and the new risk factors that they present.

Efficiency of heat performance in embedded water-based heating systems with mortar discontinuity – In this paper the efficiency of heat transfer of systems installed with mortar discontinuities behind the heating pipes creating

air gaps is investigated. In the model basic building structure with errors was used to analyze the impact of discrepancies. Numerical simulations and calculations show that air gaps do not cause significant performance drop.

Comparison of water and paraffin for heat storage – In this work the possibility of using Phase-change materials (PCM) for heat storage was investigated. During the research measurements were carried out to determine the thermal properties of the PCM. The results and their comparison with literature data are also presented.

Measurements of the grid quality for PV inverters – In this study the quality of the AC voltage produced by inverters is investigated. A data logger circuit was developed by National Instrument units to measure the voltage – time function of the electric grid, and the voltage function generated by different inverters. The measurement results and the analysis of them are presented in the paper.

Comparison of water and paraffin for heat storage

Szabolcs BŐDI[1], Piroska VÍG[2], István FARKAS[2]
[1]Department of Natural Sciences and Engineering
Neumann János University, Kecskemét
[2]Department of Physics and Process Control,
Institute for Environmental Engineering Systems

Abstract

Phase-change materials (PCM) initially absorb heat during the temperature increase, absorb latent heat and melt when their temperature reaches the melting temperature. In this work calorimeter was used to measure the temperature of solid paraffin and change in the temperature of hot water as a function of time. The main goal was experimentally determining the relative heat storage capability of paraffin, and the equivalent amount of water for the same heat storage. The results have been also compared with the literature data.

Keywords

phase-change materials, measurements, calorimetry, solar energy

1. Introduction

The environmental impacts of fossil fuels energy resources and the increase in energy consumption have led researchers to study the use of renewable energy sources. For this reason, great attention is paid to solar energy as it is clean, non-polluting and inexhaustible. However, the availability of solar energy does not always guarantee its use, irregular and intermittent (Elbahjaoui *et al.,* 2018). Therefore, new energy technologies that improve energy efficiency are at the heart of current and future research. The difference between energy supply and energy demand can be offset by the storage of thermal energy in space and time. Energy systems with heat storage are more efficient and more sustainable than conventional energy systems (Meng *et a.,l* 2017).

Thermal energy storage methods include sensible thermal energy storage, latent thermal energy storage (LTES), and chemical energy storage. Different types of thermal energy storage systems can easily be applied to the sensible heat storage, easy to implement and maintain due to their simplicity. However, their use is limited due to the amount of heat that affects the energy efficiency of the energy system. Latent heat storages (LHS) store energy during melting or evaporation using a material phase change process without significant change in temperature. Such materials are called phase change materials. Their energy density is generally higher than that of sensible heat storage (SHS). The purpose

of latent heat storage is to use the heat storage in the desired operating temperature range by converting the physical state of the material from one state to another (solid liquid or liquid gas) (Preet *et al* 2017, Zeinelabdein *et al.,* 2018). In practice, LHS systems are used in a number of places, such as solar energy recovery systems, air conditioning systems for buildings, agricultural drying, waste heat recovery systems (Khan *et al.,* 2017).

In the recent work we started our research on the efficiency of heat storage with the help of phase change materials. After conducting complex literature research by studying several articles and professional books, we found that trends indicate that among the various phase change materials, solid paraffin wax (Paraffinum solidum) as a phase change material for solar energy systems for heat storage, cooling, and efficiency improvement.

Using the experience of previous literature, we investigated the properties of paraffin, which leads me to draw conclusions from solar energy systems for use in heat storage and cooling for photovoltaic/photothermal systems. During our examinations we measured the temperature of different paraffin masses as a function of time, on the basis of which we determined the amount of heat stored by each mass. According to the law of energy conservation, the heat released by the water is the same as the heat absorbed by the paraffin.

We could not directly determine the heat absorbed by the paraffin, because we were unable accurately to determine the beginning and the end of the melt. The specific and melting heats of the paraffin depending also on its composition, so the amount of heat released by the water in was determined during the process. The mass of water was determined that could be substituted the paraffin for heat storage. The experiments have been performed with different amount (1-15 g) of paraffin samples. During the final evaluation the results were recalculated into relative units based on 1 g paraffin. In such a way, a comparison with literature available data can be fulfilled.

2. Experimental setup and results

For the measurement of paraffin masses, which were put into self-adhesive bags, we used a Sartorius MA 30 digital balance (ID MA 30, 80702496). The weighing range is 20 g, with an accuracy of 0.001 g. The masses were measured in 1 g, 5 g, 8 g, 10 g and 15 g packages (Figure 1).

The temperature of the paraffin and the hot water was measured in a calorimeter. The water value of the calorimeter was 8 g based on previous measurements. For better heat storage, the calorimeter was placed in a closed hungarocell box.

The measurement of the hot water mass was carried out using a digital kitchen scale supplied by HAUSER® (DKS-1064W) with a measurement limit of 5 kg and an accuracy of 0.1 g. We used thermocouples to measure temperatures. The data acquisition system was the ADAM-4018 module, which collected the data and was recorded in digital form (Figure 2).

Figure 1. Sartorius MA30 digital scale and paraffin masses used for measurements

Figure 2. The calorimeter with the sensors in the hungarocell box and the data acquisition system

Figure 3 shows the change in water or paraffin temperature vs time. The lower purple curve shows the change in paraffin temperature as a function of time, and the blue curve shows the change in water temperature as a function of time. The amount of heat stored was measured in the range where the temperature of the paraffin varies between 40 °C and 65 °C. We have taken measurements where the melting of paraffin ends at 65 °C, otherwise it is not possible to count the melting heat.

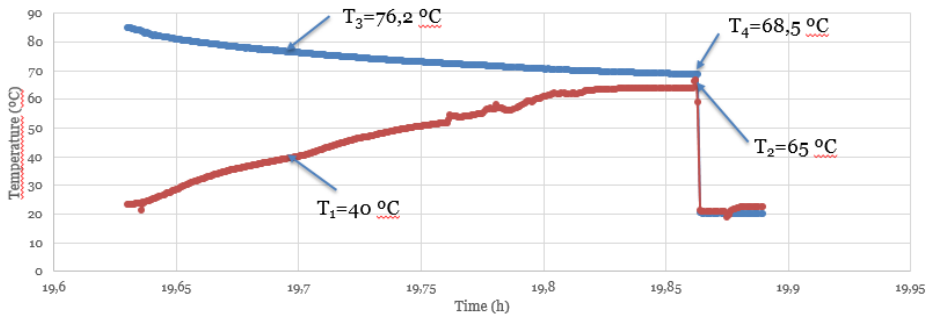

Figure 3. Changes in water and paraffin temperature as a function of time

The amount of the heat storage can be calculated as follws:

$$Q_{st} = (\, m_{hot\ water} + m_{wv})\, c_{water}\, \Delta T_{water}\ , \tag{1}$$

where:
Q_{st} – the heat storage, J
$m_{hot\ water}$ – the mass of hot water, kg
m_{wv} – the water value of the calorimeter, kg
c_{water} – the specific heat of the water,$Jkg^{-1}K^{-1}$
ΔT_{water} – temperature difference of the water, K

Figure 4 shows the average heat storage as a function of paraffin masses.

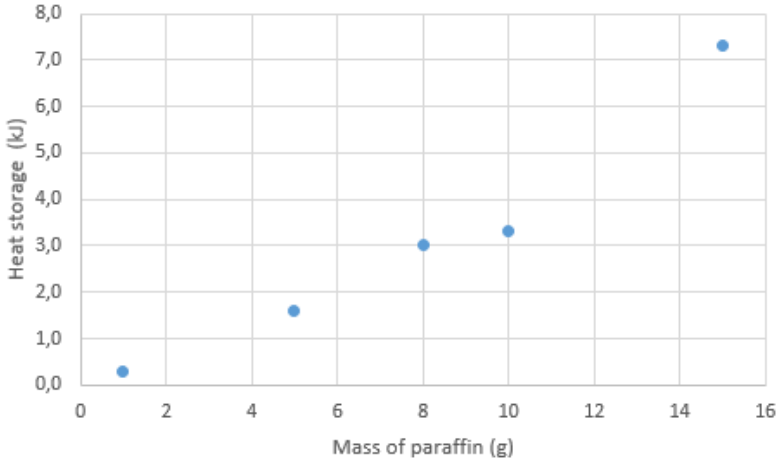

Figure 4. The average heat storage as a function of paraffin masses

Measuring errors can occur if the self-adhesive bag is not completely closed or the sensor may touch the bag, so it measures the temperature of the bag and not exactly the paraffin. It may also cause uncertainty as to whether the sensor measures the temperature of the molten paraffin or the solid state at the given time.

The heat storage can be replaced with water of the following mass:

$$m_{water} = \frac{Q_{st}}{c_{water} \Delta T_{par}}\ , \tag{2}$$

where:
m_{water} – the mass of water substituting paraffin, kg
ΔT_{par} – the temperature difference of paraffin, K

Table 1 shows the mass of paraffin and the mass of water substituting paraffin.

Table 1. Mass of paraffin and the mass of water substituting paraffin

m_{par} (g)	m_{water} (g)
1	2,94
5	15,45
8	28,33
10	31,66
15	69,85

Table 2 shoes the heat storage values per 1 g.

Table 2. Mass of paraffin and the heat storage per 1 g

m_{par} (g)	Heat storage per 1 g (kJ/g)
1	0,31
5	0,32
8	0,37
10	0,33
15	0,49

The heat storage by the amount of paraffin was determined by using literary data (c_{par} = 2100 $Jkg^{-1}K^{-1}$ and $L_{melt\ par}$ = 210000 Jkg^{-1}):

$$Q_{st\,lit} = m_{par} c_{par} \Delta T_{par} + m_{par} L_{melt\ par}\,, \tag{3}$$

where:
$Q_{st\,lit}$ – the heat storage by using literary data, J
m_{par} – the mass of paraffin, kg
c_{par} – the specific heat of the paraffin, $Jkg^{-1}K^{-1}$
$L_{melt\ par}$ – the melting heat of the paraffin, Jkg^{-1}

Table 3 shows the mass of paraffin and the heat storage by using literary data.

Table 3. Mass of paraffin and the heat storage by the amount of paraffin by using literary data

m_{par} (g)	Heat storage literature (kJ)
1	0,26
5	1,31
8	2,10
10	2,62
15	3,94

Differences in measurement and literature data may be caused by the presence of multiple paraffin depending on the composition and molecular chain, and may differ in their thermal data.

Conclusion

The previous measurements showed that solid paraffin wax is well suited for heat storage. In the calorimeter we measured the temperature changes of hot water and paraffin as a function of time, and we measured the water and paraffin masses. We determined from the measurement parameters the heat storage, the amount of water that can be substituted for the heat storage, we determined the heat storage per 1 g, finally, the heat storage by the amount of paraffin was determined using literary data. Compared to the previous measurement in Gödöllő (Bődi *et al.,* 2018) we managed to get closer to the literary values.

On the basis of the results it can be concluded that the heat storage between 40°C and 65°C per 1 g is on average 0,4 kJ, which can be replaced by 3,5 g of water, so 3,5 times less paraffin should be stored instead of one unit of water.

In order to achieve faster heat transfer, we would like to mix materials with paraffin that are good heat conductors (e.g. graphite, Al). Furthermore, we would like to investigate liquid paraffin for heat storage and cooling, comparing the results with the results of the solid paraffin test.

In additions to heat storage, the tests provide the basis for improving the efficiency of different solar systems.

References

[1] Bődi Sz., Víg P., Farkas I. (2018): Use of paraffin vax and water for heat storage in solar system, Book of Abstracts, 24rd Workshop on Energy and Environment, Gödöllő, Hungary, December 6-7, p. 17.

[2] Elbahjaoui R., Qarnia H.E., Naimi A. (2018): Thermal performance analysis of combined solar collector with triple concentric-tube latent heat storage systems, Energy &Buildings 168, pp. 438-456.

[3] Khan Z., Khan , Z.A. (2017): An experimental investigation of discharge/solidification cycle of paraffin in novel shell and tube with longitudinal fins based latent heat storage system, Energy Conversion and Management 154, pp. 157-167.

[4] Meng Z.N., Zhang P. (2017): Experimental and numerical investigation of a tube-in-tank latent thermal energy storage unit using composite PCM, Applied energy, 190, pp. 524-539.

[5] Preet S., Bhushan B., Mahajan T. (2017): Experimental investigation of water based photovoltaic/thermal (PV/T) system with and without phase change material (PCM); Solar Energy 155, pp. 1104-1120.

[6] Zeinelabdein R., Omer S., Gan G. (2018): Critical review of latent heat storage systems for free cooling in buildings; Renewable and Sustainable Energy Reviews 82, pp. 2843-2868.

Measurements of the grid quality for PV inverters

Atsu DIVINE KAFUI[1] – István SERES[2] – István FARKAS[2]
[1]Mechanical Engineering Doctoral School, Szent István University
[2]Department of Physics and Process Control,
Institute for Environmental Engineering Systems

Abstract

The continuous growth of energy demand and the diminishing fossil fuel reserves has put much pressure on the distribution electrical grids introducing issues of power availability, quality and security. The characteristic attributes of a fuel less and environment friendly electricity production from solar photovoltaics (PV), has made PV an indispensable source of power generation. Supplying AC loads and the grid with power from solar PV requires dc to AC inverters. In this study, a data logging system with an electric voltage divider was set up to measure and analyse the voltage-time functions of the grid and off-grid inverters. The development and the main components were outlined together with their properties and settings. Control measurements were carried out on the grid as well as on off-grid inverters and presented. Results show that the studied off-grid inverters produced modified square functions as against the sinusoidal shape for the electric grid.

Keywords

photovoltaic systems, inverters, electric grid, voltage function

1. Introduction

The demand for energy continues to rise with increasing population and economic growth. On the other hand, the stock of conventional energy sources continues to deplete gradually as their prices keep rising consistently. Currently, solar PV energy is experiencing an astronomical strong global growth. Policy support by various governmental and non-governmental institutions and technology cost reductions are enhancing the rapid growth of the variable renewable sources of energy generation, putting the power sector as one of the leaders in the emissions reduction efforts (IEA, 2018a).

Several configurations of solar PV systems exist, such as the grid-connected PV systems and standalone PV systems (off-grid). Currently, the installed capacity of grid-connected PV systems far outweighs the off-grid PV systems. According to IEA solar PV Trends 2018, the global PV installed capacity represented 403.3 GW of cumulative PV installations altogether, which is made up mostly of grid-connected systems, at the end of 2017 (IEA, 2018b).

An inverter is employed in the grid-connected PV systems to convert electricity from direct current (DC) as produced by the PV array to alternating current (AC) that is then supplied to the electricity network. The typical weighted conversion efficiency is in the range of 95% to 99%. (IEA, 2018b). Similarly, standalone PV systems also make use of DC – AC inverters to supply power to connected AC loads.

These inverters make use of the maximum power point tracking system (MPPT) to continuously adjust the load impedance to provide the maximum power from the PV array (IEA, 2018b). The MPPT employs a kind of control circuit or logic to search for the maximum point and thus allow the converter circuit to extract the maximum power available from the cells (Esram and Chapman, 2007). The DC voltage is then converted into an AC voltage using different techniques such as the full-wave inverter topology employing unipolar SPWM technique. Synchronization is then achieved between the grid and the PV system, after which power is fed into the grid by power flow control mechanisms (Hameed et al, 2016).

The power fed into the utility grid introduces several associated complications in both the transmission and distribution networks depending on the point of common coupling PCC (Esram and Chapman, 2007). According to Walker (2001), Multi-stage inverters are gaining greater attention in recent years, especially in grid tied PV systems as they come without voltage balancing problems. However, the multi-stage inverters have a lower switching frequency (mains frequency) than the standard PWM inverters consequently, having reduced switching losses. The line current waveform of the multi-stage inverters is also stepped shaped resulting in reduced harmonics compared to a square-wave inverter (Sarwar et al, 2012).

Interfacing with the ac grid, thus, involves two major tasks; one is to ensure that the PV array operates at the MPP. The other is to feed in a sinusoidal current into the grid with the lowest total harmonic distortion (THD) (Sarwar et al, 2012).

2. Objectives

The general objective of the study is to develop and validate a measurement method for checking the voltage -time function of inverters. The specific objectives are described as follows:

1. Develop a data logging system for measuring the voltage function of the electric grid where the data can be saved for later analysis.
2. Validate the measurement system by recording the grid voltage function.
3. Check the voltage function of off-grid inverters.

3. Materials and methods

The fast-changing electric signals can be analyzed by oscilloscopes, but the traditional ones cannot record but just visualize the measured functions. The

modern digital scopes can even record the data for further analysis. With the modern data logging system, the electronics are fast enough to be able to measure at the sampling rate of a several hundred thousand samples per second, which is generally fairly enough to check the shape of the inverter generated voltage functions.

3.1. Measuring circuit with NI USB 6009 unit

First, a basic data logger of the National Instrument, the model USB6009 was used for realizing a measurement system. This unit can be used with the maximum sampling rate of 48kS/s. Actually, it was used with the sampling rate of 40 000 samples /second, as in this way during one period of the 50 Hz electric grid 800 measurement data were recorded. From these 800 points the theoretic sinus function of the grid can be reproduced with good result.

The only problem is that, the USB6009 cannot be connected directly to the electric grid, as its measuring range is ±20 Volts, and the maximum overvoltage of the unit can be 35 Volt. The unit was used in the range of ±5 Volts, at this range with the 14-bit resolution, the typical measurement error is 7 mV.

To overcome the problem of the limited input voltage, a bridge connection was built, with a serial connection of two resistances (a voltage divider circuit). In this case two resistors of R_1= 1 MΩ = 1000 kΩ and R_2 = 10 kΩ were used. The basic equations of the serial connection of resistances:

$$U_1+U_2=U_0$$

$$\frac{U_1}{R_1} = I = \frac{U_2}{R_2} = \frac{U_0}{R_1 + R_2}$$

From these equations the U_2 voltage of the R_2 resistor can be evaluated as:

$$U_2 = \frac{R_2}{R_1 + R_2} U_0 = \frac{10}{1000 + 10} 230 V = 2.277 V$$

The test circuit with the control meter can be seen in Fig. 1.

As the motive of this measurement, was not for the effective (or the peak) voltage, but the shape of the function, we just wanted to be sure that, the measured maximum voltage is inside the measuring range of the data logger. As the effective voltage is about 2.27 V, then the maximum value is $2.277 \cdot \sqrt{2}$ ~ 3.2 V, which is fairly within the measurable range of the unit. (As we test a voltage function with sinus shape, the maximum value is $\sqrt{2}$ times bigger than the effective one).

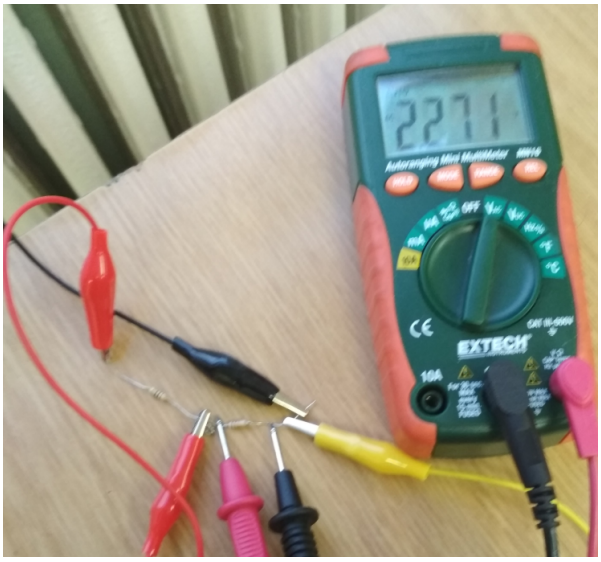

Figure 1. Checking of the voltage divider

3.1. Measuring circuit with NI MyDaq

If not just the 50 Hz sinus function of the grid voltage that has to be tested, but also higher frequency disturbances of the power lines as well, e.g. harmonics of the basic frequency, then the sampling frequency has to be at least one magnitude higher, than the measured frequency. For example, in case of investigation of sound frequency harmonics (maximum 20 kHz), at least 200 kS/s sampling frequency has to be used.

This sampling frequency cannot be carried out with the USB6009 unit, for this purpose an NI MyDaq was used, which can measure up to 400 kS/s sampling rate. As the voltage magnitude limit is similar for this case, the same bridge circuit has to be used for this solution, as well.

4. Results

This section presents the measurement results and the conclusion that can be drawn.

4.1. Results of the test measurement of the electric grid

First, the test measurements with the unit are presented. In Hungary, generally, the quality of the electric grid is quite good, so it was used to check the data logger. With the voltage divider circuit, the voltage-time function of the grid was measured with sample rate of 40 kHz, and altogether 1600 samples were measured (2 periods), the measured data were saved to a text file which was converted to excel for further analysis. The graph of the measured data can be seen in Fig.2.

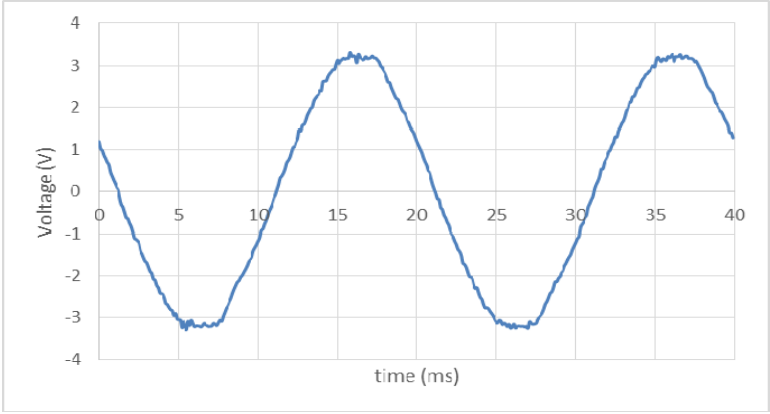

Figure 2. Voltage vs time function shape for the grid

From the graph it can be seen that, around the maximum values there are some fluctuations in the function, which can originatefrom the grid or, as our measuring unit is not shielded, it could come from some electromagnetic noise. To reduce the noise, 50 periods were measured after each other and they were averaged. In case of white noise (stochastic fluctuation), the average has to be zero (0), so the noise will disappear.

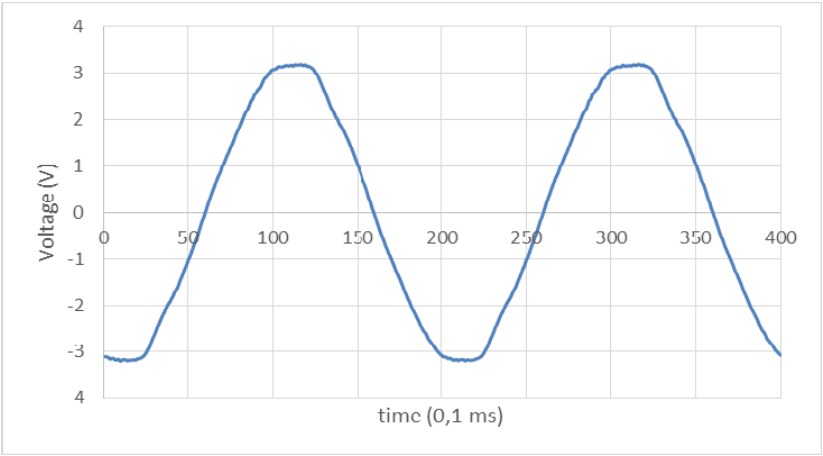

Figure 3. The average of 50 periods of measurement results

In Fig. 3, the averaged values are plotted, from where it can be recognized that, the fluctuations have disappeared in this way, so the origin of the fluctuation was a random error signal. As the start of the measurement was random, the initial phase angle of the sinus during the measurements were changing randomly, but this has no effect on the shape analysis of the function.

4.2. Results of the test measurement with off-grid inverters

After checking the measurement system, some off-grid inverters were tested. These inverters generally have low power (100- 300 W) and they are planned for use for standalone operation.

The list of the tested inverters is shown in Table 1.

Table 1. The tested off-grid inverters

Supplier	AC Power
Velleman PI 300M	300 W
Voltcraft PowerDisc 160	50 W

These simpler inverters generally provide square wave signals instead of the sinus signal of the grid, but for the energy supply of simpler unit this solution is enough. With the developed data logger system, the voltage function of the inverters could be also checked. The measurement results of the Voltcraft Powerdisc inverter can be seen in Fig. 4.

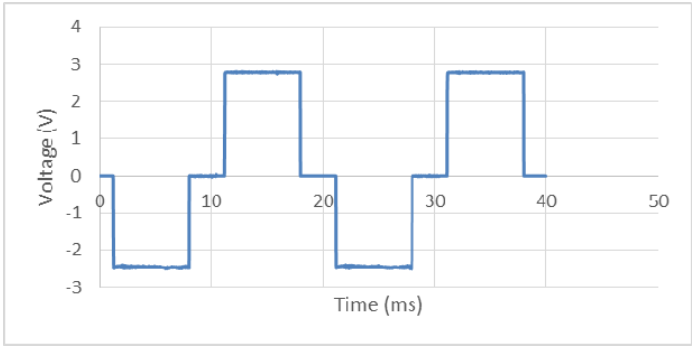

Figur 4. The square function of the off-grid inverter (Voltcraft Powerdisc)

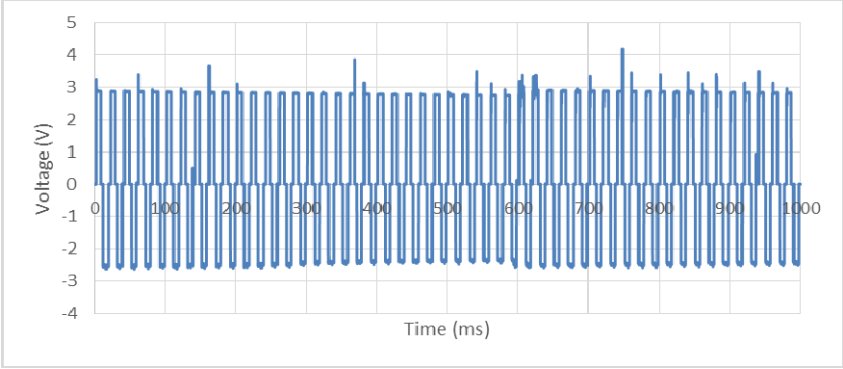

Figure 5. The instability of the voltage square function of the off-grid inverter (Voltcraft Powerdisc)

From Fig. 4. it can be seen that, instead of a sinusoidal function, a modified square function is generated by the inverter. If a longer time period of the output signal is measured, then we can recognize that, the generated signal is slightly changing, as it can be seen from Fig. 5.

From Fig. 5 it can be concluded that, this simpler off-grid inverter can operate simpler AC devices, but its voltage function is very unstable, and even its maximum value (and in this way its power) is slightly changing in time.

Summary

A data logging system with an electric voltage divider was set up to be able to measure the voltage–time function of the electric grid, and inverters. In this paper, the development and the main components of the data logger is presented, together with the important properties and settings.

Control measurements with the grid and with off-grid inverters were done and analysed in the paper. It can be seen, that the simpler off-grid inverters provide a modified square function against the sinusoidal shape for the electric grid. This fact can cause multifunctioning of sensitive electric devices.

In the future, numerical analysis of the functions (e.g. total harmonic distortion) will be made, and the measurements will be extended to grid connected inverters as well.

Acknowledgement

This work was supported by the Stipendium Hungaricum Programme and by the Mechanical Engineering Doctoral School, Szent István University, Gödöllő, Hungary

References

[1] International Energy Agency (IEA). World Energy Outlook, https://webstore.iea.org/download/summary/190?fileName=English-WEO-2018-ES.pdf 2018a, (Accessed: 05-02-19).

[2] International Energy Agency, IEA PVP Trends 2018 in photovoltaic applications. Survey report on selected IEA countries between 1992 and 2017. http://www.iea-pvps.org/fileadmin/dam/public/report/statistics/2018_iea-pvps_report_2018.pdf 2018b, (Accessed 05-02-19).

[3] Hameed, D., Hamayoon, S., Malik, A. A. and Ansari, O. A. (2016). Solar grid-tied inverter, with battery back-up, for efficient solar energy harvesting, *2016 IEEE Smart Energy Grid Engineering (SEGE),* Oshawa, ON, pp. 95-99. doi: 10.1109/SEGE.2016.7589507.

[4] Esram, T., Chapman, P.L. (2007). Comparison of Photovoltaic Array Maximum Power Point Tracking Techniques, IEEE Transaction on Energy Conversion, 22(2), 439-449.
[5] Walker, G. (2001). Evaluating MPPT converter topologies using a Matlab PV model, J. Electrical and Electronics Engineering, 21(1), 49-56.
[6] Sarwar, A., Arif, S. J., and Asghar M. S. (2012). A solar PV based multistage grid tie inverter. Innovative Systems Design and Engineering, Vol 3, No 6, pp. 77-90.

Efficiency of heat performance in embedded water-based heating systems with mortar discontinuity

Zoltán DODOG[1], Antal VERES[2]
[1]Department of Environmental and Building Engineering,
Institute for Environmental Engineering Systems
[2]Department of Mathematics,
Institute for Environmental Engineering Systems

Abstract

Embedded water-based surface systems are widely used and are reasonable choice for heat supply systems either for newly built buildings, and for house renovating processes as well. In these systems pipes are embedded in the building structure (floors, ceilings, walls) covered with mortar. During the installation process errors may occur. In this paper we investigate the efficiency of heat transfer of systems installed with mortar discontinuities behind the heating pipes creating air gaps. In our model we use basic building structure with errors to analyze the impact of discrepancies between rated performance as design value and faulty installations. Numerical simulations and calculations show that air gaps do not cause significant performance drop.

Keywords

surface heating, embedded heating, heat performance, temperature distribution

1. Introduction

Embedded wall heating systems are used in all types of buildings. These systems come in several different versions, but they can be roughly divided into water-based and electric systems. Wall heating can fundamentally be installed using either wet plastering or drywall installation, and the foundation my either be the wall itself or internal insulation [Friese *et al* 2013].

Water-based systems work with low water temperature for heating due to the large surfaces needed for heat transfer, which implies low energy cost to operate. Besides, the compatibility with modern condensing gas boilers or low temperature heat pumps makes these systems a popular choice, moreover radiant heating systems positively affect thermal comfort [Buckley 1989].

In the case of wet installation, prefabricated heating elements are directly attached to the structure and plastered over with mortar. During the installation process errors may occur. In this paper we investigate the efficiency of heat transfer of systems installed with mortar discontinuities behind the heating pipes creating air gaps.

2. Basic assumptions

The heat performance of surface heating depends on many factors and circumstances, but is mostly influenced by the followings [EN 1264-2]:

- distance between heating pipes (T),
- thickness (s_u) and thermal conductivity of covering layer,
- heat transfer resistance of the floor covering,
- diameter of heat pipe (D) and thermal conductivity of pipe material,
- parameters of heat distribution plate (if it exists),
- connection between the pipe and heat distribution.

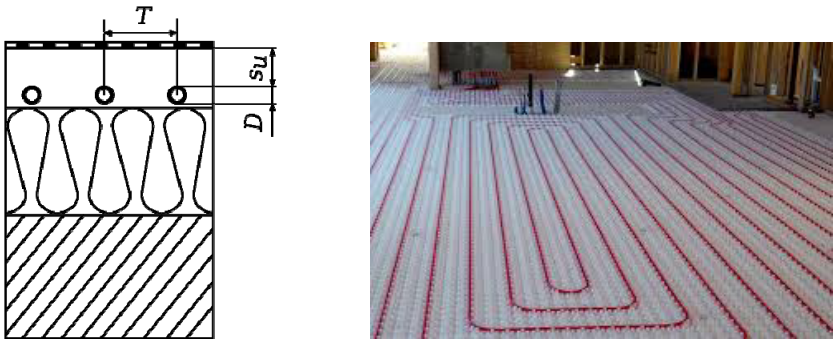

Figure 1. Cross section of a general water-based surface heating construction (left). Pipe laying on heat insulated floor (right)

More simplifications are needed for modeling building constructions with embedded water-based heating [Hu *et al* 2019]. In our case, the following key simplifications were applied:

- In most cases in building physics we suppose that heat transport processes are in steady state condition, because internal temperature is considered constant and the rate of change of outside temperature is slow and it has a daily cycle. Therefore, heat transport through building boundaries are quasi-stationary within short time intervals.
- Boundary conditions are considered as constants in time during the design process.
- The heat flow is always three-dimensional in structures, because the temperature in the tubes varies along the flow. Calculating the medium temperature of the flowing medium, it is enough to examine the heat flow in one cross-sectional plane.
- Analysis of a representative pattern instead of the whole heating structure is applicable.

Calculation of embedded heating system performance is complicated because of several factors. Let us consider a solid heat conductor with a non-linear constitutive equation for the heat flux. If the material is anisotropic and inhomogeneous, the heat conduction equation to be satisfied by the temperature field $T(x,t)$ is

$$\rho c_p \frac{\partial T}{\partial t} - \nabla \cdot (k \nabla T) = q_V \tag{1}$$

where c_p is the specific heat for given pressure, ρ denotes density, k stands for the thermal conductivity, q_v is the volumetric heat source and T is the temperature field at space coordinate x and time instant t [Ramirez *et al* 1973].

For the vast majority of geometries and problems, it is hard or even impossible to solve partial differential equations (PDEs) with analytic methods. Instead, an approximation of the equations can be constructed, typically based upon different types of discretization. These discretization methods approximate the PDEs with numerical model equations, which can be solved by using numerical methods, for example such a method is the finite element method (FEM). In special cases, methods derived from numerical results can also be used for calculations [Xing *et al* 2010].

3. The model

In our two-dimensional model we examine a wall with embedded water-based heating. Wall thickness is 300 mm with 100 mm expanded-polystyrene heat insulation on the outside. Heating tubes are embedded in mortar layer horizontally with 100 mm distance. Figure 2 shows a representative pattern of this structure.

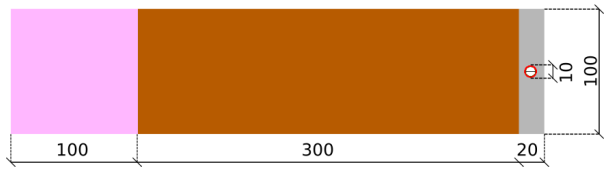

Figure 2. A representative pattern of the examined structure

The temperature of the flowing water changes along the heating pipe, since the heat transfer process between the structure and the water takes place. In practice, the value of the temperature drop is frequently determined as 5°C, but in our model, we use the average temperature of the supplying and the backward water. In the base model we assume that pipes are hermetically wrapped with mortar.

During the installation, mortar is sprayed to wall surface with high speed shown in Figure 3. Inadequate implementation or mortar plastering by hand can cause mortar discontinuity behind the pipe creating air gaps. In this case cavities may appear, where the pipe contacts with air, which is an influencing factor of the heat transfer, since polyethylene has a low emissivity factor and the space is inadequate for effective convection. The measure of the contact area can vary in a wide range. In our research we investigate the cases when the contact arc is 12.5, 25 or 37.5 percent of the circumference of the pipe. The considered cases are illustrated on Figure 4.

Figure 3. Plastering with mortar sprayer machine

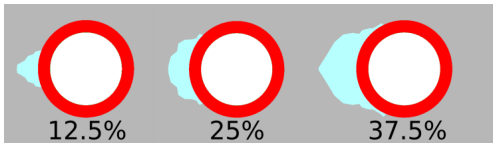

Figure 4. Different size air gaps behind heat tube

Under the assumption of steady state heat transfer process, the constants for material parameters, loads and constrains are presented in Table 1 and Table 2.

Table 1. Applied material parameters in model

Material name	Heat conductivity [W/mK]
EPS heat insulation	0.04
Solid brick wall	0.78
Polyethylene pipe	0.4
Mortar as covering layer	0.81
Air	0.024

Table 2. Applied loads and constrains in model

Load or constrain	Unit
Internal convection	20 °C - 8 W/m^{2}K
External convection	-4 °C - 24 W/m^{2}K
Pipe inside (flow) temperature	37.5 °C
Heat flux upside	0 W/m^2
Heat flux down	0 W/m^2

4. Analysis and results

Solving the heat equation by finite element method (we used LISA FEM software) provides the temperature and the heat flux value at every point of the

structure. Figure 5 shows the horizontal heat flux field of a heating element at design state when pipe is hermetically wrapped with mortar.

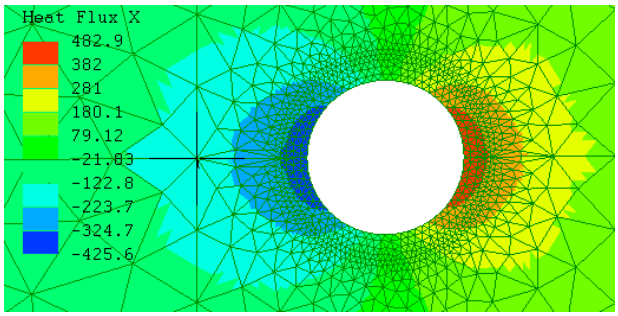

Figure 5. Horizontal projected heat flux values around the heating tube at design state

Comparing the results of the simulations of the four cases, we conclude that air gap behind the pipe causes only slight temperature drop on inside wall surface and with this causes slight performance loss (see Table 3). The heat loss in the last column is referred to the designed state.

Table 3. Surface temperature and heat flux on inner side

Examined model	Average surface temperature [°C]	Average heat flux [W/m^2]	Decrease [%]
Designed state	31.90	87.95	-
Air gap 12.5%	31.82	87.20	0.85
Air gap 25%	31.63	85.34	3
Air gap 37.5%	31.34	82.70	6

We think that the reason for this phenomenon is that air gap behind heating pipe acts as heat insulation, and as a consequence of this at the same time heat flow towards inner space is more intensive. Based on our simulations we conclude that in the case of similar structures faulty implementation does not cause significant loss in heat efficiency.

Conclusion

In the implementation of embedded surface heating systems made with water-based technology errors may occur, one of them is the lack of cover material

under the heating pipe. According to our research in the case of the examined building structure, the discontinuity of the cover material behind the pipes causes only a slight heating power loss.

References

[1] M. Friese, A. Worch (2013): Current state of the debate about wall heating systems, Report for Co2ol Bricks Project
[2] N.A. Buckley, (1989): Application of radiant heating saves energy, ASHRAE Journal 31., pp. 17–26.
[3] CEN. 1997. EN 1264-1997 Part 2, Floor heating – Systems and components. Determination of the thermal output.
[4] G. Aguirre-Ramirez, J. T. Oden (1973): Finite element technique applied to heat conduction in solids with temperature dependent thermal conductivity, International Journal for numerical methods in engineering, 7., pp. 345-355.
[5] W. Hu, P. Jia, J. Nie, Y. Gao, Q. Zhang (2019): A Fast Prediction Model for Heat Transfer of Hot-Wall Heat Exchanger Based on Analytical Solution, Applied Sciences, 9(1), 72
[6] Xing J, Xiaosong Z, Yajun L. (2010): A calculation method for the floor surface temperature in radiant floor system, Energy and Buildings 42, pp. 1753–1758.

Environmental and healthcare risks of refrigerants

Péter HERMANUCZ, István BARÓTFI, Gábor GÉCZI
Department of Environmental and Building Engineering,
Institute for Environmental Engineering Systems

Abstract

Cooling of raw materials and products in the industry as well as in transportation and storage is an important task. It has a great impact to the product quality, in this manner to the health, and of course to the environment. This paper deal with the application of refrigerant in the industry, the comfort cooling is out-of-focus. Our research covers the most important cooling systems and the widely applied refrigerants: their application range in temperature as well as system charge, their properties and risk factors to the environment and health will be shown. We paid special attention to the natural refrigerant and the new risk factors that they present. We investigate and analysed the international protocol, standards and national regulation of cooling area and refrigerant.

Keywords

natural refrigerant, health risk, environmental load, HFC, phase-out schedule

1. Introduction

The cooling demand can be found in different parts in the industry in different ways: One way is to cool down raw materials as fast as it could be, another way to reach very low temperatures, and of course to provide nearly constant temperature in case of transportation and distribution. Artificial cooling is widely used to solve these problems.

The inseparable part of a refrigeration cycle is the refrigerant itself, which also has a certain degree of global-environmental and local health risks. To measure the risks of a refrigerant or a cooling system some indicators and metrics were introduced. Environmental load is often characterized by the Global Warming Potential (GWP). GWP is an index, which compares the global warming impact of an emission of a greenhouse gas in relation to the impact from the emission of similar amount of CO_2. The impact is estimated during a 100 years' time horizon. [Makhnatcha and Khodabandeha, 2014]

Another important property of a refrigerant is the Ozone Depletion Potential (ODP). This is an index that characterizes the participation of the molecule to the depletion of the ozone layer. The value of this index is calculated by

compare to a reference molecule, namely either R11 or R12 that have ODP = 1. This means, that one molecule of R12 destroys 100,000 molecules of ozone during its life. [Molina and Rowland, 1974] The peak emission of ozone depletion was 1,5 Megatons in 1988. Thanks to the Montreal Protocol, the production of refrigerant with ODP is prohibited.

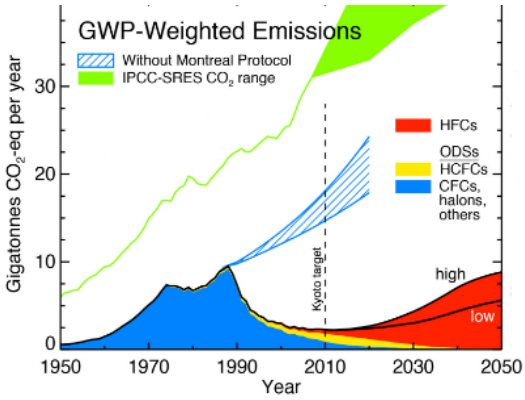

Figure 1. GWP-weighted emissions
[World Meteorological Organization, 2011]

Figure 1. presents the magnitude of the environmental hazards of the conventional refrigerants according to World Meteorological Organization and the GWP-weighted emissions of different refrigerant expressed in gigatons of CO_2 equivalent per year.

The emissions of individual gases such as CFCs, halons, HCFCs, HFCs are multiplied by their respective GWPs to obtain aggregate, equivalent CO_2 emissions. For reference are shown emissions for the range of CO_2-scenarios from the Intergovernmental Panel on Climate Change (IPCC). The dashed line marks 2010, the middle year of the first commitment period of the Kyoto Protocol. It could be easily established, that nearly half of the global warming impact were in conjunction with F-gases and many of these were refrigerants. This is the main reason why the environmental risk analysis is very important in industrial refrigeration, especially refrigeration in food industry and food chain. On the other hand, some of these refrigerants are toxic, and other ones are extremely flammable. Based on these it is essential to discuss the environmental load and health risks, to applicate laws and regulations too, which affect the construction of the refrigeration cycles used in the industry.

2. Materials and methods

By examining the refrigerants used in equipments operated nowadays, for example in food industry, the predominance of the R404a is conclusive in all

sectors (about 40% share) except for the Wine sector. R404a is a non-azeotrope blend. It consists about 52% of trifluoroethane (R143a) and 44% of pentafluorethane (R125) and 4% of tetrafluoroethane (R134a.) One of the reasons for this is that R404a is widely used in medium and low temperature refrigeration applications. [Cardoso *et al* 2017]

Another widely used refrigerant is the R717 in terms: Ammonium. For example, the two stage and double-lift type sorption cycle will mainly be operated with NH_3–H_2O for low-temperature application, but can be used for LiBr–H_2O also. [Ziegler, 2000]

There are a lot of household refrigerators which employee R134a (tetrafluoroethane) and R600a (isobutane) as refrigerant. R290 (Propane) and R744 (carbon-dioxide) are natural refrigerants and could be used in cascade systems. This is a quite new way of refrigeration, however at the beginning of artificial cooling only natural refrigerants were available. They have excellent energetic properties but are dangerous to the health. That is why they were supressed by the CFCs, which have no risk to the health, rather to the environment. Nowadays the natural refrigerants gained a lot in popularity, their market share is expanding. Over 54% (more than 1000 units) of all Aldi Süd's stores globally are running on CO_2, and over 15 000 units are in operation worldwide in 2017. [Alvaro, 2017]

[Cardoso *et al* 2017] found, there is a large amount of obsolete refrigerant used in the food industry. R22 (chlor-difluormethane) is the second most used refrigerant with about 30% share. It is in use in all the analysed sectors, is owed to its versatility and equipment age, essentially. Besides being found in older individual refrigeration systems, it is suitable for an enormous variety of refrigeration applications, across a wide range of temperatures. Controversially, R22 has an ODP of 0,05, so it destroys the ozone layer. Since 2010 it is prohibited to refill or service these cooling systems. They still in operation till some major failure occurs, then the refrigerant could be replaced to natural refrigerant. [Harby, 2017]

Table 1. The common refrigerants in the industry (based on references edited by authors)

Refrigerant	Applications	Temperature range	System refrigerant charge
R404a	Commercial and transport applications	Low/medium	1…500 kg
R134a	Household refrigerators and CO_2 cascade	Medium	0,1…100 kg
R744	Commercial systems	Low/medium	50…1000 kg
R717	Large industrial systems	Low/medium	50 … 5000 kg
R290	Commercial displays and CO_2 cascade	Low/medium	0,1…25 kg
R600a	Household refrigerators	Medium	0,1…25 kg

3. Discussion

Table 1. shows the refrigerants and their application as well as temperature range and typical system refrigerant charge.

In addition to the GWP, the lifetime of the refrigerant in our atmosphere is also important. Table 2. shows GWP, lifetime and Safety class for the common refrigerants used in the industry. The ODP of refrigerants shown in Table 2. are zero.

Table 2. Environmental metrics of refrigerants

Refrigerant	GWP	Atmospheric lifetime	Safety Class
R404a	3922	40	A1
R134a	1430	14	A1
R744	1	1	A1
R717	0	<1	B2L
R290	3	<1	A3
R600a	3	<1	A3

The impact to the health is classified by the safety class. The explanation of Safety Class can be found in Table 3. Two kind of risks are taken in account: Flammability is characterised by the concentration of Lower Explosive Level (LEL). At this concentration in air by volume, the air-refrigerant mixture can ignite and explode by a spark. The higher the concentration, the less dangerous is the mixture. Another property is the burning velocity. If the burning velocity of the mixture is lower than 10cm/s, the mixture could not explode. Some regulations (Eg. 517/2014 EU) allows only 20% of the LEL in closed spaces, so the chance of an explosion is nearly zero. The chance of exposure can be minimized, for example by restrict the charge in a cooling system. This limit for household refrigerators is 150g flammable HC. [517/2014/EU]

Table 3. Health impact of refrigerants

Flammability group	Toxicity group	
	A	B
	$LC_{50} \geq 10\,000$ ppm	$LC_{50} < 10\,000$ ppm
1 (Non-flammable)	A1	B1
2L (LEL ≥ 3,5% vol. and burning velocity < 10cm/s)	A2L	B2L
2 (LEL ≥ 3,5% vol.)	A2	B2
3 (LEL ≤ 3,5% vol.)	A3	B3

Toxicity, which has direct impact to the employees or customers, is measured by the LC_{50} value. This is the concentration of a material in air that will kill 50% of the test subjects (animals, typically mice or rats) when administered as a single exposure (1 or 4 hours). For R717, the critical concentration is 1000 ppm.

There's another kind of risk to the health. The product quality. While the product of the food industry is the food itself, in this case there is a direct relation between the quality of the product (influenced by the cooling process) and the health: Low quality processed food lowers the quality of life. Figure 2. summarize the risks of refrigeration to the health and environment.

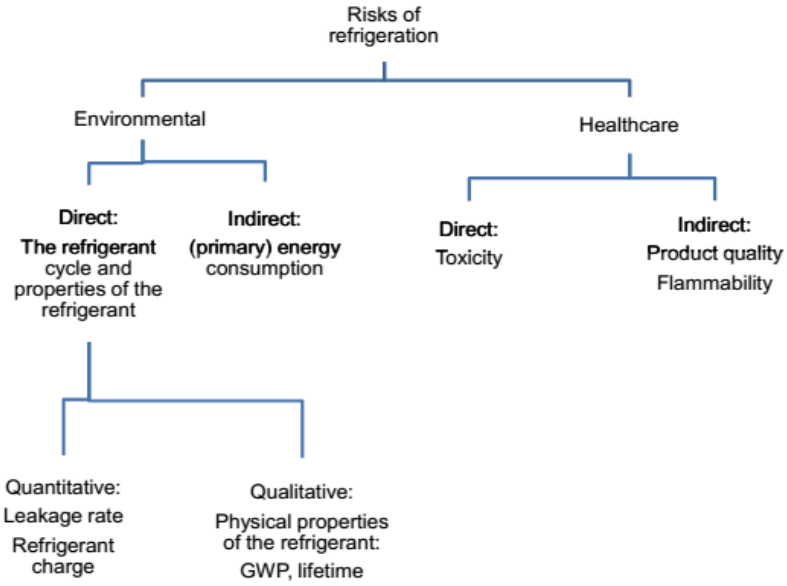

Figure 2. Environmental and healthcare risks of refrigerants

There is an indicator, which in addition to the direct impact of the refrigerant (estimated by GWP), takes in account the other impact to the environment: Any system or process, which requires energy input, indirectly affects the environment. This impact is originated from CO_2 emissions from the energy production processes. To indicate the overall environmental impact from a refrigeration system during it operation, this indicator, named Total Equivalent Warming Impact (TEWI) is used. TEWI accounts for the global warming impact from both direct and indirect emissions and calculated as a sum of both: direct effect of refrigerant released during the lifetime of the equipment and the indirect impact of CO_2 emissions from fossil fuels used to generate energy to operate the equipment throughout its lifetime [Pavel *et al* 2014]. It is essential to construct cooling systems with as low refrigerant charge as possible, because less refrigerant in a system automatically means lower TEWI [Kátai *et al* 2014].

As illustrated in Figure 3, bulk HFC quantities permitted to be placed on the market by producers/importers will be reduced year on year in accordance with the phase down schedule set out in 517/2014/EU.

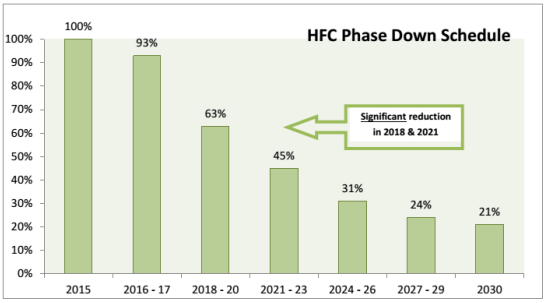

Figure 3. HFC Phase Down Schedule

In 2015 the quotas (in CO_2-eq.) for each producer or importer is 100% of the average volume of HFC placed on the market between the years 2009 - 2012. Until 2018 the phase down is modest. However, there are very significant reductions in 2018 (reduced by 33%) and again in 2021 (reduced by 22%). The phase down means that by 2030 the annual quantity of HFCs placed on the market and available to operators of equipment containing HFC will be reduced by 79% when compared to 2015. According to the, systems with 10.2 kg or more charge will be prohibited from being serviced and maintained from 2020. As R404A is widely used in the European refrigeration market, it could lead to significant cost increase and shortages in the coming years. [Cardoso *et al* 2017] In 2018, the bull market drove up the retail prices of HFC's to more than double than in 2017.

Conclusion

In our research I don't find any indicator that combine the health and environmental hazards of a refrigerant or a complete cooling system. In many cases an optimal solution to replace R22 which has ODP is the drop-in change to natural refrigerant R290.

I found that there's a hard push by the regulations to apply more and more natural refrigerants, because of their direct and indirect impact to the environment is very low. By contrast, these have lot of risks to the health, therefore there's a big challenge in changeover to natural refrigerants.

Hydrocarbon based natural refrigerants have a great advantage over conventional ones: the comparable system charge dropped by nearly 50% when replace HFCs by HCs. This significantly lower the risks to the health.

References

[1] Alvaro de Oña (2017): Global Market Trends for Natural Refrigerants in commercial refrigeration, Proceeding of Danish Technological Institute

[2] Cardoso B.J., Lamas F.B., Gaspar A.R., Ribeiro J.B. (2017): Refrigerants used in the Portuguese food industry: Current status, International journal of refrigeration, Vol. 83 p. 60–74
[3] EU Regulation No. 517/2014 Annex V.
[4] Harby K. (2017): Hydrocarbons and their mixtures as alternatives to environmental unfriendly halogenated refrigerants: An updated overview, Renewable and Sustainable Energy Reviews, Vol.73, p.1247-1264
[5] Kátai L., Várszegi T., Zsidai L., Csomai-Kürtössy R.N., Daróczi M., Nagy I. (2014): Functional Definition of the Basic Construction of Food Transport Containers Providing Universal Cooling, Storage and Handling Capabilities, Acta Polytechnica Hungarica, Vol. 11, No. 9, p. 23-37
[6] Molina M.J., Rowland F.S. (1974): Stratospheric sink for chlorofluoromethanes: chlorine atom-catalysed destruction of ozone, Nature 249, p. 810–812
[7] Makhnatcha P., Khodabandeha R. (2014): The role of environmental metrics (GWP, TEWI, LCCP) in the selection of low GWP refrigerant, Energy Procedia, Vol. 61 p. 2460–2463
[8] World Meteorological Organization (2011): Scientific Assessment of Ozone Depletion: 2010, Global Ozone Research and Monitoring Project–Report No. 52, p. 516.
[9] Ziegler, F. (2002): State of the art in sorption heat pumping and cooling technologies, International Journal of Refrigeration, Vol. 25, p. 450–459

Institute for Mechanical Engineering Technology

Professor Dr. Gábor KALÁCSKA
Director of the Institute

Dear Reader,

The year 2018 for our institute (Institute for Mechanical Engineering Technology including Department of Material and Engineering Technology, Department of Maintenance of Machinery, Department of Mechatronics) brought an intensive research period. Beside PhD programs the industrial partner based new faculty-level topics about additive technologies and the cold atmospheric plasma (DBD) treated polymer surfaces – sponsored by OTKA found – were the main fields. Traditionally the tribological evaluation of different engineering polymers e.g. in hostile abrasive condition played role as well. The following articles give a brief review about the activities and results, which may were already published or are going to be published in elsewhere more in depth.

- One article is related to the physical simulation of diffusion bonding/welding of Plasma Facing Components with the Gleeble 3800 thermomechanical simulator, which provides a non-conventional method. Instead of having a furnace with uniform radiation heating of the bulk material in a vacuum chamber, Gleeble applies Joule heating with 50 Hz alternating current passed through the specimens up to 10,000°C/second. Analytical and discretized model was built up taking into account the thermal conductivity, electrical resistivity in function of temperature.
- One article is dedicated to agricultural machine materials subjected to severe wear. The selected materials were ESD PA6 G, PA6G, and PLA reinforced with hemp (as bio-composite material). The examination was done in two steps: first by pin-on-plate test with sliding abrasive clothes, then a 3D microscopic photos of the worn surfaces to see how the friction affected these specimens. In the pin-on-plate abrasive wear system, we found that PA6G was the best choice of the used polymers because it had the lowest wear rate, while for the 3D microscopic PA6G ESD was the most outstanding worn surface.
- Additive technology: concerning polymers, fused deposition modelling (FDM) and digital light projection (DLP) technologies have been used for three-dimensional (3D) printing of tensile and tribology test specimens. Several print parameters were examined during the process of utilised methods. The performance of the two employed 3D printers in

the present work was evaluated according to the production speed, materials used, properties of the printed pieces, and geometrical and economical aspects. With metallic and ceramic materials: steel, aluminium and copper alloy powders are blended with aluminium oxide ceramic powder and used as a raw material for 3D printing. The prepared specimens are analysed by metallographic examination.

Plastic deformation and heat generation rate at the contact surface during diffusion bonding at Gleeble 3800 thermomechanical simulator

Tétény BAROSS[1], László JÁNOSI[2], Gábor VERES[1]
[1]MTA Wigner FK RMI
[2]Department of Mechatronics,
Institute for Mechanical Engineering Technology

Abstract

For diffusion bonding physical simulation of Plasma Facing Components the Gleeble 3800 thermomechanical simulator provides a non-conventional method. Instead of having a furnace with uniform radiation heating of the bulk material in a vacuum chamber, Gleeble applies Joule heating with 50 Hz alternating current passed through the specimens up to 10,000°C/second. Specimens are gripped by jaws that lead to a temperature distribution along the specimens. Therefore analytical and discretized model was built up taking into account the thermal conductivity, electrical resistivity in function of temperature. The contact area was modelled according to the plastic deformation of contact asperities as proposed by Hill and Wallach (1989) diffusion bonding model's first step. The results indicate that one can avoid melting on surfaces during Gleeble heating up process at a 20-70 MPa bonding pressure. However during the long 1-2 hours bonding process the applied pressure needs to be decreased, because of undesirable large creep mechanism following the low yield stress at elevated bonding temperature. This paper summarizes the temperature distributions along the specimens, as the temperature at mating surface in steady-state.

Keywords

Diffusion bonding, thermal distribution, Gleeble physical simulator, contact surface

1. Introduction

Diffusion bonding methods as a candidate solution for Plasma Facing Components in fusion reactors involved significant investigations over the last decades. The author is planning to carry out the diffusion bonding simulations in Gleeble labor in University of Dunújváros, Hungary (uniduna.hu). For preparation of these experiments the presented work focus on thermal calculations of a Gleeble 3800 thermomechanical physical simulator and

theoretical calculations of diffusion bonding. The article is a part of series to introduce the results in the frame of the author's phd work and continuation of previous article (T. Baross, 2017).

Gleeble 3800 thermomechanical physical simulator is able to combine heating and various type of mechanical loading at standard sized specimens: Ø6 – 12 mm, length: 140 mm. It applies direct resistance heating by 50 Hz alternating current up to 10,000°C/second and applies maximum static pressure 20 t under mid 10-5 Torr range (gleeble.com). The system provides a high range of welding simulation like HAZ (heat affected zone) simulation (See Fig. 1.), material tests like creep tests at elevated temperature, which capacities are well within the diffusion bonding parameters.

In literature few references are available about diffusion bonding at Gleeble instruments (K.P. Singh et al., 2016, E. Mizia et al., 2018) and some dedicated computer systems developed for Gleeble as well, as a FEM 3D modelling of thermal distribution (J.A. Spittle et al., 1997) and a simulation of changing material properties at casting temperature (M. Hojny et al, 2011). For the investigation of diffusion bonding at Gleeble a new and simplified 1D thermal modelling was modelled and the plastic deformation of theoretical diffusion modeling by Hill and Wallach (1989) was applied. Fig. 1. Presents the schematic view for thermal calculations of test cell.

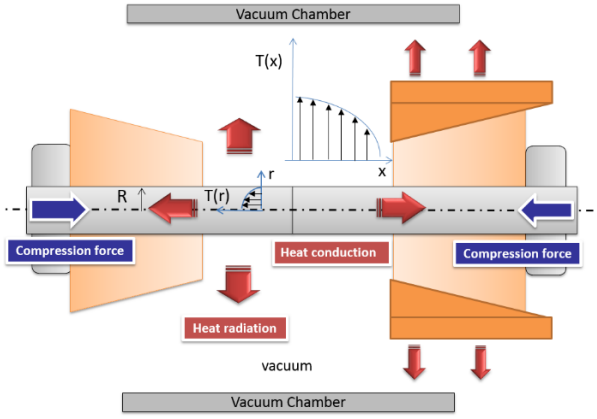

Figure 1. Schematic view of specimens with copper jaws

The Hill and Wallach diffusion bonding model (1989) gives the expected bonded area after a given time by combination of 7 mechanisms. This study calculates the first mechanism: the plastic yielding deforming of original contacting asperities. The materials that shall be relevant for fusion reactor materials were estimated in this study. In this way as an example an ODS steels (oxide dispersion strengthened steels) produced with similar matrix material. The latter was modelled and tested earlier by W. Sittel in her Phd thesis (2014).

2. Plastic deformation mechanism of diffusion model

This study calculates the plastic yielding deforming the original contacting asperities. The contact area of the asperities rapidly grows until the applied load can be supported and the local stress falls below the material's yield stress. (A. Hill, et al., 1989) Since the model assumes fully symmetrical geometry – as *Figure 1*. shows – one quarter of an elliptical section is considered. In Figure 2. b denotes the width of one quarter, a is the bonded length and $c = b - a$ the horizontal axis of the ellipse.

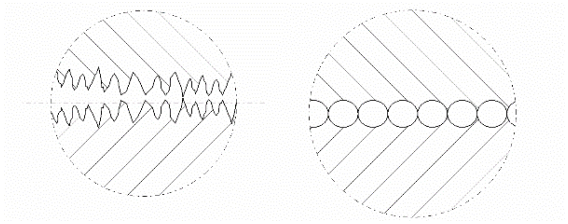

Figure 1. Modelled surface as parallel ridges, identical voids formed through the cross-section

For plastic mechanism the following assumptions are necessary (A. Hill, et al., 1989):

- Same surface roughness at both side for simplifying the modeling;
- The peaks join perfectly to each other, and the surfaces has no waviness;
- no work hardening approximately, because of the high temperature of bonding and the microscopically plastic deformation that do not effect on grain boundaries.
- Instantaneous deformation not allowing the time dependent mechanisms.

The fractional bonded area are represented in Fig.4.

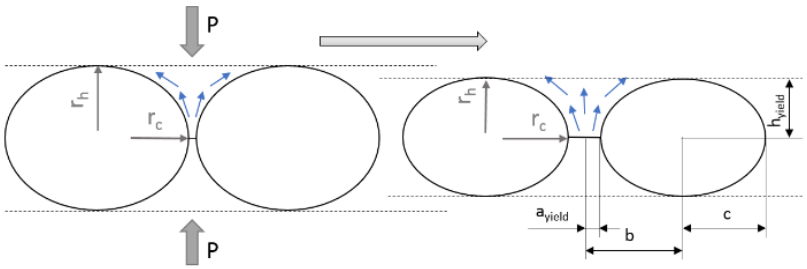

Figure 2. Plastic deformation mechanism of elliptical voids

Estimation of a_{yield}, where the deformation stops was derived from Eq. (1) after solving it numerically.

$$a_{i(yield)} = \frac{\sqrt{3}\cdot(p\cdot b-\gamma_s)}{2\cdot R_{p0,2}\cdot\left[1+\frac{r_c}{a_{i-1}}\right]\cdot\ln\left(1+\frac{a_{i-1}}{r_c}\right)} \quad (1)$$

The driving force is the applied pressure denoted by P. $R_{P0,2}$ is the 0,2 % proof stress, γ_s is the surface energy for ferritic or austenitic phase given by (A. Hill, et al., 1989), r_c is the required neck radius of the void.

The void height h_{yield} using the volume conservation argument can be derived by eq. (2):

$$h_{i(yield)} = h_{i-1}\frac{b-\frac{\pi}{4}(b-a_{i-1})}{b-\frac{\pi}{4}(b-a_i)} \quad (2)$$

In Table 1. the 0,2 % proof stress of fusion relevant or similar materials are given. The initial surface roughness parameters were chosen for all the three samples: b = 5 µm, h = 1 µm and as initial value a = 0,001*b. The surface energy was chosen to γ_s=1,95 J/m^2.

Table 1. 0,2 % proof stress for fusion relevant materials at different temperatures

Material	Temp. [°C]	$R_{p0,2}$ [MPa]	Ref.
PM 2000 (ODS)	20	857	[12]
PM 2000 (ODS)	800	113	[12]
SS 316L (N)-IG	20	220	[14]
SS 316L (N)-IG	700	102	[14]
EUROFER 97	20	560	[15]
EUROFER 97	700	170	[15]

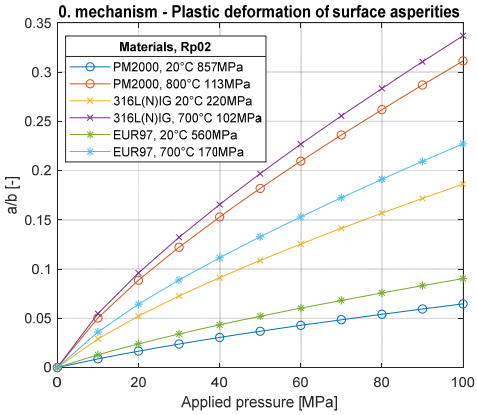

Figure 4. Bonded area after plastic deformation at different applied pressure

The results indicated that to reach a minimum 5 % contact area one needs to apply 20 – 70 MPa bonding pressure at room temperature. To avoid the undesirable creep mechanism at elevated temperature 900-1100 °C, where yield strength of steels is significantly lower 40-60 MPa, the applied bonding pressure shall be decreased.

3. Thermal calculations in Gleeble specimens

3.1 Analytical and discretized modeling of thermal distribution

In author's previous work (T. Baross et al, 2017) the thermal distribution model of specimens was determined with analytical and discretized modelling. Fig.1. shows two specimens fixed by copper jaws on both sides ensuring the good thermal conductivity at the gripping points and the electrical conductions for current. According to the Gleeble Users Training book (2010) in this case the temperature at boundaries can be chosen approximately as a constant value. Furthermore, assuming the heat radiation negligible and using thermal sleeve around the specimen gives a 1D thermal distribution in axial direction. For first thermal calculations we did not assume electrical or contact thermal resistance between the two specimen joining surfaces.

The analytical temperature in 1D distribution for volumetric heat generation rate is described by eq. (3).

$$t(x) = -\frac{\dot{q}_v}{2\lambda} \cdot x^2 + \frac{\dot{q}_v}{2\lambda}\left(\frac{\delta}{2}\right)^2 + t_\infty \tag{3}$$

For a more realistic estimation the thermal conductivity and electrical resistivity in function of temperature cannot be neglected, so Figure 3. gives an example for discretized elements.

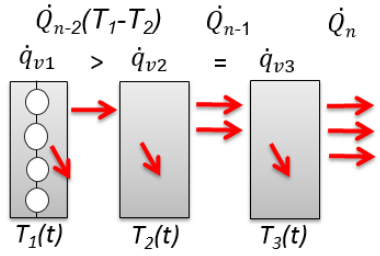

Figure 3. Discretized elements of thermal distribution

The heat conduction of the nth element $\dot{Q}_n$ will conduct the heat generated in the sum of elements between the middle – joining surface and the adjacent element. So heat conduction is derived as Eq. 4.

$$\dot{Q}_n = \lambda(T_{n-1}) \cdot \frac{F_n}{l}(T_{n-1} - T_n) = \sum_0^{k=n} R_k(T_k) \cdot I^2 \tag{4}$$

In Eq. (4) $\lambda(T_n)$ and R_k is derived in function of temperature. It is the resistance of one discretized element, where ρ is the specific electrical resistivity Ωmm^2/m in function of temperature.

$$R_k(T) = \rho(T) \cdot \frac{l}{A} \quad [\Omega] \tag{5}$$

Table 1. Parameters for material 1.4404 in f(T)

Name	Equation	Ref.
Sp. Electr. Res. T [K]	44+0,1*T-0,000031*T2	Appr. [17]
Thermal conductivity	0,01502*T + 13.98	[14]
Current density	605 A	

Table 1. summarizes the equations for parameters depending on temperature. Specific electrical resistivity was taken from C.J. Smithells, (1992). The analytical and discretized model results are shown in Figure 4. Results reveal that discretized calculations predict a much higher temperature than thermal conductivity in middle temperature. For a more precise modelling and validation of a Gleeble 3D FEM model the temperature dependency of parameters are not avoidable.

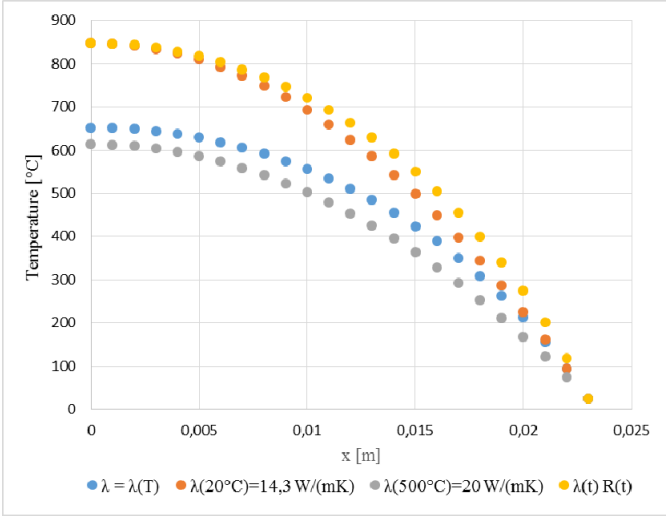

Figure 4. Temperature distribution in specimens for thermal conductivity and electrical resistivity as a function of temperature

3.2 Heat distribution near to the mating surfaces

Since the Gleeble heating is done by Joule-heating, and the mating surfaces have several peaks and valleys the normal surfaces are held apart by their roughness (A. Hill et al., 1989). It raised a possible issue during heating, namely that around 1% of contacting surface will melt since the same current pass through its peaks as a in the bulk material that ensures the heating up to 1000 °C. See Figure 3 as visualization. Therefore, we need to derive the maximum current compared to the percentage of the contacted area. Although heating up process is a transient process, by assuming a long heat up process and using constant current we can approximate it with steady-state calculations as well. The 5 mm is the full cross-section and 0,01/0,25 mm are the contact area.

The Figure 5. Shows the sum up of the void cross-section similar to the estimated in previous section. Since the heat removal from mating surfaces is calculated as a 1D geometry, we can replace the real cross-section with an equivalent 1D geometry.

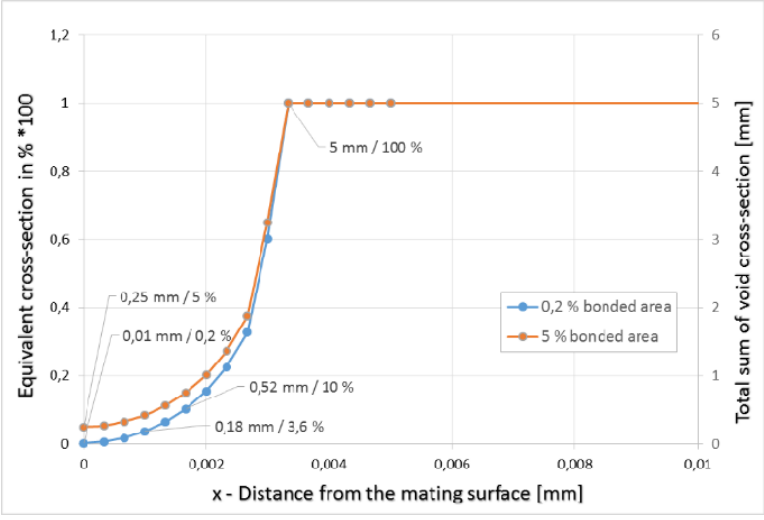

Figure 5. Equivalent micro geometry of specimen near to the joining surface for 1D discrete modelling

With this geometry one can determine the heat generation at a given current rate for different area of discretized cross-sections. For the very top of peaks the heat generation rate can be several orders of magnitude higher than at the same current in bulk material, respectively. Parameters were chosen as shown in *Table 1*. For simplicity the electrical resistance was taken into account as a constant value 0,75 (Ωmm²/m) from C.J. Smithells, (1992).

Figure 6 shows heat generation rate at the contact asperities, where the heat generation close to the contact surface is several order of magnitude larger than the heat generation in bulk material.

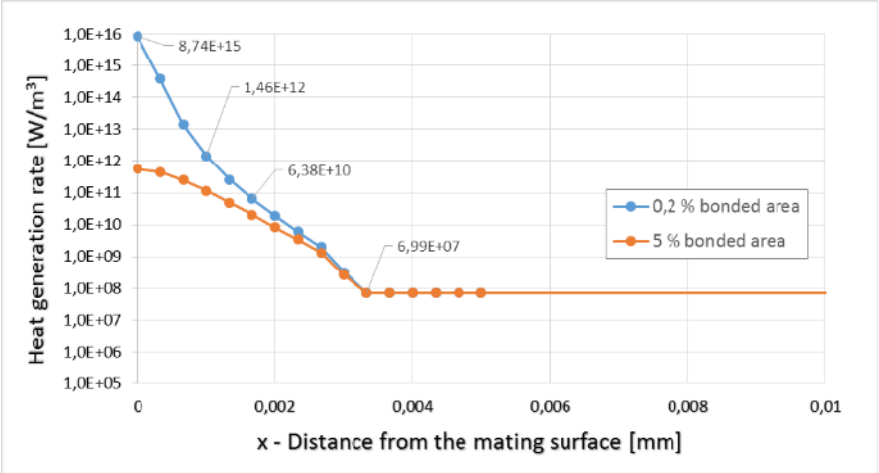

Figure 6. Heat generation rate in specimen near to the joining surface in logarithmic scale

The temperature distribution in steady-state is shown in Figure 7. Although the peak temperature is not relevant in worst case, during ramp-up at transient case the Gleeble 3800 may apply higher current 800-1000 A or even higher to reach the demanded bulk temperature of 900-1100 °C, that can melt the contact asperities. Figure 7 indicates also that the specimen peak temperature will decrease with higher bonded area, because of the less heat generated during welding process.

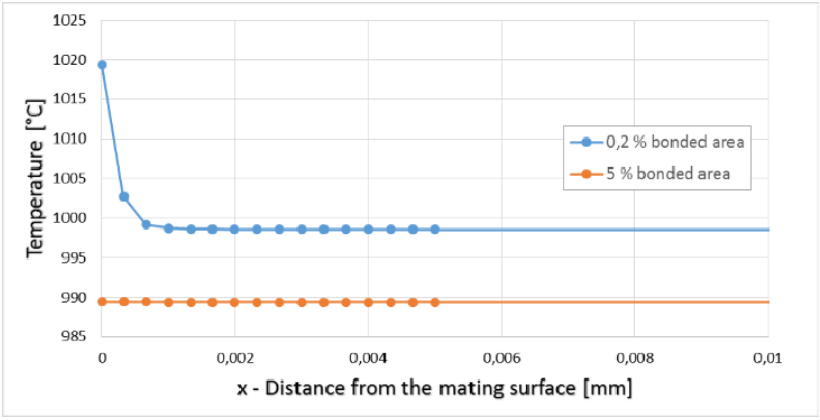

Figure 7. Temperature distribution in steady-state condition near to joining surface

Following these estimations it is suggested that compression force has to be applied first at room temperature to ensure a minimum 5-10 % bonded area (contact asperities) before the Joule-heating would have been applied.

Conclusions

This article aims to give the temperature distribution and thermal behavior of mating surface in specimens heated in a Gleeble 3800 Termomechanical Simulator. These calculations aim to define the proper welding parameters, which may endure 1-2 hours.

The results indicate that to avoid melting on surfaces during Gleeble heating up process a certain axial pressure is required. However during the long 1-2 hours bonding process the applied pressure need to be decreased, because of undesirable large creep mechanism following the low yield stress at elevated bonding temperature.

The 2D plastic deformation proposed by Johnson and used in Hill and Wallach diffusion model (1989) is validated by experiments, but significant improvement could be the extension of the model to waved surfaces as well.

Acknowledgments

This calculation was prepared in the frame of SZIE PhD school, in this way many thanks for the leaders of IPMP (International PhD Mentor Programm) Dr. Gábor Kalácska. Special thanks to Dr. Péter Bereczki, who demonstrated me the Gleeble 3800 Thermomechanical Simulator at University of Dunaújváros.

The work is supported by the ÚNKP-18-3 IV New National Excellence Program of The Ministry of Human Capacities.

References

[1] http://www.uniduna.hu/images/dokumentumok/Gleeble_labor.pdf

[2] T. Baross, L. Janosi and G. Veres, (2017): Analytical and numerical model of the temperature distribution of diffusion welding specimens on a Gleeble 3800 thermomechanical simulator, Mechanical Engineering Letters, Szent István University, Volume 15, page 16-26, HU ISSN 2060-3789S.

[3] https://www.gleeble.com/products/gleeble-systems/gleeble-3800.html

[4] K.P. Singh, Alpesh Patel, Kedar Bhope, S.S. Khirwadkar, Mayur Mehta, (2016): Optimization of the diffusion bonding parameters for SS316L/CuCrZr with and without Nickel interlayer, Fusion Engineering and Design, Volume 112, Pages 274-282, ISSN 0920-3796, https://doi.org/10.1016/j.fusengdes.2016.09.004.

[5] E. Mizia, R & E. Clark, D & Glazoff, Michael & E. Lister, T & L. Trowbridge, T. (2018): Progress Report for Diffusion Welding of the NGNP Process Application Heat Exchangers. 10.2172/1036269.

[6] J.A. Spittle et al., (1997): Numerical Simulation of Temperature Distributions in Gleeble Specimens as a Function of Time, Proc. 7th Int. Symposium on Physical Simulation of Casting, Hot Rolling and Welding, At Tsukuba, Japan, (Tsokuba National Research Institute for Metals) p 181

[7] M. Hojny, M. Glowacki, R. Kuziak, W. Zalecki,(2011): Development of Dedicated Computer System for Gleeble 3800 Thermo-Mechanical Simulator, Lecture Notes in Engineering and Computer Science, Newswood and International Association of Engineers, http://www.iaeng.org/publication/IMECS2011/IMECS2011_pp1507-1512.pdf
[8] A. Hill, E.R. Wallach, (1989): Modelling solid-state diffusion bonding, Acta Metallurgica, Volume 37, Issue 9, Pages 2425-2437, ISSN 0001-6160
[9] Derby, B. & Wallach, E.R. J Mater Sci (1984) 19: 3140.
[10] Derby, B. & Wallach, E.R. J Mater Sci (1984) 19: 3149.
[11] W. Sittel, (2014): (Phd work) Entwicklung und Optimierung des Diffusionsschweissens von ODS Legierungen,
[12] W.W. Basuki, (2008): (Phd), Optimierung der Diffusionsschweißparameter von Hastelloy® C-22® zur Herstellung von Mikrowärmetauschern,, ISSN 0947-8620
[13] Wiebke Sittel, Widodo W. Basuki, Jarir Aktaa, (2013): Diffusion bonding of the oxide dispersion strengthened steel PM2000, Journal of Nuclear Materials, Volume 443, Issues 1–3, 2013, Pages 78-83, ISSN 0022-3115,
[14] V. Barabash et al.,(2013): Summary of Material Data For Structural Analysis of the ITER Vacuum Vessel and Ports
[15] H. Tanigawa, K. Shiba, A. Möslang, R.E. Stoller, R. Lindau, M.A. Sokolov, G.R. Odette, R.J. Kurtz, S. Jitsukawa, (2011): Status and key issues of reduced activation ferritic/martensitic steels as the structural material for a DEMO blanket, Journal of Nuclear Materials, Volume 417, Issues 1–3, 2011, Pages 9-15
[16] Gleeble Users Training (2010): Gleeble Systems and Trainings
[17] C.J. Smithells, (1992): General Physical Properties, Metals Reference Book, 7th ed., E.A. Brandes and G.B. Brook, Ed., Butterworth-Heinemann, p 14–1

3D topographical analysis of abrasive worn surfaces

Adam KALACSKA[1], Hasan MUHANDES[2]
[1]Ghent University, Soete Laboratory, Department of Electrical Energy,
Metals, Mechanical Construction and Systems
[2] Deprtment of Maintenance of Machinery,
Institute for Mechanical Engineering Technology,

Abstract

This study is to know the wear behaviour of several composite materials as suggested replacements of some critical fast-wearing steel in Agricultural machinery. The selected materials are ESD PA6 G, PA6G, and PLA fortified with hemp (as bio-composite material), the examination was done into two steps, first by pin-on-plate test with sliding abrasive clothes, then a 3D microscopic photos of the worn surfaces to see how the friction affected these specimens. In the pin-on-plate abrasive wear system, we found that PA6G was the best choice of the used polymers because it had the lowest wear rate, while for the 3D microscopic PA6G ESD was the most outstanding worn surface.

Keywords

Wear of plastics, abrasion test, 3D microscopic photos, pin-on-plate, composite materials

1. Introduction

[Mishra, 2014] Nowadays, abrasive wear of engineering and agricultural machine components caused by the abrasive particles e.g. soil [Blahunka, Bártfai 2013] is a major industrial problem. Therefore, a full understanding of the effects of all system variables on the abrasive wear rates is necessary to undertake appropriate steps in the design of the machinery and the choice of materials to reduce/control wear.

Due to substantial losses because of friction and wear of agricultural machine parts, so polymer matrix composites are a perfect application due to their high durability, fracture toughness, and abrasion resistance properties.

[Sawpan *et al* 2011] Thermoplastic bio-composites experience a continuing demand for various industrial applications. This is due to several specific advantageous characteristics that can be combined in these materials. [Kim, Park, 2017] Thermoplastics, reduced processing times, highly increased storage times, and favourable recycling capabilities, by using thermoplastics we can separate the components after using them. And the process will be easier, cleaner and faster. [La Mantia, Morreale, 2011] Environmentally friendly, degradable biomaterials, used to create true bio-composites, possess the ability to improve the environmental impact

of commonly used composite materials significantly. This includes both natural fibres, used for the reinforcement component of a composite, as well as matrix materials from renewable resources. [Biron, 2013] The using of thermoplastic matrices is better than using thermosets because thermoplastics has facilitated recycling by being able to be molten and reshaped for numerous times. [Khondker et al 2006] demonstrate that thermoplastic materials like PP (polypropylene), PE (polyethylene) and PVC (polyvinyl chloride) dominate as matrices for natural fibres. [Ellis et al 1995] By using a scanning electrochemical microscopy (SECM) high-resolution three-dimensional images were generated by measuring the variation in the tip current due to perturbations in the diffusion layer.[Nasrullah et al 2005] A study of Surface Roughness of Thin Silicon Films Deposited on SiO2 was done by using an Atomic Force Microscope. Several Silicon Films were used like amorphous silicon and Low-pressure, chemically-vapour-deposited silicon films on silicon dioxide. [Tholt et al 2006] Also the Atomic Force Microscope and Profilometer were used to calculate the Surface Roughness in Ceramics specimens where the surfaced had different Finishing Techniques. Three ceramic materials were used: Vitadur Alpha, IPS Empress 2 and AllCeram. Five surfaces finished systems were used. The stylus profilometer and an atomic force microscope (AFM) are the two used roughness measuring instruments.

2. Materials and Methods

At that point, as per the above brief survey for some written literature, two types of composite materials which are (PA6G and PA66GF30) and PLA fortified with hemp as a kind of bio-composite materials were recommended to supplant these steel parts.

Table 1. The main properties of the PA6G and PA66GF30

Properties	Method	PA6G	PA66GF30
Density [g/cm3]	DIN EN ISO 1183	1.15	1.34
Yield stress [MPa]	DIN EN ISO 527-2	80	91
Modulus of elasticity (tensile test) [MPa]	DIN EN ISO 527-2	3500	5500
Elongation at break [%]	DIN EN ISO 527-2	130	13
Flexural strength [MPa]	DIN EN ISO 178	109	135
Impact strength, Charpy [kJ/m2]	DIN EN ISO 179-1eU	Nem törik	87
Tensile strength [MPa]	DIN EN ISO 527-2	83	91
Compressive strength [MPa]	EN ISO 604 1% / 2%	19 / 36	25 / 46
Notched impact strength, charpy [kJ/m2]	DIN EN ISO 179-1eA	4	
Ball indentation hardness [MPa]	ISO 2039-1	170	216
Shore D hardness [-]	DIN EN ISO 868	83	86

Table 2. The main properties of the PLA-Hemp [Bio-composite]

Properties	PLA-Hemp [Bio-composite]
Density [g/cm^3]	1.28
Fibre volume fraction Vf [%]	34.62
Matrix volume fraction Vm [%]	61.99
Porosity volume fraction Vp [%]	3.39
Tensile strength [MPa]	58.36
Young's modulus [GPa]	26.05
Elongation at break [%]	0.59
Flexural strength [MPa]	126.69
Flexural modulus [GPa]	7.72
Impact strength [KJ/m2]	24

To test these materials, a pin-on-plate test with a sliding abrasive cloth. Pin-on-plate test made by using the following device:

Figure 1. Pin-on-plate wear device.

This device can give us a nonstop wear interface and furthermore a possibility to control several parameters:

1. Opportunity to control the speed of the interface wear.
2. Possibility to use several wear interfaces
3. Opportunity to add a load over the specimens.
   - Two types of wear interfaces were used (P60 and P150).
   - Two speeds are used which are (20%=0.032 m/s and 40%=0.056 m/s)
   - And we used Three loads (9.81 N, 29.43 N and 49.05 N)

Wear of different structural plastic materials was analysed by measuring relevant features during abrasion tests (time, force, abrasion rate). Experimental equipment has been utilised to trace the wear of plastic materials under the same conditions. Abrasion rate has been recorded, together with pressure (force)

applied on the sample. Length (duration) of the experiments have been standardised by taking identical experimental runtime. Simple apparatus assembled (Figure 2) and sensors were connected to a computer data collecting interface. The interface was converting the sensor signals into digital values and provided the data to a computer that was recording the values.

Figure 2. The Specimen holder and the connected sensor

Several strain gages are connected to a PC by an estimation device (Spider 8) to take these parameters as results.

The interface was converting the sensor signals into digital values and provided the data to a computer that was recording the values.

Figure 3. Spider 8, a strain gage measurement device

The used specimens have an exact dimension with 8mm diameter and 20 mm length.

We tested each sample for 10 minutes; some samples didn't bear this time due to its specifications, enormous load, and substantial sliding speed. These cases we can see it amid the results.

After testing these samples, we took them to do the 3D microscopic check to calculate some parameters and to get a 3D profile of the worn surfaces.

To do this process we used (Taylor Hobson CCI HD) device. The Measurement type is Non-contact 3D optical profilometry.

Figure 4. Taylor Hobson CCI HD device

This device has several features like:

- Reduced inaccuracy and noise compared to 2D
- High resolution, precise results
- Data extraction from whole 3D surface

And during the measurement the used settings are:

- 50X lens
- Scanning speed: x1, 4m mode, filter 2, rough surface

3. Results

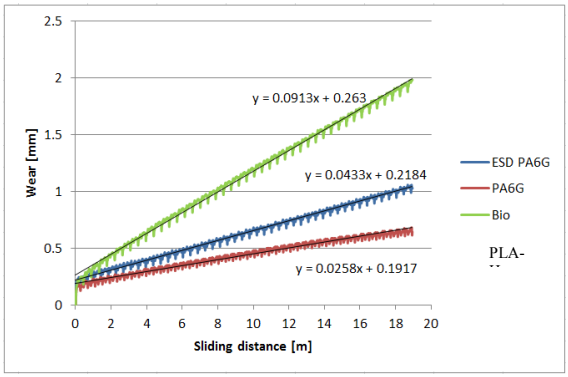

Figure 5. The relation between the wear and sliding distance for several polymers types

Figure 5 demonstrates a comparison between the wear and sliding distance for several polymers types; the load is 9.81N, the sliding speed is 0.0315m/s, and the wear interface is P60. We can compare the different types of polymers by using the slope value of the wear lines.

Table 3. Wear line equation and the slope value of the different polymers types

Type	Wear line equation	Slope value
PLA-Hemp	y=0.0913x+0.263	0.0913
ESD PA6G	y=0.0433x+0.2184	0.0433
PA6G	y=0.0258x+0.1917	0.0258

From figure 5 and table 3, we can see that PLA-Hemp was subjected to the highest wear rate and had the maximum slope value, while PA6G had the lowest wear rate and had the minimum slope value. And in other words, we can state that the high slope value implies high wear occurred in the specimen.

Then these samples were tested by the 3D microscopic to have a further idea about the worn surfaces after the pin-on-plate process, and the results were like the following figure:

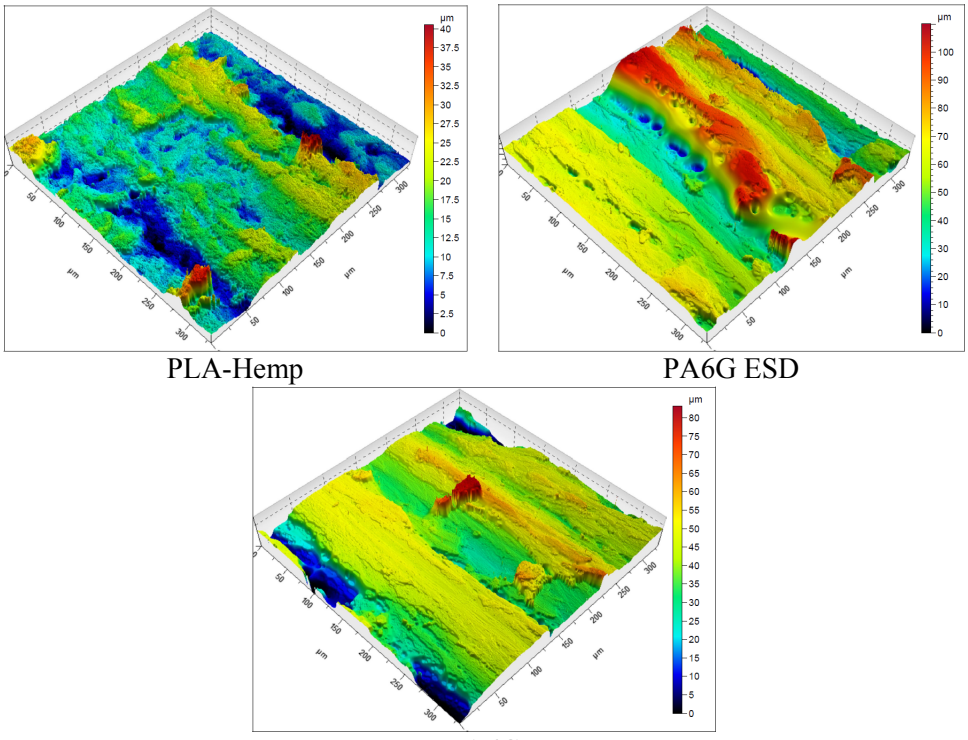

Figure 6. 3D microscopic photos for the worn surfaces of the materials

And as results for these photos, we got the following table:

Table 4. The Height Parameters of the worn surfaces according to ISO 25178

	PLA-Hemp	PA6G ESD	PA6G
Sq (μm)	6.13743	19.19280	12.46001
Ssk	0.55912	-0.14405	-1.15040
Sku	3.32444	3.01320	5.04750
Sp (μm)	26.97496	50.71683	41.84994
Sv (μm)	13.55743	59.39984	41.30695
Sz (μm)	40.53239	110.11667	83.15689
Sa (μm)	4.90134	15.10862	9.32774

From the previous table we can recognise that:

- The height distribution is skewed below the mean plane for PLA-Hemp since Ssk value is more than zero, while for PA6G ESD and PA6G the height distribution is skewed above the mean plane since Ssk is less than zero.
- The sharpness of the roughness profile of the PA6G is the most spiked then PLA-Hemp since Sku values are more than 3, while PA6G ESD had a normal distribution since the value is almost 3.
- PA6G ESD had the highest peak within the defined area as 50.71683 μm, while PLA-Hemp had the lowest as 26.97496 μm.
- PA6G ESD also had the most considerable pit height as 59.39984 μm. Also, PLA-Hemp had the lowest one as 13.55743 μm
- The Maximum height where for PA6G ESD as 110.11667 μm, which is the sum of largest peak height value and the largest pit depth value, but the minimum height was for PLA-Hemp material as 40.53239 μm.
- PA6G ESD also had the highest arithmetic mean of the absolute value of the height from the mean plane of the surface as 15.10862 μm, while PLA-Hemp material had the lowest as 4.90134 μm.

As a result of the previous points, we can see that the PA6G ESD was the most outstanding worn surface, and that is obvious also according to the surface photo.

To have a further idea of this test, we took a new PA6G ESD specimen, and we change some parameters to see the effect of them and how the microscopic photo will change.

We changed the load and the speed; then we had the same process as calculating the wear and the 3D microscopic photo.

In the following two figures, we can see the wear for PA6G ESD in two cases, in the first one the speed is 0.0315 m/s and the load is 9.81 N. While in the second one, the speed is 0.0557 m/s, and the load is 49.05 N.

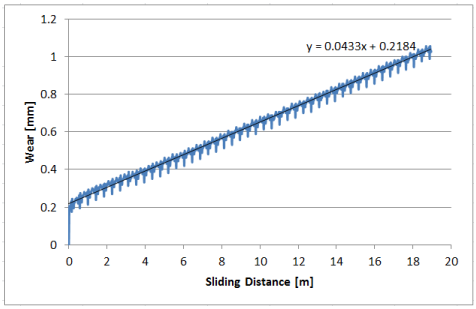

Figure 7. The relation between the wear and sliding distance for a PA6G ESD specimen, where speed is 0.0315 m/s and the load is 9.81N

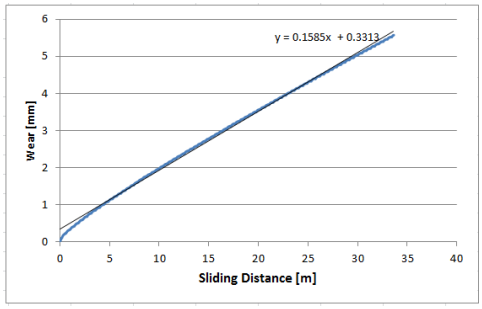

Figure 8. The relation between the wear and sliding distance for a PA6G ESD specimen, where speed is 0.0557m/s and the load is 49.05N

By comparing the two figures, we can see that by increasing the load and increasing the speed, the wear values will increase.

And we checked the surfaces after that. The following two figures, we can see the worn surfaces for PA6G ESD in the same two cases.

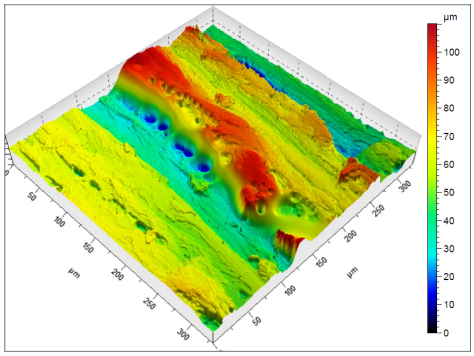

Figure 9. The worn surface of PA6G ESD specimen, where speed is 0.0315 m/s, and the load is 9.81 N

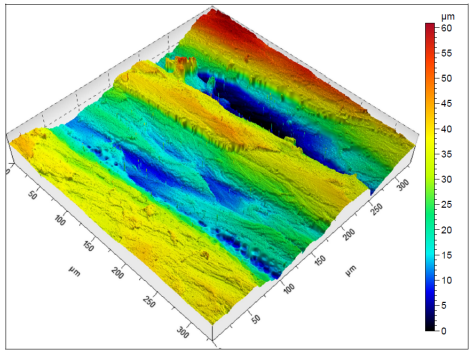

Figure 10. The worn surface of a PA6G ESD specimen, where speed is 0.0557 m/s, and the load is 49.05 N

And as results for these photos, we got the following table

Table 5. The Height Parameters of the worn surfaces according to ISO 25178

	PA6G ESD (0.0315 m/s and 9.81 N)	PA6G ESD (0.0557 m/s and 9.81 N)
Sq (µm)	19.19280	12.75325
Ssk	-0.14405	-0.00445
Sku	3.01320	2.16308
Sp (µm)	50.71683	33.51800
Sv (µm)	59.39984	27.36918
Sz (µm)	110.11667	60.88718
Sa (µm)	15.10862	11.11797

From the previous table we can recognise that:

- In both cases, the height distribution is skewed above the mean plane since Ssk is less than zero.
- The sharpness of the roughness profile in the first casein in a normal distribution since the value is almost 3, while in the second one is skewed above the mean plane because Sku is less than 3.
- The first case a higher peak within the defined area than the second one.
- Also had a more considerable pit depth than the second one.
- The Maximum height was in the first case also not for the second.
- Also, the highest arithmetic mean of the absolute value of the height from the mean plane of the surface for the first was higher than the second.

As a result form both of pin-on-plate and the 3D microscopic photos, we can say that increasing the load and increasing the speed will lead to increase the wear values, but that will give us a smoother surface compared to the first case.

Conclusions

A different polymers type were used and showed and the effects of various parameters on working performance.

In this work, many factors have been studied to test to show their effects on the general performance, like polymers types, the speed of friction, the applied loads.

At the end of this research give some suggestion that PA6G was the best choice of these use polymers because it had the lowest wear rate and how the mentioned parameters could affect the wear process during the day working.

Also, we got that by increasing the load and increasing the speed, the wear values will increase.

While for the 3D microscopic photos, we had a great idea about the worn surfaces. The PA6G ESD was the most outstanding worn surface.

As a result form both of pin-on-plate and the 3D microscopic photos, we can say that increasing the load and increasing the speed will lead to increase the wear values, but that will give us a smoother surface compared to the first case.

References

[1] Mishra, V. (2014). Physical, mechanical and abrasive wear behaviour of jute fiber reinforced polymer composites. Doctoral dissertation, National Institute of Technology, India.

[2] Blahunka Z., Bártfai Z. et.al. (2013): New method for soil surface roughness measurement. Synergy Conference 2013, Gödöllő. full article, pdf

[3] Sawpan, M. A., Pickering, K. L., Fernyhough, A. (2011). Improvement of mechanical performance of industrial hemp fiber reinforced polylactide biocomposites. Composites Part A: Applied Science and Manufacturing, 42, pp. 310-319.

[4] Kim, S. H., Park, C. H. (2017). Direct impregnation of thermoplastic melt into flax textile reinforcement for semi-structural composite parts. Industrial Crops and Products, 95, pp. 651-663.
[5] La Mantia, F. P., Morreale, M. (2011). Green composites: A brief review. Composites: Part A, 42, pp. 579-588.
[6] Khondker, O.A., Ishiaku, U.S., Nakai, A., Hamada, H. (2006). A novel processing technique for thermoplastic manufacturing of unidirectional composites reinforced with jute yarns. Composites Part a-Applied Science and Manufacturing, 37, pp. 2274-2284.
[7] Biron, M. (2013). Outline of the Actual Situation of Plastics Compared to Conventional Materials. Thermoplastics and Thermoplastic Composites 2nd ed. Oxford, UK: William Andrew Publishing, pp. 1-29.
[8] Ellis, K. A., Pritzker, M. D., Fahidy, T. Z. (1995). Modeling the Degradation of Scanning Electrochemical Microscope Images Due to Surface Roughness. Analytical Chemistry, 67, 24, pp. 4500-4507.
[9] Nasrullah, J., Tyler, G.L., Nishi, Y. (2005). An Atomic Force Microscope Study of Surface Roughness of Thin Silicon Films Deposited on SiO2, IEEE Transactions on Nanotechnology, 4, 3, pp. 303-311.
[10] Tholt, B., Miranda-Júnior, W. G., Prioli, R., Thompson, J., Oda, M. (2006). Surface Roughness in Ceramics with Different Finishing Techniques Using Atomic Force Microscope and Profilometer. Operative Dentistry, 31, 4, pp. 442-449.

Evaluation of 3D printing process of testing samples using DLP and FDM techniques

Muammel M. HANON, László ZSIDAI
Department of Maintenance of Machinery,
Institute for Mechanical Engineering Technology

Abstract

Fused deposition modelling (FDM) and digital light projection (DLP) technologies have been used for three-dimensional (3D) printing of tensile and tribology test specimens. Several print parameters were examined during the process of utilised methods. The performance of the two employed 3D printers in the present work was evaluated according to the production speed, materials used, properties of the printed pieces, and geometrical and economical aspects. These assessed sides were based on the observations meanwhile the experiment. Further, the operation procedures, as well as the options of print settings of both methods, have also been detailed. Lastly, all important considerations of the tested methods have been compared.

Keywords

Additive manufacturing, 3D printing options, Fused deposition modelling, Digital light projection, Testing specimens printing

1. Introduction

Three-dimensional (3D) printing is one of the additive manufacturing (AM) technologies. It is also known as additive fabrication, additive processes, direct digital manufacturing, rapid prototyping, rapid manufacturing, layer manufacturing and solid freeform fabrication (ASTM International, 2013). This technology was developed by Charles Hull in 1986 in a process known as stereolithography (SLA) (Jacobs, 1992), which was followed by numerous novel AM processes development over the span of more than 20 years include, among others, Laminated Objective Manufacturing (LOM) (Feygin and Hsieh, 1991), Fused Deposition Modelling (FDM) (Comb, Priedeman and Turley, 1994), Selective Laser Sintering (SLS) (Beaman *et al.*, 1997), and Laser Metal Deposition (LMD) (Mazumder, Schifferer and Choi, 1999).

The applications of 3D printing have incredibly increased in different industries at the last decade (Busachi *et al.*, 2017). Many factors have facilitated this growing such as; inventing various technologies and techniques of 3D printing (Srinivas and Babu, 2017), involving diverse materials (Singh,

Ramakrishna and Singh, 2017), and the decrease in the price of printers (Rayna and Striukova, 2016). As well as several advantages of this new technology include; the desire to the personalisation (manufacturing your goods yourself), and complexity handling (create complex internal structures that would be impossible to achieve with traditional moulded or cast parts) (Attaran, 2017). Whereas the high costs and time-consumption of the AM process remain to be a significant obstacle that inhibits mass production. Void formation results in porosity which can reduce the mechanical performance of the printed products (Bourell *et al.*, 2017).

A wide range of Materials in the forms of filaments, wire, resin, powder, paste, sheets and inks can be used for 3D printing include metals, polymers, ceramics and composites (Takezawa and Kobashi, 2017). Polymers are considered as the most common materials in the 3D printing industry due to their diversity and ease of adoption to different 3D printing processes.

In the present research, 3D printed polymer specimens (for tensile and tribology tests) are produced by two different printing technologies (FDM-Fused Deposition Modelling and DLP-Digital Light Projection). During fabricating the samples, several options of process settings have been examined. Among the tested options, print orientation and angle, the thickness of the layer, and infill percentage. Evaluation for the printing technologies by applying various parameters has been carried out. The features and disadvantages of both accomplished methods were compared.

2. 3D printing methods

There are seven categories of additive manufacturing processes have been defined by ASTM International in their standard terminology for additive manufacturing technologies (ASTM International, 2013), These categories are, binder jetting, directed energy deposition, material extrusion, material jetting, powder bed fusion, sheet lamination, and vat photopolymerization. The process of 3D printing begins with a meshed 3D computer model that can be created by acquired image data or structures built in computer-aided design (CAD) software. An STL file extension is commonly created. A software will be further used for slicing the model into layers, these layers are sent to the printing machine (Ligon *et al.*, 2017). The basic principles of the additive manufacturing process are demonstrated in Figure 1.

Fused deposition modelling (FDM) (alias fused filament fabrication - FFF), falls into the material extrusion category. FDM is currently the most applied AM technology, its printers work by controlled extrusion of thermoplastic polymer filaments to 3D print layers (layer by layer) of materials and then solidify into final parts (N. Turner, Strong and A. Gold, 2014). Thermoplastics such as acrylonitrile butadiene styrene (ABS) (Sun *et al.*, 2008), polycarbonate (PC) (Garcia *et al.*, 2012), and polylactic acid (PLA) (Tymrak, Kreiger and Pearce, 2014), are commonly used due to their low melting temperature.

Digital light processing (DLP) can be grouped into the vat photopolymerization category, where liquid photopolymer in a vat is selectively cured by light-activated polymerisation. DLP uses a digital light projector screen to flash a single image of each layer all at once (or multiple flashes for larger parts). Therefore the print can be achieved very fast in this method (Redwood, Schöffer and Garret, 2017).

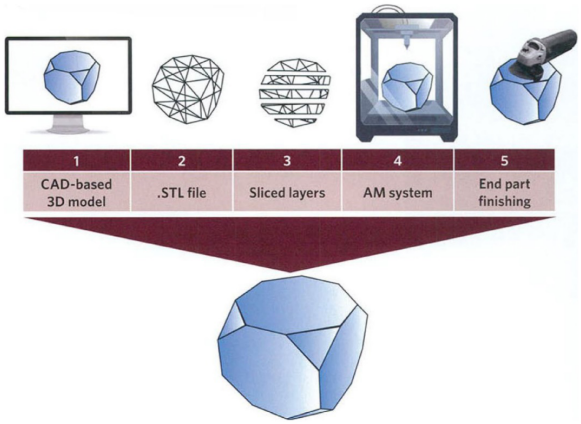

Figure 1. Basic principles of additive manufacturing (Dizon *et al.*, 2018)

3. The used 3D printing machines

The printed test pieces were made with two different 3D printers work according to the FDM and DLP technologies. The models of the used 3D printers are WANHAO duplicator 6 for the FDM and WANHAO D7 for the DLP, which are exhibited in Figures 2 and 3 respectively.

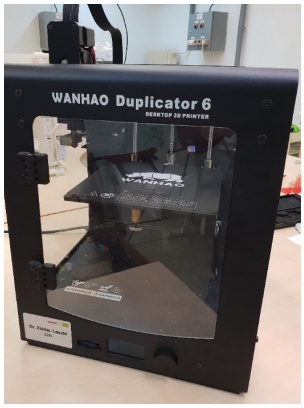

Figure 2. The FDM 3D printer WANHAO duplicator 6

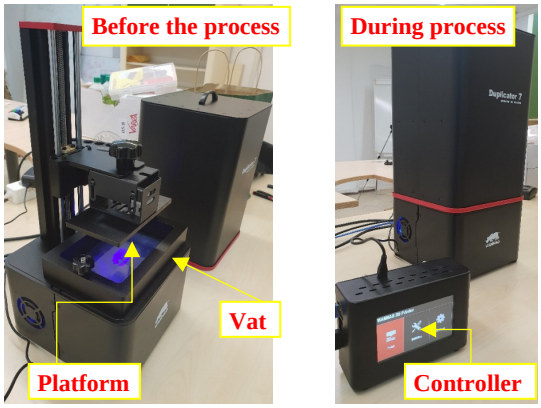

Figure 3. The DLP 3D printer WANHAO D7

For the FDM 3D printer WANHAO duplicator 6, the G-Code of the 3D model can be incorporated directly from the SD card. The model could be designed using any CAD software, which is in this case Solid work software. The file must be saved as "stl" format due to it is compatible with most slicing programs. Simplify3D software was used as a slicer for this work. The FDM printing technology utilises the materials in a filament form.

Regarding the DLP 3D printer WANHAO D7, all parameters and commands could be given from a supplement controller supplied with the printer (Shown in Figure 3). For the slicing purpose, CreationWorkshop software used which is the recommended and prepared for the same printer. "cws" format is the file extension that can be recognisable by the controller. The model file can be uploaded to the controller using a pen drive. The material that employed for the DLP printing is the so-called resin which is a chemical liquid curable by light.
The Technical specifications of both 3D printers (FDM WANHAO duplicator 6 and DLP WANHAO D7) are listed in Table 1.

Table 1. Technical specifications of the used printers

Specifications	**WANHAO duplicator 6 (FDM)**	**WANHAO D7 (DLP)**
Technology	FFF (Fused Filament Fabrication)	DLP LCD printer
Printing materials	PLA, ABS, PVA, PEVA and HIPS	405 nm Resin
Printable volume	200x200x175 mm	120.96*68.5*180 mm
Layer thickness	50 - 400 μm	35-100 μm
Material form	Filament diameter of 1.75 mm	Resin
Heating or curing source	Extrusion nozzle (0.4 mm)	5.5 inch LCD, 405 nm UV lamp
Port	USB 2.0 or SD card	USB 2.0 and HDMI from the computer or the controller
Print speed	30-150 mm/s	30 mm/hour (in height)
Operating temperature	180-260 °C	23 °C
Ambient operating temperature	15-32 °C	23 °C
Position precision	X: 12.5 μm, Y: 125 μm and Z: 5 μm	X: 0.01 μm, Y: 0.01 μm, Z: 4 μm

4. Options of the utilised printing technologies

Once the STL file of the model completed, it is imported to the previously mentioned slicing programs, where a variety of settings can be chosen. These settings are expected to affect the properties of the finished object. The examined options in this work of each printing method are explained in the following.

4.1. FDM 3D printing options

With the assistance of the slicing software, there are different settings have been examined when printing the test pieces using the FDM printer. The primary investigated options are the print orientations (Flat "X", On-edge "Y", and Upright "Z" at 45/-45 raster direction angle) and raster direction angles (0°, 45°, 90°, crossed 45/-45 at Flat "X" print orientation) which shown in Figure 4 (a) and (b).

Raster direction means, the orientation of the extruder head when filling the printing material within the contour of the printed part. The angle of the raster directions of the test piece with the longitudinal axis can be adjusted to any value. Also, successive layers may have different orientations. So, there is a possibility of variation, e.g. if the raster direction angle of the first layer is 45° the second could be built at -45°. When printing with various raster directions, A Flat print orientation was applied. While for the varying of print orientation, the raster direction was set as crossed +45/-45°.

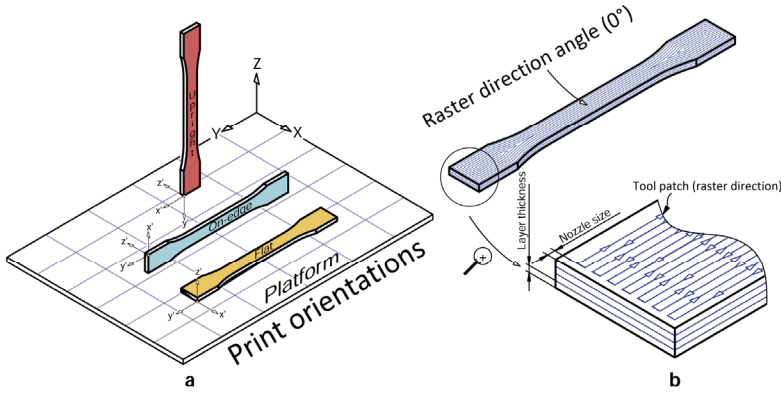

Figure 4. Printing settings of the FDM method: (a) Print orientations (b) Raster direction angle at 0°, and layer thickness (Chacón *et al.*, 2017)

4.2. DLP 3D Printing options

The print orientation angle and layer thickness are the main parameters that can be varied in the DLP printing process of the test specimens. These parameters are expected to influence the results of the subsequent tests (Tensile, tribology, bending, impact, and surface roughness). Three print orientation angles are tested in this work (0, 45, and 90°). Three optional layer thicknesses are offered by the used printer and the slicing program which are 35, 50 and 100 µm. When the examined parameter is the orientation angle, the layer thickness is set as 100 µm. While for investigating the thickness of the layer, the orientation angle is fixed at 0°. Figure 5 displays tensile test specimens and tribology samples are set to be printed in different orientation angles. Table 2 summarises all the examined parameters.

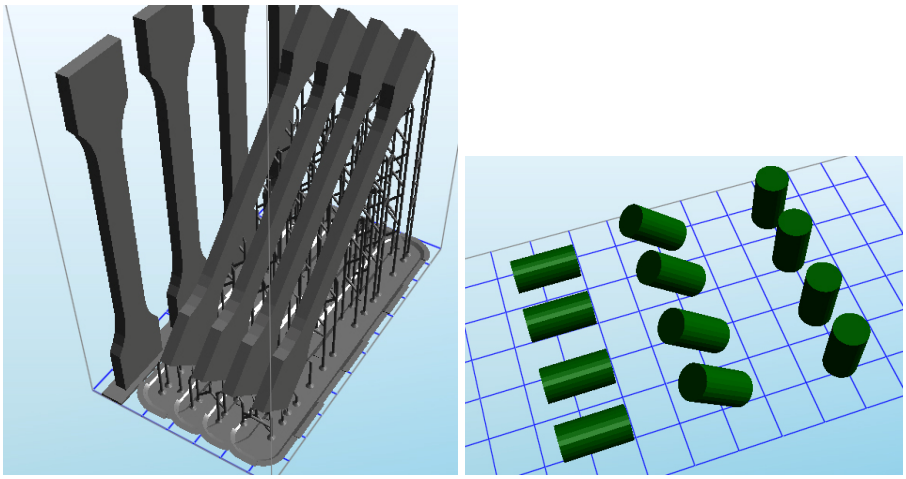

Figure 5. DLP Print orientation angles of tensile test pieces (left) and tribology samples (right)

Table 2. Summary of the experimental settings plan for printing the tensile test pieces

Parameter	**FDM Variables**		**DLP Variables**	
	Raster direction	⁂ Orientation	Orientation angle	Thickness
Raster angle	*0°, 45°, 90°, crossed +45/-45°	X	**-	**-
Orientation	crossed +45/-45°	*X, Y, Z	*(0°, 45°, 90°) at Y	0° at Y
Thickness	200 µm	200 µm	100 µm	*35, 50, 100 µm

*The variables of each examined set.

⁂ When X, Y, Z mean Flat, On-edge, and Upright print orientations consecutively.

**No raster direction in the DLP technology, since every layer is built once after it exposes to the UV light.

5. Preparation of printing the samples

5.1. Preparation of tensile test specimens

The tensile test specimens are modelled according to ISO 527-2: 2012 standard (International Organization for Standardization, 2012) type 1B specimens. The FDM and DLP 3D printers are employed to print the specimens of the tensile test. An identical number of (three) specimens of each used material are printed with different settings, i.e. for each individual print setting, three similar samples have been investigated. Figure 6 presents the printed specimens for tensile measurement with different orientation angles using DLP technology.

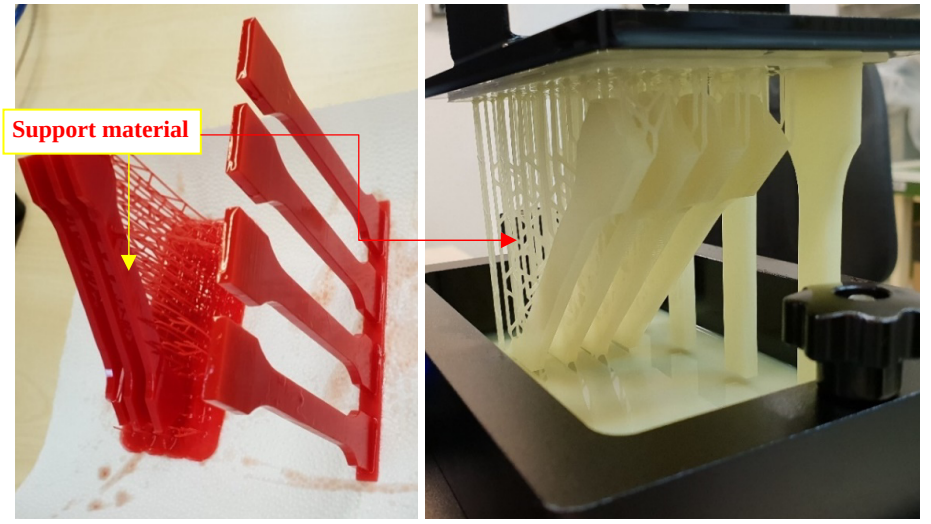

Figure 6. Tensile test specimens printed in 45° and 90° orientation angles using DLP

5.2. Preparation of Tribology specimens

The 3D printed specimens for tribology test have a diameter of 8 mm and a length of 15.2 mm. Some sets of tribology test pieces printed in various orientations using FDM are exhibited in Figure 7.

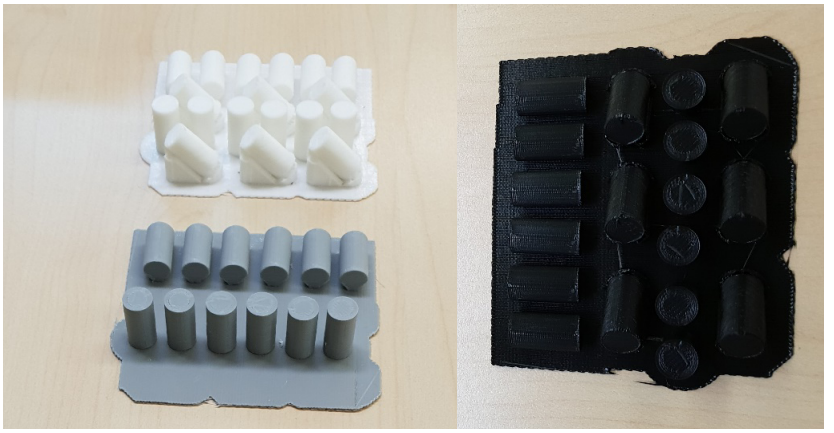

Figure 7. Some sets of tribology test specimens printed in various orientations using FDM

6. Evaluation of the DLP and FDM techniques

Evaluation regarding numerous important considerations among the employed 3D printers has been illustrated in Table 3.

Table 3. Evaluation of the used 3D Printers

	Considerations	Evaluation of the 3D printing technology	
		FDM	DLP
Cost	Machine	●	●
	Material	●	◖
	Operation	●	◖
	Services	●	●
Geometrical properties	Accuracy	◖	●
	Printable size	◖	○
	Complexity	◖	●
	Possibility of print hollow shaps	◖	●
Materials	Composites among layers	*◖	○
	Different colours among layers	*◖	○
	Support material	◖	●
Properties of the products	Durability	●	○
	Mechanical properties	◖	○
	Surface roughness	○	◖
Other considerations	Print settings variety (options)	●	◖
	Print speed	○	●
	Postprocess	No need	**◖
	Material form	Filament	Resin
	Machine size	●	●

Note: ● good; ◖ medium; ○ weak

*When using more than one extrusion head. **DLP Postprocessing starts with removing the excess resin using Alcohol, then irradiating the printed products by UV light for a while.

Conclusion

Evaluation of two 3D printing technologies which are FDM and DLP has been carried out. This evaluation was done based on the experimental work of printing tensile and tribology test specimens using both mentioned methods. Many considerations have been compared regarding the aspects of the cost, geometry, materials, and properties of the printed parts as well as the characteristics of the operation and machines. The analysis of the examined parameters proves that an assessment is not easy when trying to specify which 3D printing technique is better. Since both methods demonstrated privileges in some considerations and defects in others. Therefore, it depends on the application and the desired needs. So, among the used techniques, when the durability and mechanical properties are matter, for sure the FDM technology is

the best choice. Whereas, the DLP method is the most preferable when the print speed and accuracy are required. Both 3D printers used showed somehow low cost in general whether about the consumables or the machine itself.

Acknowledgement

This work was supported by the Stipendium Hungaricum Programme and by the Mechanical Engineering Doctoral School, Szent István University, Gödöllő, Hungary.

References

[1] ASTM International (2013) 'F2792-12a - Standard Terminology for Additive Manufacturing Technologies', *Rapid Manufacturing Association*, pp. 10–12.
[2] Attaran, M. (2017) 'The rise of 3-D printing: The advantages of additive manufacturing over traditional manufacturing', *Business Horizons*. 'Kelley School of Business, Indiana University', 60(5), pp. 677–688.
[3] Beaman, J. J. *et al.* (1997) *Solid Freeform Fabrication: A New Direction in Manufacturing*, *Jom*. doi: 10.1007/978-1-4615-6327-3.
[4] Bourell, D. *et al.* (2017) 'Materials for additive manufacturing', *CIRP Annals - Manufacturing Technology*. CIRP, 66(2), pp. 659–681.
[5] Busachi, A. *et al.* (2017) 'A review of Additive Manufacturing technology and Cost Estimation techniques for the defence sector', *CIRP Journal of Manufacturing Science and Technology*. CIRP, 19, pp. 117–128.
[6] Chacón, J. M. *et al.* (2017) 'Additive manufacturing of PLA structures using fused deposition modelling: Effect of process parameters on mechanical properties and their optimal selection', *Materials & Design*, 124, pp. 143–157.
[7] Comb, J. W., Priedeman, W. R. and Turley, P. W. (1994) 'FDM technology process improvements', in *Proceedings of Solid Freeform Fabrication Symposium*. Austin: Stratasys, Inc., pp. 42–49.
[8] Dizon, J. R. C. *et al.* (2018) 'Mechanical characterization of 3D-printed polymers', *Additive Manufacturing*. Elsevier B.V., 20, pp. 44–67.
[9] Feygin, M. and Hsieh, B. (1991) 'Laminated object manufacturing: A simpler process', in *Proceedings of the 2nd Solid Freeform Fabrication Symposium (SFF)*. Austin: TX, pp. 123–130.
[10] Garcia, C. R. *et al.* (2012) '3D PRINTING OF ANISOTROPIC METAMATERIALS', *Progress In Electromagnetics Research Letters*, 34, pp. 75–82.
[11] International Organization for Standardization (2012) *ISO 527-2:2012: Plastics - Determination of tensile properties - Part 2: Test conditions for moulding and extrusion plastics*.
[12] Jacobs, P. F. (1992) *Rapid Prototyping & Manufacturing: Fundamentals of Stereolithography*. Dearborn: SME publication.

[13] Ligon, S. C. *et al.* (2017) 'Polymers for 3D Printing and Customized Additive Manufacturing', *Chemical Reviews*, 117(15), pp. 10212–10290.
[14] Mazumder, J., Schifferer, A. and Choi, J. (1999) 'Direct materials deposition: Designed macro and microstructure', *Materials Research Innovations*, 3(3), pp. 118–131.
[15] N. Turner, B., Strong, R. and A. Gold, S. (2014) 'A review of melt extrusion additive manufacturing processes: I. Process design and modeling', *Rapid Prototyping Journal*, 20(3), pp. 192–204.
[16] Rayna, T. and Striukova, L. (2016) 'From rapid prototyping to home fabrication: How 3D printing is changing business model innovation', *Technological Forecasting and Social Change*. Elsevier B.V., 102, pp. 214–224.
[17] Redwood, B., Schöffer, F. and Garret, B. (2017) *The 3D printing handbook : technologies, design and applications*. 3D Hubs B.V.
[18] Singh, S., Ramakrishna, S. and Singh, R. (2017) 'Material issues in additive manufacturing: A review', *Journal of Manufacturing Processes*. The Society of Manufacturing Engineers, 25, pp. 185–200.
[19] Srinivas, M. and Babu, B. S. (2017) 'A Critical Review on Recent Research Methodologies in Additive Manufacturing', *Materials Today: Proceedings*. Elsevier Ltd, 4(8), pp. 9049–9059.
[20] Sun, Q. *et al.* (2008) 'Effect of processing conditions on the bonding quality of FDM polymer filaments', *Rapid Prototyping Journal*, 14(2), pp. 72–80.
[21] Takezawa, A. and Kobashi, M. (2017) 'Design methodology for porous composites with tunable thermal expansion produced by multi-material topology optimization and additive manufacturing', *Composites Part B: Engineering*, 131, pp. 21–29.
[22] Tymrak, B. M., Kreiger, M. and Pearce, J. M. (2014) 'Mechanical properties of components fabricated with open-source 3-D printers under realistic environmental conditions', *Materials and Design*. Elsevier Ltd, 58, pp. 242–246.

Tribological behaviour of electrically conductive and self-lubricating cast polyamide 6 composites

Miklós ODROBINA, Ádám SARANKÓ, Gábor KALÁCSKA,
Róbert Zsolt KERESZTES
Department of Maintenance of Machinery
Institute for Mechanical Engineering Technology

Abstract

In this study, tribological properties of ESD (Electrostatic discharge) protective PA 6 (polyamide 6), self-lubricating PA 6 and ESD protective self-lubricating PA 6 were investigated. The tribometer used in the test is capable of pin-on-disc measuring within all possible layout known in tribology practice. The pin was a specimen made from examined materials, always in contact with a rotating general-purpose carbon steel (S355) disc under a load. The matrix material was cast PA 6 in all cases. In the case of ESD protective PA 6, the additive was carbon black while ondina oil was added for self-lubricating properties. The third material also contains carbon black and ondina oil. Sliding diagrams were used to illustrate the coefficient of friction in the function of sliding distance. We used the same parameters for all materials to compare them. As a result, we found the carbon black additive was good for earlier steady-state. In the case of self-lubricating PA 6, the oil particles in the material prevent the rapid formation of the transfer film layer. ESD protective self-lubricating PA 6 has the best performance according to sliding diagrams. This composite material has the lowest coefficient of friction value with this test setup.

Keywords

polyamide 6, ESD cast polyamide, self-lubricating polyamide, pin-on-disc test, electrically conductive plastics,

1. Introduction

Electronic components and products are susceptible to damage from electrostatic discharge (ESD). Protection against electrostatic discharge is a fundamental requirement in many cases for advanced electronic equipment. The annual losses in products containing sensitive electronic components due to ESD during manufacturing, assembly, storage and shipping has been estimated in billions of dollars [Singh, El-Khateeb, 1994]. An ESD control system should be introduced in production and other processes to reach savings of billions of dollars.

International standards demanding ESD protection also increase the awareness of and the need for ESD protection. A variety of materials has been

developed to manufacture sensitive electronic devices and prevent damage during manufacturing and storage. Materials for electronic components are classified according to their surface resistivity as being either conductive, dissipative or insulative. According to standards, conductive materials have a surface resistivity of less than 1 $x10^5$ Ω/sq; dissipative materials have a surface resistivity between $1x10^5$ and $1x10^{12}$ Ω/sq and insulative materials have a surface resistivity greater than $1x10^{12}$ Ω /sq. According to many articles, in ESD protected environments the optimal surface resistivity is in the range of 10^6..10^9 Ω /sq. If the article is capable of dissipating charge fast enough then higher values may be accepted. An uncontrolled discharge can result in too high surface resistivity [Vakiparta, 1995; Cambell, Tan, 1995]. Static dissipative materials are often used to slow down the charge removal process and prevent a damaging ESD event.

There are some processes by which a polymer or component can be made conductive, static dissipating or antistatic. The conventional methods are painting or coating, and conductive fillers, or the internal or external addition of hygroscopic materials. Electrostatic dissipating thermoplastic compounds have successfully eliminated electrostatic discharge failures in many applications in the electronics industry [Narkis *et al* 1999]. Different conductive filler types can be added to the matrix to achieve conductivity. Three most important conductive fillers are as follows: carbon-based materials such as carbon black (CB) and carbon nanotubes (CNTs), metal powders and their compounds, inherently conductive polymers, e.g. polypyrrole and polyaniline [Hooshmand *et al* 2011; Naarmann, 2000]

It is well known that the raw materials of modern products are already largely supplied by the plastics industry. Due to the demands of the electronics industry, polymers with electrostatically dissipative (ESD) properties have appeared on the market.

For research, another important polymer type with additives is the self-lubricating composite. Self-lubricating characteristics and low cost make polymer materials interesting, particularly for bearings and gears with minor demands. If the bearing and gears require small clearance and higher loads over the entire lifetime, pure polymer materials are less suitable because of their lower mechanical properties. The solution for these functions is the production of compounds, e.g. reinforced with additives because the combination with certain additives may cause a reduction of the coefficient of friction [Franke *et al* 2007].

Cast polyamide 6 (PA6) is a widely used one type of polymers in technical practice, which have ESD and self-lubricated composites with little information in the literature.

In this respect, this paper deals with the tribological properties of three different PA6 composites. Self-lubricating PA6, ESD protective PA6 and ESD protective self-lubricating PA6 were investigated. The tribological properties of the PA6 composites were measured based on the pin-on-disc test method.

2. Method

Materials

Cylindrical specimens were used as pins, which were 18 mm in length and 8 mm in diameter. These specimens were manufactured with a high tolerance, which significantly increases the accuracy of tribology tests. We tested three different types of PA 6 composites which were the following: ESD protective PA 6, self-lubricating PA 6 and ESD protective self-lubricating PA6.

In these three cases, the matrix material was magnesium catalysed cast PA 6 polymer. Among the cast polyamides, thanks to the specially-catalysed manufacturing process, it is distinguished by its uniform structure and toughness. Compared with the extruded natural PA 6, it has higher strength, dimensional stability and abrasion resistance. The materials were produced by Quattroplast Ltd. They call the matrix material DOCAMID 6G-H. These materials were made by gravity casting technology. In the case of ESD protective PA 6, the additive was carbon black, while in the case of self-lubricant PA 6 ondina oil was used as a composite material. Type ESD protective self-lubricating PA 6 contained both above-mentioned additive materials.

Table 1. shows the additive materials of the tested polymer composites in mass percentage.

Table 1. Additives of composite materials

Composite\additives	Ondina oil [m/m %]	Carbon black [m/m %]
Self-lubricating PA 6	2	-
ESD protective PA 6	-	1
ESD protective self-lubricating PA 6	2	1

Table 2. Parameters of tests

Name of parameter	Value
Surface roughness, R_a/R_z [μm]	0,07-0,15/0,48-0,93
Load, F [N]	28
Sliding velocity, v [m/s]	0,01
Time of test, t [min]	60
Path	circle
Ambient temperature, T [C°]	24
Relative humidity, RH [%]	50

The material of the disc was general-purpose carbon steel S355, with a grounded surface. The diameter was 350 mm, with 13 mm thickness. The

surface roughness was 0,07-0,15 µm (R_a) and 0,48-0,93 µm (R_z). Peripheral sliding speed was calculated from the radius of the pin route and the disc revolution.

Method

A frequently used small-scale tribology test method was chosen. This method is based on one-directional sliding friction generated between the face of the specimen and the disc. The specimen was fixed into a holder to prevent any movement. The pin-on-disc type tribology test device is in the workshop of the Institute of Mechanical Engineering Technology at Szent István University. Figure 1. shows the pin-on-disc method.

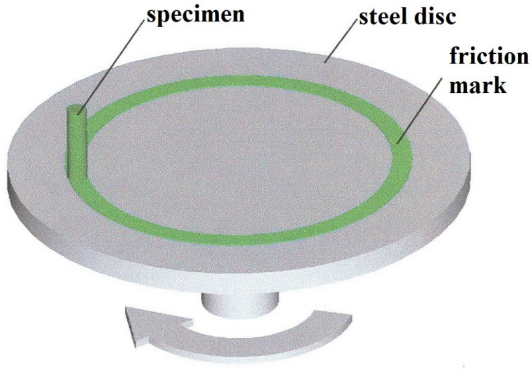

Figure 1. The pin-on-disc test

Tests were performed under pure adhesion conditions without any added lubricant. The friction forces were examined during the tests. Strain gauges found on the force measuring sensor and the Spider 8 measuring amplifier are connected by wire converting the analogue signals to digital, which are transmitted to the computer. The chart-like visualisation of the digital signals was achieved with software called Catman.

After inserting the specimen into the holder, the contact surfaces of the disc and the specimen were cleaned with methylated spirit. During the tests, a diagram from data was monitored, which was displayed on the screen in real time. After completing the test, all data were saved in the appropriate file for later processing, using a spreadsheet.

4. Results

Diagrams were used to illustrate the results. We made the diagrams with software called Microsoft Excel. Tests were repeated twice in all cases, used the same setup. We present only one diagram for each material. Fig 2. shows the

coefficient of friction (Cof) in function of sliding distance in case of self-lubricating PA 6. The value of Cof change between 0,2-0,3. This is a relatively low value due to the added ondina oil. At the beginning of the test, the Cof is decreasing. After this running-in period, we can see a hump in the diagram. That is because of the established transfer layer between the specimen and the disc. It is a common phenomenon in the case of polymer sliding systems. After this phase, the sliding system reaches the steady-state between 0,2 and 0,225 Cof value.

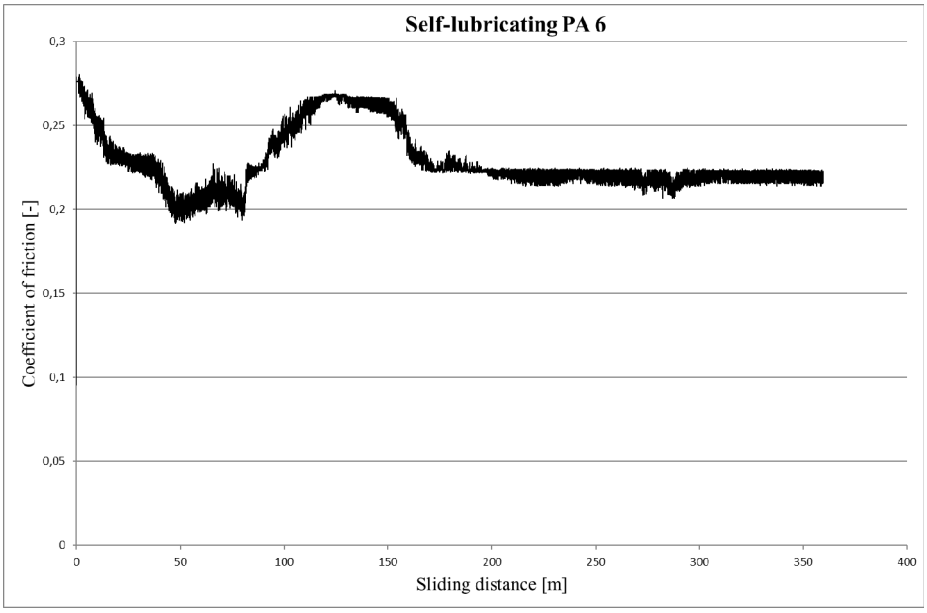

Figure 2. Sliding diagram of self-lubricating PA 6

In Fig 3., the friction diagram of ESD protective PA 6 is presented. In this case, the curve is different compared to the previous diagram. However, in the established steady-state, the Cof takes up almost the same value. After 100 m the Cof is mildly increasing continuously. This material reached the steady-state earlier than the self-lubricated one. We can say the carbon black is better for earlier steady-state.

In Figure 4. we can see the sliding diagram of the ESD protective self-lubricating PA 6. It is easy to see this material is much better than the others. The maximum Cof value is under 0,25. In the beginning, there is a short running-in period. In this period the Cof value is strongly decreasing. After 100 m we can see the steady-state at a low Cof value. Due to the carbon black and ondina oil additives, this material uses the advantages of the previous materials. In this diagram, the curve is thinner, because in the case of this material the sliding was much smoother during the tests.

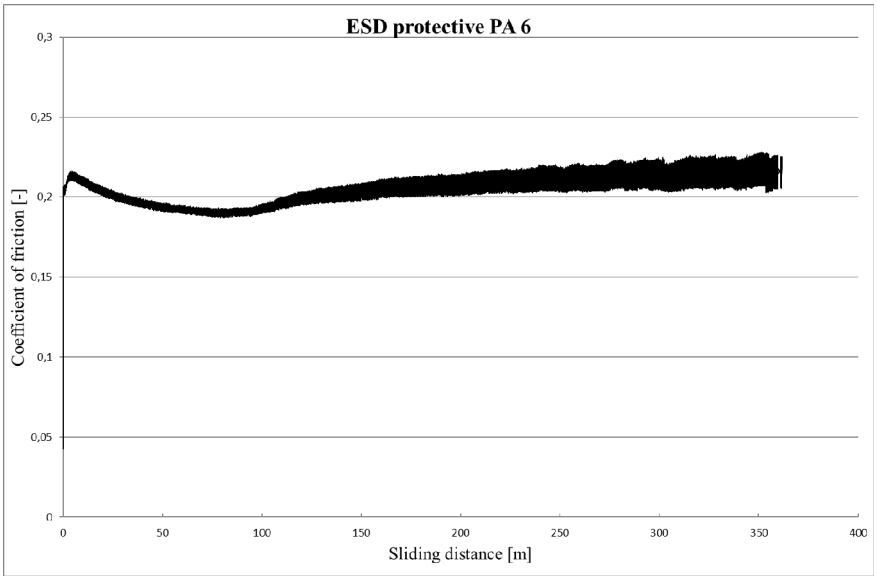

Figure 3. Sliding diagram of ESD protective PA 6

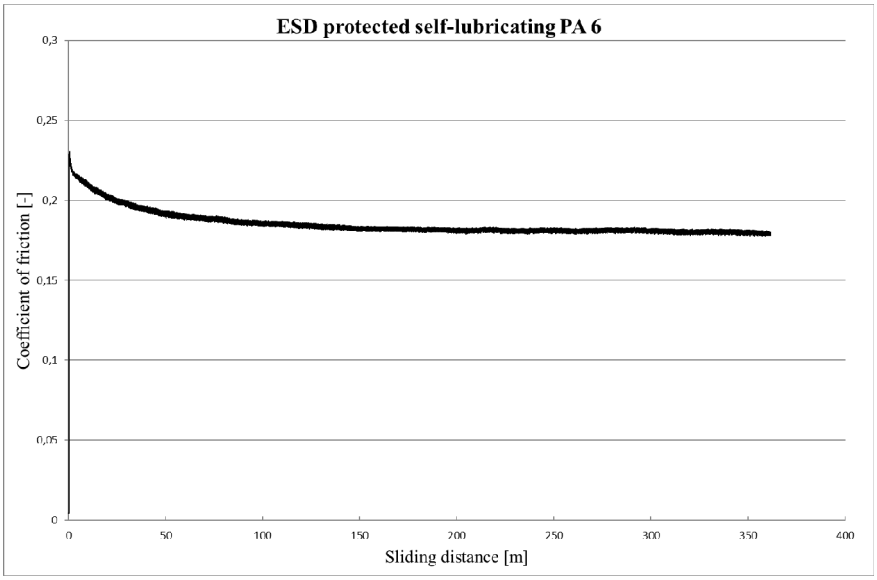

Figure 4. Sliding diagram of ESD protected self-lubricating PA 6

Conclusion

In case of the ESD protective PA 6, the carbon black additives deteriorate the deformation. The deformation ability in the contact zone is the lowest on the given load, which means that the actual contact surface is smaller, it cannot

deform. Deformation components of rigid materials are completely different than though materials. Where actual contact occurs, the specific load will be greater. That is the reason why the sliding properties are better compared to self-lubricating PA 6.

In the case of the self-lubricating PA 6, the sliding system reaches steady-state phase later. A dynamic equilibrium is formed by the release of the polymer film layer, which sticks to the steel and then sticks back to the specimen. This is a blocked phenomenon because the oil particles in the material prevent the rapid formation of the transfer film layer. Therefore, the curve on the sliding diagram is not smooth. The breakaway and the sticking phenomenon depend on the quantity of the ondina oil additive at the contact zone. Because of this, reach the steady-state takes longer time.

The transfer film layer is much easier to form when the carbon black is added, according to the measurement results obtained, but it causes problems in the uniformity of the transfer film layer, as shown by the fluctuation phenomenon. The dynamics of sticks are much stronger, so in the diagrams, the coefficient of friction fluctuates in a larger band but stabilises much sooner.

References

[1] Cambell, R. W., Tan, W. (1995): EOS/ESD Symposium, Phoenix AZ, pp. 218.

[2] Franke, R., Lehmann, D., Kunze, K. (2007): Tribological behaviour of new chemically bonded PTFE polyamide compounds. Wear, Vol. 262, pp. 242-252.

[3] Hooshmand, S., Soroudi, A., Skrifvars, M. (2011): Synthetic Metals, Vol. 161, pp. 1731-1797.

[4] Naarmann, H. (2000): Polymers, Electrically Conducting. Ullmann's Encyclopedia of Industrial Chemistry.

[5] Narkis, M., Lidor, G., Vaxman, A., Zuri, L. (1999): New injection moldable electrostatic dissipative (ESD) composites based on very low carbon black loadings. Journal of Electrostatics, Vol. 47, pp. 201-214.

[6] Singh, S. P., El-Khateeb, H. (1994): Evaluation of a proposed test method to measure surface and volume resistance of static dissipative packaging materials. Packaging Technology and Science, Vol. 7, pp. 283-289.

[7] Vakiparta, K. (1995): EOS/ESD Symposium, Phoenix AZ, pp. 229.

Production of metal-ceramic composite with 3D printing

Tamás PATAKI, Attila KÁRI-HORVÁTH
Department of Material and Engineering Technology,
Institute for Mechanical Engineering Technology,

Abstract

In this work, the production of a metal-ceramic composite produced by 3D printing is presented. In our research, steel, aluminium and copper alloy powders are blended with aluminium oxide ceramic powder and used as a raw material for 3D printing. The prepared specimens are analysed by metallographic examination. By adding ceramics, the strength of the workpiece is significantly reduced. Creating a ceramic composite is a very difficult task with 3D printing technology, because the laser jogs out the ceramic particles from its place. In the process of creating the new composite material, we have made a new recipe for a variety of metals and ceramics. The 1.2709 steel loses its magnetic properties after adding 6% ceramic.

Keywords

3D Metal Printing, CuZn28, Bronze, Tool-steel, 1.2709, AlSi10Mg, Aluminium, Material structure, Strength, Metallography

1. Introduction

At the present day, 3D printing is already widespread in the industry, and we can produce not only metal models but also metal parts. Three-dimensional object can be manufactured using laser melting from metal powders. With 3D metal printing technology, external and internal free surfaces or so-called “impossible design" shapes can be created, which cannot be produced by using traditional manufacturing technologies. The new 3D metal printing technology is better than the traditional 3D printing, as the parts, which are manufactured by this technology, are not only models, but are also ready for use. Components produced by the new technology can directly incorporate into machines after machining.

3D metal printing is the most developed and researched technology nowadays. In the past two decades, the first material used by researchers and manufacturers was the polymer. Polymer 3D printing technology is already well-developed in the designing of products. Szabó I. and Kátai L., are the researchers of Szent István University, who dealt with the issue of planning in Hungary. Hungarian researchers

have carried out comprehensive work in several areas, eg. KÁTAI and his colleagues examined the impact of 3D printing components manufacturing parameters on component strength. As a result of the complex work, Kátai et al. created a CAD manual what can be used in design, so Hungarian engineers can make better use of the possibilities provided by materials. With the development of 3D metal printer technology, manufacturers have been able to produce a large number of automotive parts. The industrial environment is constantly evolving in Hungary, so designers can create increasingly complex geometries. The reconstruction of the complex and complicated surface forms is of great importance to the work of Szabó, Kátai and Csoma R., when the corrections of 3D scanning were analysed. Using innovative technology, engineers are able to develop new designs, since nowadays the automotive industry is most concerned with 3D printing. The Renault Trucks company can produce 25% lighter engines than the factories that manufacture with the conventional process. In various projects, the currently available metal powder alloys were used by engineers. R. Dolan et al. presents a reconstruction design of a 3D printed piston for diesel engines. E. Jakus and others at the University of Chicago, University of Northwestern, have investigated the production and strength of various metals and ceramic composites. John H. Martin et al. examines the strength properties of base materials for aluminium 3D printing. It was found that the strength of the available 3D metal powder for marketable 3D metal printing is much higher than that of conventional casting technologies. They were able to produce new geometries and the weight of the components was reduced.

There are some studies where the top of the piston is coated with ceramics to reduce heat conduction, improving the thermal efficiency of the engine. In the 1980s, american researchers developed a method for supplying internal combustion engine pistons with ceramic inserts, increasing engine efficiency. In 1982, university researchers patented a method of applying a thin layer of ceramic to the top of the piston. The technology did not spread because the coefficient of thermal expansion of the two materials is significantly different. The ceramics applied to the surface of the aluminium plunger are dissipated over time due to thermal expansion.

2. The materials

During the work we used three different types of metal raw materials: steel 1.2709 (X3NiCoMoTi 18-9-5), copper (CuZn 28), aluminium (AlSi10Mg). In the new material, the matrix is made of metal and the additive MARTOXID MDS-6 ceramic. In the course of the research, we created mixtures of different compositions. The mixtures contained 2, 4, 6, 8 10% ceramics.

Steel:
The specimens are made of tool steel X3NiCoMoTi18-9-5 according to DIN 1.2709. This material has very good mechanical properties and can be easily

heat treated. It is a perfect material for casting tool and for high performance mechanical parts as well, such as motorsport or aircraft components. You can also use this material for different cutting tools.

The 1.2709 material behaviour: high tensile strength, high yield strength, good toughness (contraction, elongation, impact, cracking toughness), even at low temperatures, high incision tensile strength, good heat resistance.

Table 1. The chemical composition of the measured steel

C [%]	Si [%]	Mn [%]	P max [%]	S max [%]	Cr [%]	Mo [%]	Ni [%]	Co [%]	Ti [%]	Fe [%]
0,03	0,1	0,15	0,01	0,01	0,25	4,5-5,2	18	9	1	66

Cooper

CuZn28 is a solid solution strengthened copper alloy containing 28% zinc (brass). The alloy has very good cold forming properties and can be brazed and soldered, welding processes need to be executed with care, due to the high zinc content. As the zinc content increases, the strength improves, yet the conductivity and ductility are reduced and the alloy gets more susceptible to stress corrosion cracking if exposed to an ammonia atmosphere, compared to pure copper. If exposed to an ammonia atmosphere, CuZn28 should be stress relieved. Due to the raised zinc content the alloy has economic advantages. Fields of application are metal ware and deep drawing parts, automotive, heat exchangers, connectors, chains, coolers and components of electrical and mechanical engineering.

Table2. The chemical composition of the measured copper alloy.

Cu [%]	Fe max [%]	Zn [%]	Pb max [%]	Al max [%]	Ni max [%]	Sn max [%]
71-73	0,05	26-29	0,05	0,02	0,3	0,1

Aluminium

This material has good mechanical properties and can be used for parts subject to high voltages. The material is durable and lightweight. These behaviours make aluminium AISi10Mg particularly effective in areas where a strength-, mass ratio as well as good thermal properties are required. The parts what are produced SLM AISi10Mg aluminium have excellent properties as the rival some, produced by traditional methods. Additive manufacturing of aluminium parts is often most successful in projects where 3D printing is fully justified, because it is the best production method, compared to other manufacturing techniques (casting, machining, cutting). We have to approve that the 3D printing is often advantageous.

Table 3. The chemical composition of the measured aluminium alloy.

Si [%]	Fe max [%]	Cu max [%]	Mn max [%]	Mg [%]	Ni max [%]	Zn max [%]	Pb max [%]	Sn max [%]	Ti max [%]
9-11	0,55	0,05	0,45	0,2-0,45	0,05	0,1	0,05	0,05	0,15

Ceramic

MARTOXID MDS-6 is a ceramic with high content of aluminium oxide (Al2O3). Especially suitable for the production of wear-resistant parts and products, which are subject to extremely high mechanical, thermal, chemical and electrical loads. Using this ceramic we have the opportunity to produce refractory materials and components.

Table 4. The chemical composition of the measured ceramic.

Al_2O_3 [%]	Na_2O max [%]	CaO [%]	Fe_2O_3 [%]	SiO_2 [%]	Al_2O_3 min [%]
99,8	0,06	0,03	0,4	0,06	95

The following figure shows the distribution diagram of the particles of the ceramic powder, which we used.

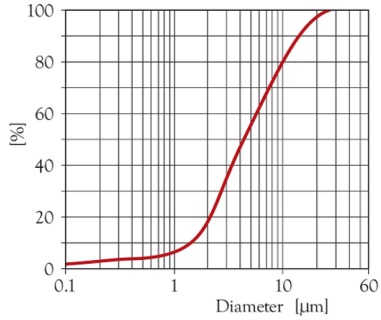

Figure 1. The distribution diagram of the particles of the ceramic powder

The 3D Printer

One reason for metal 3D printing became such an important topic is that the parts can be 3D printed in mass production. It is a fact, that some parts created with metal 3D printing are already so good, if not better, than those manufactured by traditional methods. Many professional users and industries are adopting the metal printing technology to create 3D printed metal prototypes or customised parts on demand.

In this work we used the Thinkspace CL/TST2 Pro 3D printer. The working area of this machine are 200x200x250 mm. This printer use two 200W laser lines. The next figure shows the ways of laser lights. In this work we use the "island" type of laser lighting method.

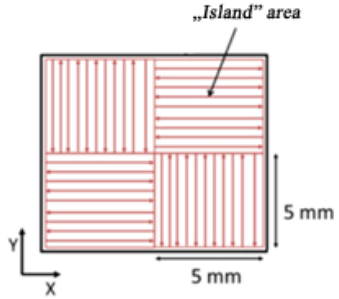

Figure 2. The strategy of laser exposure

3. Method

Metal and Composite material printing is used to create high-precision, mechanically and thermally resilient components. In this process the fine metal powder is locally melted by a high-energy laser. The material will be in one part after cooling.

With the use of 3D printing technology, ceramic thermal particles can be introduced into the piston material. Using the new technology, the ceramic particles are intertwined with the particles of the metal powder that can be melted by the laser sintering technology. Using this method, the advantageous properties of the two materials can be exploited. Using the technology, the material of the piston does not secede with the ceramic, but the two materials become one unit. Ceramic can also be mixed into the side wall of the piston, which reduces the thermal expansion coefficient of the aluminium components. The thermal expansion coefficient of the new composite piston could be brought closer to the steel. Thus, the fitting of the two parts can be reduced, thus improving the efficiency of the engine, making it more economical, environmentally friendly and less consumable. The composite piston can only be produced from dust with 3D deformation technology, unsuitable for conventional manufacturing processes. Ceramic grains cannot be detached from the surface because they are embedded in a matrix material, so the lifetime is not affected by the material used.

Using ceramics as an additive, heat regulating materials can be used in many areas of the industry. For example, the industry could provide new opportunities for the automotive industry. By adding ceramic granules, it is possible to control the thermal properties of the entire structure (thermal conductivity, thermal insulation).

The preliminary assumption of our research was that the high-strength printer materials used in industry are mixed with ceramic powder. Ceramic insulates heat well, therefore the new composite is an insulating material in a metal matrix.

In the powder container of the machine, a pre-blended metal and ceramic material is applied. The particles are irregular but homogeneous. Ceramic grains are larger than the particles of the metal powder. The laser melts the metal which surrounds the ceramic particles. Ceramic granules do not melt, metal fixes them. This method provides a fused composite material that includes the metal and the ceramics too.

During the work we used three different types of metal raw materials: steel 1.2709 (X3NiCoMoTi 18-9-5), copper (CuZn 28), aluminium (AlSi10Mg). In the new material, the matrix is made of metal and the additive MARTOXID MDS-6 ceramic. In the course of the research, we created mixtures of different compositions. The mixtures contained 2, 4, 6, 8 10% ceramics.

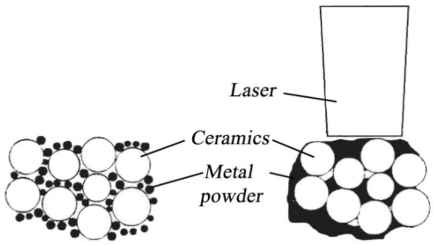

Figure 3. The melting process

4. Results

Metal ceramic composite was created with the Thinkspace CL / TST2 Pro 3D printer. Steel, copper and aluminium were mixed with ceramic powder, which became the raw material. We made up to 10% ceramics in the raw material. We tried to create material containing five different quantities of ceramic powder. Each metal powder was also tested naturally (without ceramic). The printer parameters are set for the particular composition. In all cases, we have optimized the laser performance and the speed of exposure. Our first experience in the production of specimens was that the laser picks out the ceramic particles from the particles of the raw material. The following picture shows that there is a dust layer around the specimens that contains only ceramic particles.

Figure 4. During the printing process, the ceramic particles stick out from their space

During the process, we reduced the laser performance so that the material can merge. Compared to the production of pure metals, the laser performance had to be reduced by 30%. Less laser power results in a reduction in the strength of the specimens as described in a previous study. In this work we examine the structure of the test specimens. Next, we will examine what other parameters (grain size, amount of additive) can improve the properties. Now, we were interested in the structure of materials and the opportunity. Other materials can be embedded in the metal matrix. The following figure shows the metallographic image of the pure metal.

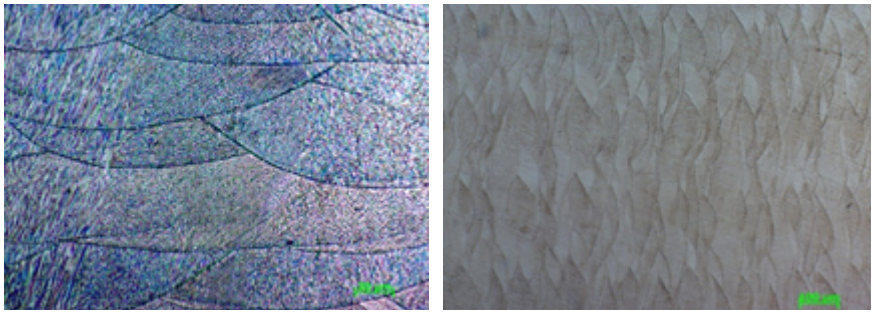

Figure 5. The 1.2709 steel metallographic cross section in 100x and 500x enlargement

The images show that the metal powders have merged and a homogeneous structure has been created, the strength tests have proved that the parameters of the material what we have produced, meet the expectations.

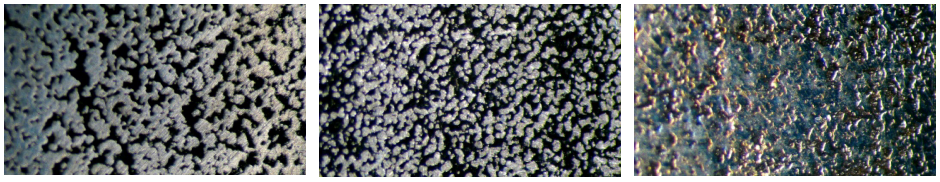

Steel Aluminium alloy Copper alloy

Figure 6. The tree material structure with 10% ceramic

During the experiments, metallographic cross-section was performed on the specimens, on which the fabric structure of the metals was analysed. The maximum ceramics tincture was 10% because if we were to increase it, the strength would be reduced. Above the 10% ceramic content, the specimens disintegrate into pieces. The next picture shows the different materials with the maximum ceramic content. During the illumination of the specimens, a significant amount of the ceramic particles jumped out of the surface, so that the resulting material contained only a small amount of ceramics. In practice, a

foamy structure was created because the ceramic particles were not embedded in the matrix, their place was left empty. In the case of Steel, this spongy lattice metal structure is continuous. However, in the case of aluminium, this metallic structure is highly porous. In the case of copper alloy, it was the same as in the case of steel, because the metallic structure is continuous. The significant reduction in the strength of the test specimens is due to the empty spaces and the surrounding material structure.

Summary

In the present study, the metal powder used for 3D printing was mixed with aluminium oxide ceramics. We have created a new material, a new composite from the mixture. In our examinations it can be stated that up to 10% ceramics can be mixed into the base metals examined. However, a significant part of it moves away from its place of manufacture, creating a material and empty space. In our research, we have proved that ceramic particles can be introduced into metal structures by utilizing 3D printing technology. We pointed out that the applied ceramic at a 10% mixing ratio moves away from the processed surface during laser scanning, thereby obtaining a lattice structure. With the addition of 6% ceramics, the magnetic properties of the steel are already eliminated. It is a further object to examine the properties of these obtained materials. Our aim is also to try to incorporate a smaller particle size of the ceramic into the metallic structures and to re-agitate the mixing ratios. It can be stated that a metal-ceramic composite can be created with 3D metal powder printing technology, but the mixing ratio is very limited.

References

[1] R. Dolan, R. Budde, Dr. Ing R. Rezaei, 3D Printed Piston for Heavy-Duty Disel Engines, 018Ground Vehicle Systems Engineering and Technology Symposium(GVSETS), POWER &MOBILITY (P&M)TECHNICAL SESSION, AUGUST 7-9,2018-NOVI,MICHIGAN, p.8

[2] https://corporate.renault-trucks.com/en/press-releases/metal-3d-printing-technology-of-the-future-for-lighter-and-more-compact-engines.html?q=3d%20printed

[3] L. Kucerová, I. Zetková, Metallography of 3D printed 1.2709 tool steel, Manufacturing Technology, february 2016 Vol. 16, No 2, 140-144

[4] Eric A. Jägle, Zhendong Sheng, Philipp Kürnsteiner, Sörn Ocylok, AndreasWeisheit and Dierk Raabe, Comparison of Maraging Steel Micro- and Nanostructure Produced Conventionally and by Laser Additive Manufacturing, *Materials* 2017, *10*, 8; doi:10.3390/ma10010008, p. 15

[5] E. Jakus, L. Taylor, R. Geisendorfer, C. Dunand, N. Shah Metallic Architectures from 3D-Printed Powder-Based Liquid Inks, Advanced Functional Materials, 16. November. 2015 Volume 25, Issue 45

[6] Szabó I. – Kátai L.: Construction Design and Analysis with Computer Aided Engineering Tools. In: Proceedings of Annual Session of Scientific Papers „IMT Oradea – 2012", Editura Universitatii din Oradea 2012., CD ROM Edition, Volume XI., NR 1/ 2. 135-141. ISSN 1583-0691

[7] Kátai l., Szabó I., Lágymányosi A., Lágymányosi P., Szakál Z.: Additív gyártástechnológiában alkalmazott anyag szilárdsági jellemzőinek vizsgálata a 3D nyomtatás paramétereinek függvényében In: Gép, LXIX. évf. 4. szám, Miskolc, 2018, 45-48. o., ISSN 0016-8572

[8] I. Szabó – L. Kátai – R. Csomai: Application of 3D Scanning in Engineering Design and Analysis In: Mechanical Engineering Research, Volume 7. 2012. p. 81-91. HU ISSN 2060-3789

[9] Kátai et.al.: *CAD Book*. Typotex Kiadó, Budapest, 2012. ISBN 978-963-685-7

[10] John H. Martin, Brennan D. Yahata, Jacob M. Hundley, Justin A. Mayer, Tobias A. Schaedler1 & Tresa M. Pollock, 3D printing of high-strength aluminium alloys, 21 september 2017, VOL 549, NAtUre, doi:10.1038/nature238 , PP 365-380

[11] M.S.Pham, B.Dovgyy, P.A.Hooper, Twinning induced plasticity in austenitic stainless steel 316L made by additive manufacturing, Materials Science and Engineering: A Volume 704, 17 September 2017, Pages 102-111

Institute for Process Engineering

Professor Dr. Péter KISS
Director of the Institute

Dear Reader,

The Institute for Process Engineering - as an important education and research division at the Faculty of Mechanical Engineering - has three units:

Department of Automotive Technology
Department of Energetics and
Department of Measurement Systems.

During our educational and scientific work we paid special respects to the following topics:

- Basic technical knowledge in aspect of engineering approach,
- Engineering thermodynamics, electrical engineering and electronics,
- Basic and applied knowledge of energy conversion, energy utilization and energy economy,
- Special technical knowledge for development of environmental industry and utilization of alternative energy sources,
- Basic and applied knowledge of automotive and off-road techniques and technologies,
- Land locomotion and soil mechanics,
- Disciplines of measurement technology applied in different engineering processes.

Last year we focused the following scientific topics:

- Some aspects of torque transmissibility of dry friction clutches
- Finding the optimal neuron numbers of multilayer artificial neural network models for drying
- Effect of bulk density and moisture content of soil on the penetration resistance and penetration depth
- Pressure regulation in pneumatic tractor tyres

I hope that these papers interest you and if you need more information do not hesitate to contact us.

Finding the optimal neuron numbers of multilayer artificial neural network models for drying

Kornél BESSENYEI, Zoltán KURJÁK, János BEKE
Department of Energetics, Institute for Process Engineering

Abstract

Among several parameters the structure of the artificial neural network can have a significant influence on model performance. If we say structure, we think about how the neurons are connected to each-other and how much of neurons do we need for a proper model. This paper is about some questions that we had to answer while experimenting with artificial neural networks for deep bed drying of tomato pomace.

Keywords

drying, energetics, artificial neural network, semi-empirical model

1. Introduction

Tomato pomace is the by-product of tomato manufacturing and also a raw material for some other processes in the food industry or agriculture. Hungary has good terms in tomato production and achieves a high yield compared to the world and EU average. A rational processing of by-products is desirable.
Using data from the drying experiments with tomato pomace, modelling of the drying process was performed using neural network models. The neural network is basically used as an empirical model for modelling drying. In this case, the connections between the neurons of the network - at the beginning with the same strength - will be strengthened or weakened during the training process. So we get the trained, working model. In general, the empirical models approximate the process from which the data was taken quite good, but their use is limited when the circumstances change. The limits of empirical models can be widened by the use of semi-empirical models. In the case of neural networks, this can be accomplished by adding a priori information to the model by setting and forcing the connections between neurons. The experimental data have a significant impact on the usability of both empirical and semi-empirical models. In the case of neural networks, furthermore, the preparation of data for training, the training method used, and the integration of neurons into layers, the number of layers and the number of neurons per layer, has a significant effect on the performance of the resulting model. Based on our previous experience, the cumulative square error can be used to evaluate the performance of the model, making the models comparable. As a result of random events built into the data preparation and training processes – under the same initial conditions – the training process always results in a somewhat different model. This

means that the effect of the number of layers and the number of neurons per layer cannot be judged by comparing the models obtained by the single training of neural networks of different structures. This is also the case with the comparison of empirical and semi-empirical models. Finding the network structure that produces the optimal model is only possible if the structural changes of the model can be detected significantly in the model's performance. The solution is that the neural network with the selected structure is trained repeatedly. The individual trainings always start from the same initial state and follow the same algorithm. The performance of the models thus obtained is not characterized by the cumulative square error, but by its expected value and standard deviation. I refer to this method as a statistical approach in the followings. This method is applicable to both empirical and semi-empirical models. Evaluation of the results can be done by machine, in algorithmic form, but with human power in tabular or graphical form. We have found that graphical representation is an effective tool for discovering promising structures and drawing general conclusions about the structure.

The model is considered to be given if the network structure, the connection matrices, and the transmission functions are defined by the neuronal attachment structure. If only the network structure is given, it cannot be considered as a model, but as a starting point for providing the optimal model. But in order to do this, the structure must be selected using multiple recurrent statistical methods. It is not enough to refer to the performance of a model obtained by teaching the structure one time, because in extreme cases, the standard deviation of the model performance can be equal to the expected value. In addition to the structure, the training and the data preparation algorithm must be given as they have a significant impact on the usability of the model produced.

The structuring of the neural network is basically done in two ways. At first, by defining the number of layers and the number of neurons per layer. At this point, each neuron in each layer is connected to each neuron in the adjacent layer. This design results in an empirical model. On the other hand, it is possible to define the layers between the layers and the number of neurons per layer by specifying the connections between the layers at the same stage. This allows us to organize the network to a certain extent with known theoretical contexts. These will be semi-empirical models. The hand-made structure can be trained in the same way as above. However, there is a significant difference that the outputs of the intermediate layers are also available.

A semi-empirical model from neural networks can also be made with a composite model created by combining empirical models that are trained separately for known sub-processes. However, this method requires measurement data for the training of each sub-model.

2. Materials and Methods

The measurement data is taken from an experimental drying of tomato pomace in a laboratory dryer. The drying apparatus is a convective batch dryer. The

dried material is placed into the drying chamber on perforated sheet metal trays in three layers. The psychrometric properties of the drying air are measured before and after each layer, the flow rate is measured with an orifice at the duct inlet. The water removal is measured with gravimetric method. For data acquisition five-minute sampling rate was used.

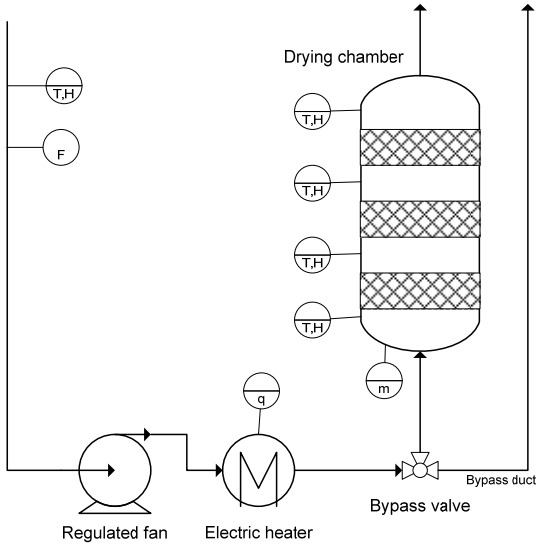

Figure 1. Schematic of the dryer. (T-temperature, H-humidity, F-flow rate, m-mass, q-heat flow)

The wet-base moister content of the raw material was about 80% at the beginning and 6% at the end of the drying experiment. The flow rate of the drying air was 370m^3/h and the temperature was set according to table 1. 2 kg tomato pomes was put on each tray in a 40 mm thick layer.

Table 1. Temperature of the drying air

experiment	**temperature [°C]**
1	40
3	110
5	75
6	55

From the preliminary data analysis four data sets have been chosen for the models: experiment 1, 3, 5 and 6. From these data sets experiment 1 has systematic error, and not used for training the models but for test. It is required that the model shall approximate experiment 1 with a significantly higher error.

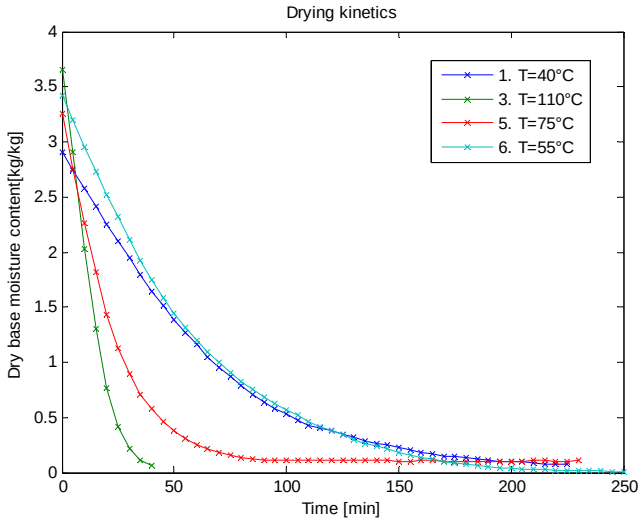

Figure 2. Drying kinetics. The effect of the air temperature.

The first model constructed is purely empirical. We decided to focus on ate simplifies empirical model.

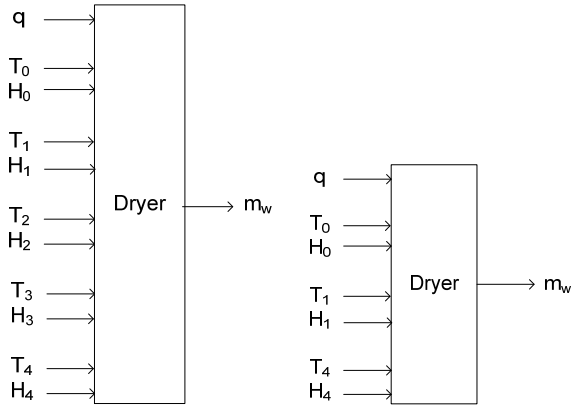

Figure 3. Empirical model of deep bed dryer. Left: complete, right: simplified. (m_w-water removal rate, T_0-ambient air temperature, T_1-air temperature at drying chamber inlet, T_4-air temperature at drying chamber outlet, H_0-ambient air humidity, H_1-humidity at drying chamber inlet, H_4-air humidity at drying chamber outlet)

The semi-empirical model is taking into account that the dryer is made out of a burner and a drying chamber. The connection of the two components is the flow rate of the drying media. The semi-empirical ANN model on figure X is made from the combination of separately trained smaller networks.

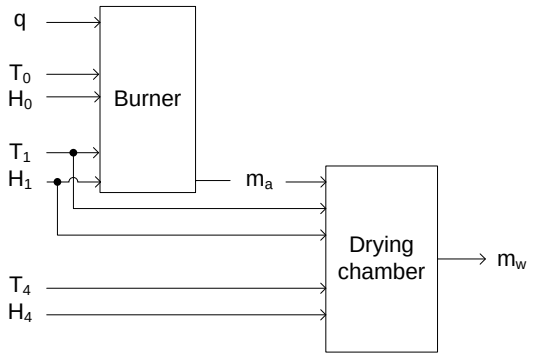

Figure 4. Semi-empirical model of the deep bed dryer.
The composit model. (m_a-flow rate of the drying air)

We also constructed semi-empirical ANN models made from structured analytical neural networks and it is looking for answers to the following questions: Is it possible to construct such a model? Is it possible to find an optimal model? Is it better than the pure empirical?

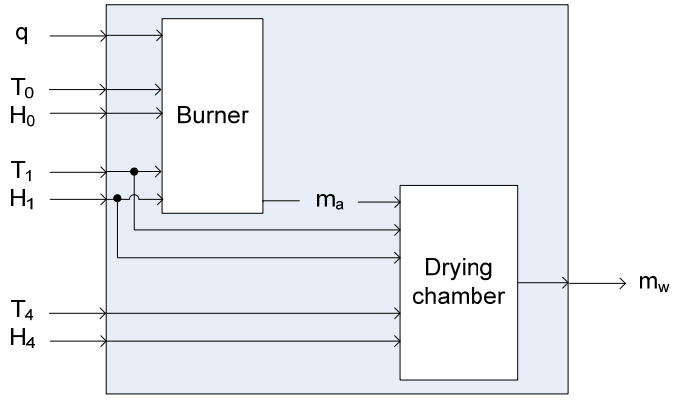

Figure 5. Semi-empirical model of the deep bed dryer.
Structured analytical ANN

3. Results

The empirical model has 2 hidden layers. We used the method on Figure 4 to construct empirical models with different neuron numbers according to Table 2. The results can be observed on Figure 5. The structure of the optimal empirical model and its performance is shown in Table 3.

The semi empirical model always has 3 hidden layers: one for the burner and two for the drying chamber. We used the same method as for the empirical model thus on Figure 4. The results cannot be shown on one diagram as the 3

layers of neurons span a 3-dimensional space rather than a 2-dimensional. But it is possible to show on several diagrams. We need as many diagrams, as many neurons we have in a chosen layer. We choose the burner layer, because it has less possible number of neurons than the others. This way we got the smallest number of diagrams. Figure 6 contains the optimal structure. The structure of the optimal semi empirical model and its performance can be found in Table 3.

Table 2. Optimal models

model	layer	neurons	error
empirical	1st	7	0.862
	2nd	9	
semi empirical	burner	1	2.6
	drying chamber 1st	13	
	drying chamber 2nd	11	

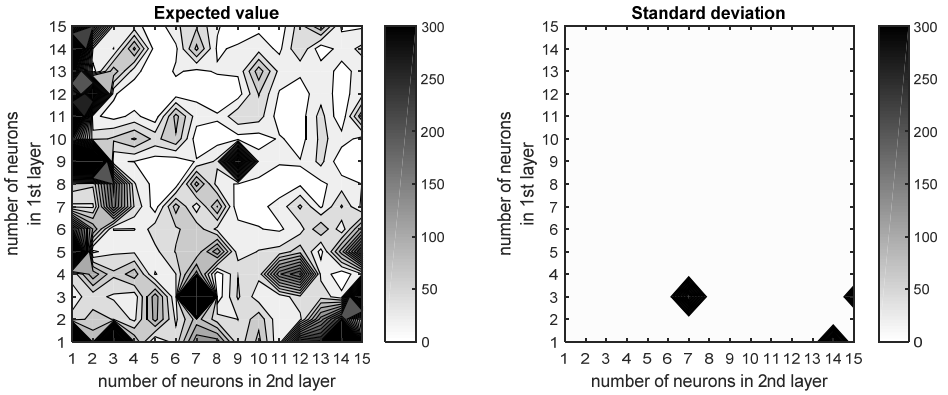

Figure 6. Performance of the empirical model with different neuron numbers.

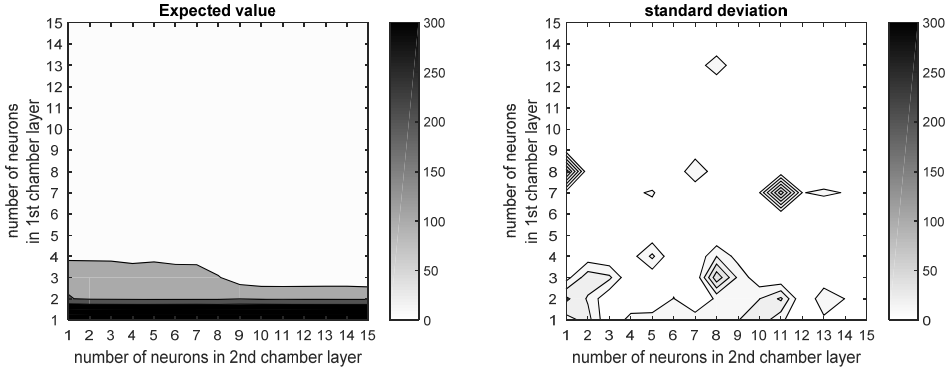

Figure 7. Performance of the semi empirical model with a single neuron in the burner layer.

There are several near optimal structures on figure 6. On the other hand there are structures with significantly higher error what probably make the model unusable. If the burner has one neuron the 1st chamber layer should have at least 3 or 4 neurons. The diagrams with higher neuron numbers for the burner show significantly higher error. Because of the limited space we did not include in this paper all the diagrams but they are very similar to Figure 7 in the aspect that the model with all those neuron numbers has significantly higher error.

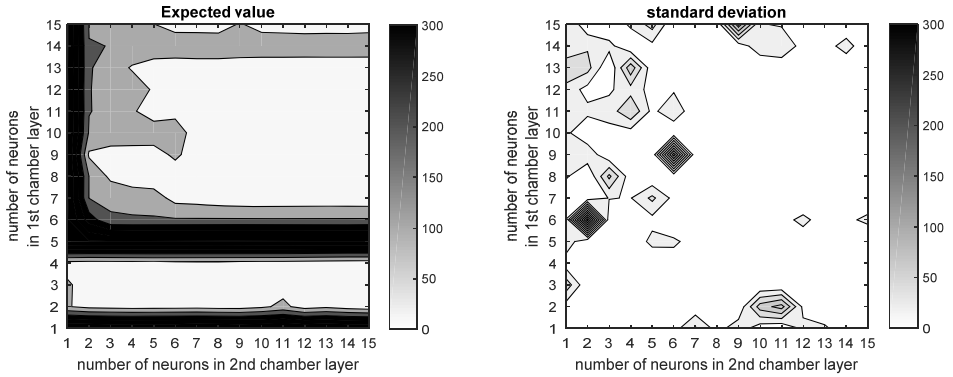

Figure 8. Performance of the semi empirical model with 2 neuron in the burner layer.

Conclusion

The statistical approach can help us to find the optimal structure of the network.

The models performance can be highly influenced by the applied number of the layers, and the number of the neurons in the layers.

There are structures and neuron numbers that will never ever provide us an accurate model. On the other hand, there are structures what provide us accurate model with a high probability.

Semi-empirical models are less sensitive to neuron numbers applied.

References

[1] Bessenyei, K.; Kurják Z.; Deákvári, J.; Beke J. Modelling of tomato pomace drying process with artificial neural network. In Proceedings of 5th European Drying Conference, Paris, France, October 2-5, 2013.

[2] Bessenyei, K.; Kurják Z.; Beke J. Semi empirical models with artificial neural network. In Proceedings of 6th European Drying Conference, Budapest, Hungary, October 21-23, 2015.

Pressure regulation in pneumatic tractor tyres

György PILLINGER, László MÁTHÉ, József DOBOS, Péter KISS
Department of Automotive Technology,
Institute for Process Engineering

Abstract

Work on tyre pressure regulators has hitherto paid little attention to energy consumption. Energy use depends on how frequently and over how wide a range the pressure is changed. Larger tyres also require more energy for inflation. Consequently, care must be taken in choosing the tyre pressure and the route taken, avoiding inappropriate types of road. Since the physical properties of the soil are partially dependent on the weather, current soil condition on terrain routes should be properly considered when setting the tyre pressure.

Keywords

tyre pressure regulator, tyres, tyre load capacity, contact surface, specific ground pressure, tyre pressure, radial, fertility.

1. Introduction

Many agricultural machinery manufacturers now offer tyre pressure regulators for their products. A pressure regulator inflates tyres to pre-set pressures either at the press of a button or automatically, using GPS signals. None of these systems, however, take account of current road conditions, for example, after sustained rain or drought. The best basis for setting tyre pressures is the data provided by the manufacturer. Tyre catalogues carry graphs of tyre load capacity against pressure at various travel speeds, from which the appropriate pressure may be read. At present, the effect of road conditions is considered only in distinguishing between rigid track (travel on a public road) and deforming track (on terrain). On a rigid track, the tyre pressure is set as high as possible so as to reduce rolling resistance and prevent tyre wear. This is comparable to tyre pressure optimisation systems for passenger cars, involving tyre pressure monitors or automatic pressure regulation [1]. On a deforming track, the aim is to reduce the inflation pressure as far as possible, which reduces the specific ground pressure and thus the energy required for travel [3][7]. Furthermore, appropriate tyre pressure improves tractive efficiency [2]. The benefits of the tyre pressure regulator are thus realised in the form of fuel savings. Little is said, however, about the energy consumption of the pressure regulator. Clearly, the higher the frequency and the wider the range of tyre pressure changes, the less energy savings there will be. Furthermore, the

larger the tyre, the more energy is required to inflate it. Since the relation between ground pressure and sinkage is described by a saturation curve, reducing the tyre pressure to its lowest setting is not absolutely necessary. After a certain point, the increase in contact area with decreasing pressure is so small as to achieve no significant improvement in soil compaction and tractive force. Re-inflation of the tyre, however, requires a substantial amount of energy.

Our aim is therefore to minimise the pressure difference in the tyres when travelling on roads and on terrain, by taking account of current soil conditions.

Theoretical energy requirement for change of tyre pressure

We determine the theoretical energy requirement of a 710/75 R42 tyre, assuming constant temperature and tyre volume.

Profile width: $B = 71$ cm

Profile height: $H = 53.3$ cm

Tyre diameter: $D = 213.3$ cm

Tyre air volume:

$$V = \left(\frac{B}{2}\cdot\frac{H}{2}\cdot\pi\right)\cdot(D-H)\cdot\pi = \left(\frac{0.71}{2}\cdot\frac{0.533}{2}\cdot\pi\right)\cdot \cdot(2.133-0.533)\cdot\pi = 1.49\,m^3 \quad (1)$$

Pressure range applicable to tyre (from catalogue): 0.5–1.8 bar

Tyre energy at lowest pressure:

$$E_1 = p_1 \cdot V = 0.5\cdot 10^5 \cdot 1.49 = 74500 J$$

Tyre energy at highest pressure:

$$E_2 = p_2 \cdot V = 1.8\cdot 10^5 \cdot 1.49 = 268200 J$$

Thus, energy required for inflation:

$$\Delta E = E_2 - E_1 = 268\,200 - 74\,500 = 193\,700\,J = 193.7\,kJ$$

This is the energy used for a cycle of one inflation and one deflation. For an axle with two such tyres, the energy required for a cycle involving a change in pressure of 1 bar is 298 kJ. This corresponds to the energy provided by 7 g of diesel fuel. In practice, the energy expended is higher than this theoretical value because it includes losses in the inflation system.

Determination of the load capacity of the tyre

The load capacity of the tyre is determined, where possible, from the manufacturer's catalogue. Otherwise, it may be calculated from a knowledge of

the tyre dimensions and operating circumstances, using the following formula [4].

$$T = \left[C \cdot (B \cdot D) + \alpha \cdot (B \cdot D)^n\right] \cdot C_v \cdot C_p \tag{2}$$

Speed factor:

$$C_v = 1.72 \cdot v^{-0.23} \tag{3}$$

Tyre pressure factor:

$$C_p = L \cdot p^m \tag{4}$$

where:
T – tyre load capacity, [kg]
B – tyre width, [m]
D - tyre diameter, [m]
c_v – speed factor, [-]
c_p – tyre pressure factor, [-]
p – tyre pressure, [bar].

Table 1. Values of variables

Variable	Radial tyre	Diagonal tyre
m	0.46	0.55
L	0.78	0.78
n	2.00	2.00
α	650.00	500.00
C	4500.00	3800.00

Determination of specific ground pressure under tyre
After obtaining the load capacity of the tyre, the next step is to determine the specific ground pressure under the tyre, for which we also use the dimensions and operating parameters of the tyre. The empirical formula used does not apply to deforming soil, but minor sinkage only slightly increases the contact area, and so – if z/D ≤ 0.05 – the following formula may be used to a good approximation [5]:

$$\sigma_R = T^{0.15} \cdot (B \cdot D)^{-0.2} \cdot p^{0.6} \cdot 33.3 \tag{5}$$

In addition to the tyre load capacity and the ground pressure under the tyre, we need the value of a quantity that characterises the current condition of the soil from which we may calculate its bearing capacity. The Saakyan formula,

which relates specific ground pressure to soil condition, may be used to obtain the soil bearing factor.

$$\sigma_R = k \cdot \left(\frac{z}{d_e} \right)^{n_1} \rightarrow k = \sigma_R \cdot \left(\frac{d_e}{z} \right)^{n_1} \tag{6}$$

where
k – soil bearing factor, [Pa]
z – soil deformation, [cm]
d_e – equivalent pressure plate diameter, [cm]
n_1 – soil dependent constant (for loamy sand soil: 0.8) [-].

The equivalent diameter is calculated from the contact area, which is either measured or calculated, the latter involving the empirical relation:

$$A = 2.26 \cdot \left(B \cdot D \right)^{0.5} \cdot \Delta r_R \tag{7}$$

where
Δr_R – tyre deformation, [cm]
A – contact area, [cm^2].

The most convenient method of determining tyre deflection or deformation is direct measurement, allowing contact area to be obtained using Equation (7). Tyre deformation may also be calculated, however, by the empirical [6]:

$$\Delta r_R = T^{0.835} \cdot \left(B \cdot D \right)^{-0.3} \cdot p^{-0.33} \cdot 10^{-2} \tag{8}$$

The equivalent diameter is:

$$d_e = \sqrt{\frac{4 \cdot A}{\pi}} \tag{9}$$

The ratio z/D is the depth to which the wheel has sunk into the soil relative to its diameter. A high z/D value thus means that the wheel has sunk deep into the soil. This implies that, for the same specific ground pressure, wheel sinkage decreases with increasing soil bearing factor. This gives the name of the factor k. Conversely, for the same sinkage, specific ground pressure increases with k, meaning that the soil bears a greater load.

Therefore, the soil bearing factor must be set to the highest possible value by adjusting σ and d_e, or rather by setting tyre pressure and load, because σ and d_e are also functions of tyre pressure. This is possible because the bearing capacity of a soil is not simply an inherent property but a function of the interaction, i.e. the size of the contact area.

These relations allow tyre load capacity to be plotted against tyre pressure:

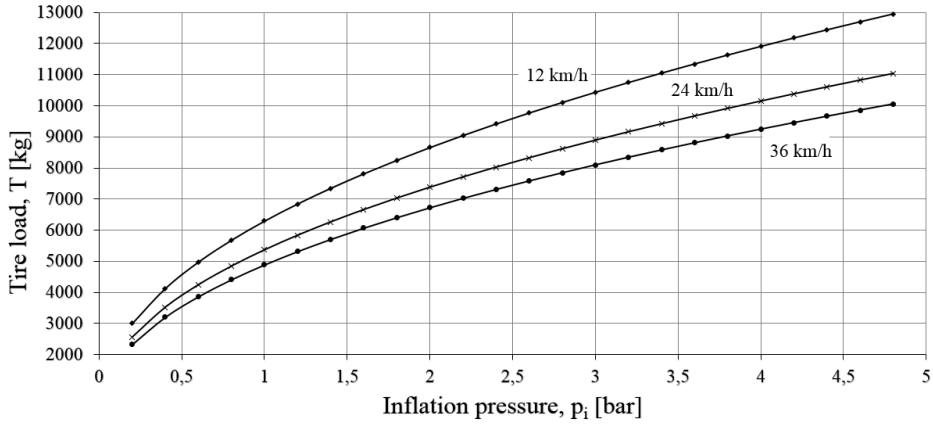

Figure 1. Load capacity of 710/75 R42 tyre at various speeds.

Figure 1 shows the load capacity of a 710/75 R42 tyre against tyre inflation pressure, calculated using Equation (2), at travel speeds of 12, 24 and 36 km/h. The pressure range must lie within the working range of the tyre. There is no sense in investigating outside this range, because at higher or lower pressures, the tyre would fail within a short time. The variation of load capacity is approximately proportional to tyre pressure. Increasing speed severely constraints maximum load. For example, for a pressure of 3 bar, the load capacity at 36 km/h is only 78% of that at 12 km/h.

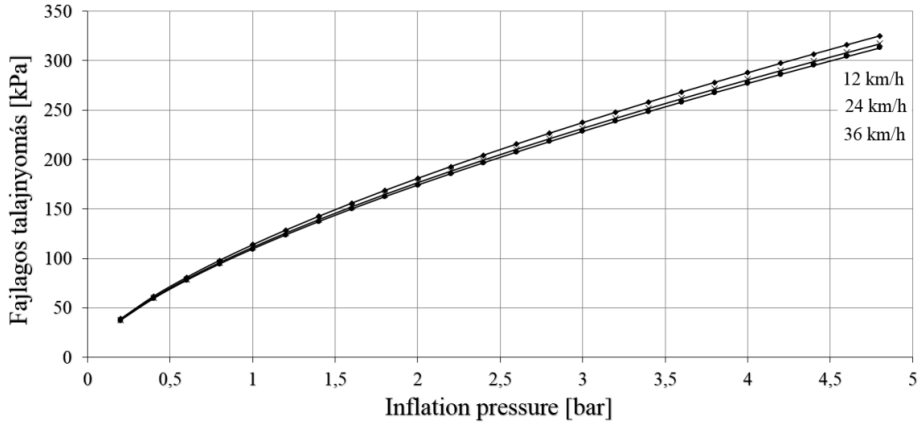

Figure 2. Specific ground pressure at maximum load.

Figure 2 shows the specific ground pressure calculated using Equation (5) at the loads calculated above, again for speeds of 12, 24 and 36 km/h. As for load, the ground pressure curve is linear to a good approximation, but the speed has much less effect. At 3 bar, the difference is approximately 4%. The main effect

is that of change of load, because in Equation (5), the speed has no direct presence. Since field measurements may have errors of more than 5%, this change is difficult to detect.

Figure 3 shows the soil bearing factor against soil deformation, using the specific ground pressure values. The bearing factor clearly varies more steeply in the 0–4.8 cm range than in the 7.8–12 cm range.

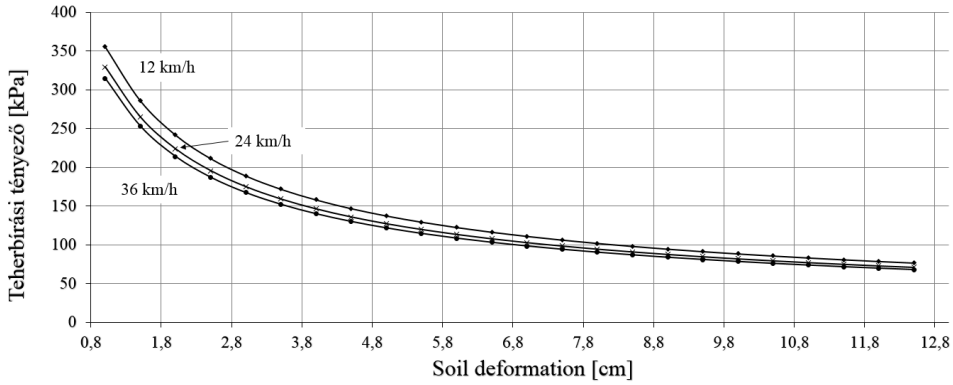

Figure 3. Soil bearing factor as a function of soil deformation for a 710/75 R42 tyre.

Conclusions and proposals

Using known tyre parameters and operational parameters, and for specific speeds, the graph of tyre pressure vs. tyre load may be constructed from Equation (2), and that of tyre pressure vs. specific ground pressure from Equation (5).

1. From these graphs, we can read off the maximum load from a given tyre pressure or the tyre pressure applicable for a given load, at the relevant speed. The graph thus tells us the required change in pressure (Figure 1).
2. Knowing the maximum ground pressure for the soil, we can obtain the corresponding tyre pressure (Figure 2). This also tells us the required pressure change.
3. The soil bearing capacity may be obtained from the rut depth using Figure 3.

With regular data collection, further comparisons and analyses could be made from the bearing factor. Possible examples are the comparison of bearing factor values for different fields, the investigation of sensitivity of bearing factors to changes in moisture content in specific fields, and the determination of the relationship between tyre pressure and bearing factor. Given the wide scatter of soil physical characteristics and the diversity of operational circumstances, individual measurements for each field are required to determine the parameters precisely.

Knowing these, it is possible to ensure that the tyre pressure regulator is always set to the appropriate level. The savings offered by the pressure

regulator, however, can to some extent be wasted by overuse, and so we must also control the frequency and magnitude of changes.

References

[1] A.V. Wadmare, P.S. Pandure (2017): Automatic Tire Pressure Controlling and Self Inflating System: A Review, IOSR Journal of Mechanical and Civil Engineering, pp. 01-05. ISSN: 2320-334X.

[2] B. Kayisoglu, Y. Engin, I. S. Dalmis, B. Akdemir, Y. Bayhan, A. Kullukcu (2014): Developing an Automatic Tire Pressure Control System To Improve the Tractive Efficiency of Tractors, Journal of Agricultural Machinery Science, 10(3), 253-259.

[3] Hajdú J. (2014): Központi guminyomás-szabályozás előnyei az erőgépeken [Advantages of tyre pressure regulation in agricultural tractors]. Mezőgazdasági Technika. http://technika.gmgi.hu/uploads/termek_574/a_kozponti_guminyomas_szabalyozas_elonyei_az_erogepeken_14_07.pdf

[4] Komándi Gy. (1974): A belapulás, a felfekvési méret és teherbíró képesség meghatározása betonpályán, fúvott gumiabroncsoknál [Determination of flattening, contact area and bearing capacity on concrete track with pneumatic tyres]. Járművek, Mezőgazdasági Gépek XXI. évf. 12.sz. 1974. pp. 447-451.

[5] KomándiGy. (1999): Hajtókerék-abroncsok üzemi paramétereinek számítása traktoroknál [Calculation of operational parameters of tractor drive wheel tyres].

[6] Laib L. (2002): Terepen mozgó járművek [Vehicles travelling on terrain]. Szaktudás Kiadó Ház, Budapest.

[7] Varga V. (2017): Gumiabroncs légnyomásának szabályozása mezőgazdasági gépeknél [Regulation of tyre pressures in agricultural machinery]. Agrofórum Online. http://agroforum.hu/archivum/2017-aprilis/gumiabroncs-legnyomasanak-szabalyozasa-mezogazdasagi-gepeknel

Some aspects of torque transmissibility of dry friction clutches (presented at the 19th International and 14th European-African Regional Conference of the ISTVS)

Gábor MAGDICS[1], Péter SZENDRŐ[2], Péter KISS[3]
[1]Department of Product Development, Schaeffler Savaria Ltd.
[2]Department of Machine construction, Institute for Mechanics and Machinery
[3]Department of Automotive Technology, Institute for Process Engineering

Abstract

Dry friction clutches are a key element of today's manual transmission equipped cars. Their widely used methods of dimensioning are often based on experimental values e.g. those regarding the necessary slip safety factor. Also, there are many simplifications used in the formulas describing the torque transmissibility. One of these is that a uniform pressure distribution is supposed to be acting between the friction linings and the cast iron parts of the clutch mechanism and those of the flywheel. This is not the case in most real situations, since frictional heat is forcing these parts to deform. In this paper the effects of thermoelastic deformations of the iron castings on the pressure distribution is discussed, and a measurement is proposed, so that this influence can be included into the formula describing the transmittable torque of a clutch.

Keywords

clutch, pressure distribution, thermoelastic deformation

1. Introduction

Most of today's cars are propelled by internal combustion engines through manual gearbox transmissions. The clutch system is a key element of these powertrains, since its malfunction or design deficits can cause severe problems in many different operating conditions. Very often they have to be developed fulfilling strong compromises, because of controversial goals to be achieved.

First, they have to ensure proper torque transmission at most extreme temperatures, which requires a robust construction. This need is intensified by the increasing torque capacity of the engines, which was multiplied in the recent decades. This was shown by M. Zink et al. [1] on the example of one manufacturer's two-liter Diesel engines of different model years.

However, clutches have to offer the ability to the driver to operate them precisely and comfortably. This results very often in refined mechanical parts

and a complex structural setup. The cabin noise level of the vehicles is reducing constantly, the vibrations acting on the passengers have to be toned down more and more. Since the requirements themselves are continuously getting higher, the difference between them is harder and harder to bridge. This means that, there is a higher clutch preload needed to transmit the increased torque, although the drivers demand systems, that are easier to operate than earlier ones. The situation gets particularly difficult, when a uniform strength of the clutch mechanism is required, because the stresses of the single parts will get more complex too, as the complexity of the system increases. Also, we can have less and less confidence in the experimental formulae, which have been used unchanged for a long time – telling that the basic operating principles of the clutches have not changed through the last half of a century.

More particularly the focus of the present investigation will be on single plate dry friction clutches, since this can be found in the majority of the vehicles. Their construction is to be seen on fig. 2.

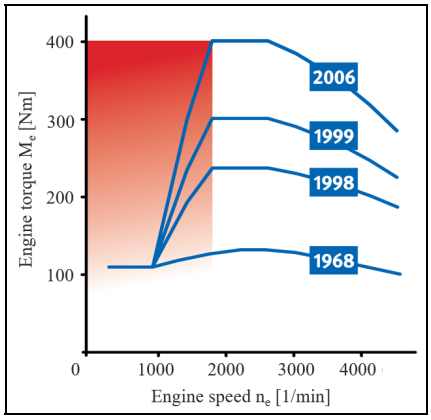

Figure 1. Torque curves of 2000 cm^3 diesel engines

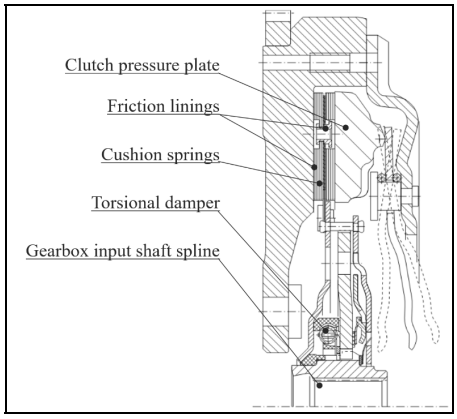

Figure 2. Single plate dry friction clutch

2. Target

With a more precise description of the clutch's torque transmissibility an over- and under dimensioning of the system can be avoided. Therefore, chances of failure can be reduced, and the vehicle ergonomics will improve. The most widespread formulae do not consider some factors, which change, while using the vehicle, resulting in a considerable change in the clutch's torque capacity:

- The friction surfaces of flywheel and pressure plate will get hot due to the heat generated by the clutch slipping. Heat expansion results in internal stresses that deform the flywheel and the pressure plate. The result will be a conical shape of the friction surfaces. Therefore, the surface pressure on these surfaces cannot have a uniform level, it will change as a function of the radius.
- The stiffness of the flexible cushion segments', used to support the back of the friction linings, has an effect on surface pressure too.
- The friction coefficient depends on the relative speed on the friction surfaces. Latter is different on the inner and outer diameter even at constant engine speed, so the friction coefficient is also depending on the radius.

Our target is to define the contexts of clutch operation in such a way, that we become able to consider the above factors. Then, dimensioning of the clutch, can be performed not only specifically to the car type but also to its operating conditions. In the end we are looking for a formula that is suitable to calculate the function shown on fig. 3. On the figure r_m is the equivalent friction radius, M_c is the clutch torque capacity, Δb_0 is the initial conicity [mm], and T the temperature of the friction surface.

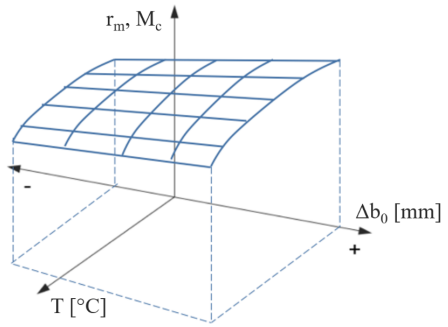

Figure 3. Correlation of temperature, conicity and transmittable torque

3. Background

In 1972, Z. Ternai [3] recommended to perform the dimensioning of passenger car and truck clutches to have a torque capacity of 1,5 – 1,8 times the engine

torque. In 1994 L. Ilosvai suggesteed a lower safety factor of 1,3 – 1,75 [4]. This is already very close to the values that are most commonly used by the majority of today's manufacturers. We may state that, the slip safety factor of clutch mechanisms has been continuously reducing throughout the last decades. This however, has only partially to do with the improvement of dimensioning methods, most of the time it is due to the usage of empirical values, that are available easier and in larger amount – apart from the usage of more advanced materials of course. There are however, large differences between the different applications, be it the engine torque, vehicle mass or usage profile. So it would be subservient to additionally consider the factors shown in chapter 2, in the process of torque capacity dimensioning of clutches.

The commonly used formula to describe torque capacity considers homogeneous surface pressure [5], which is a strongly idealised case:

$$M_c = z r_m F_{CL} \tag{1}$$

Temperature distribution in a slipping clutch was described quite precisely by T. P. Newcomb and M. El-Sherbiny in the '70-s already, both as a function of axial and radial position [6]. Their results were refined by O. I. Abdullah and J. Schlattmann, by considering the grooves on the friction surfaces [7]. Likewise, they performed further calculations, simulating heat fluxes of different intensities [8]. Later they considered the effect of the slipping process' initial temperature, simulating more consecutive load cycles [10].

These researches provide detailed results regarding the resulting temperatures within the clutch. But they do not draw any conclusions on how these influences the torque transmissibility of the clutch. Also, they consider the friction linings either as thermally fully insulating, or they neglect the heat dissipated through the lining rivets and the cushion segments. Pursuing an exact dimensioning this is not acceptable, since the surface area of the rivets can be up to 6% of the overall friction surface size [11].

The contact between friction linings is not endlessly stiff as it is supposed in the above-mentioned papers. The importance of the cushion deflection was shown by S. Sfarni et al. [12], who studied the aging process of the cushion springs and the wear between them and the friction linings. They also neglected the fact that, friction surfaces are not parallel in reality, even though this is another considerable influence to the surface pressure.

4. Material and method

In order to define torque capacity more precisely than what is commonly used, it is essential to know the distribution of surface pressure over the radius, and to consider that, when defining the equivalent friction radius. Therefore, it must be defined, which factors and by what rules do have an impact on surface pressure. While doing this, boundary conditions have to be defined in a way that, the results are relevant within everyday circumstances.

Until the exact function of surface pressure is not known, a linear changing of pressure is assumed to act between the inner and outer diameter of the friction surface. The difference to the currently used model is shown on fig. 4.

In the model shown on fig. 4. a) it is supposed that, the friction surfaces are parallel, and the casting parts of pressure plate and flywheel have an endless torsional stiffness. In this case the clamp load F_{CL1} resulting from the diaphragm spring preload will produce a uniform pressure distribution on the friction surfaces. Supposing conical friction surfaces as shown on fig. 4. b) we get a different pressure distribution, even having the same magnitude of F_{CL2} as in the previous case. Experience shows that, in many cases the outer edges of the friction surfaces move away from each other due to the heat expansion, causing the surface pressure to drop locally, and to increase at the inner diameter, thus reducing the torque capacity of the clutch.

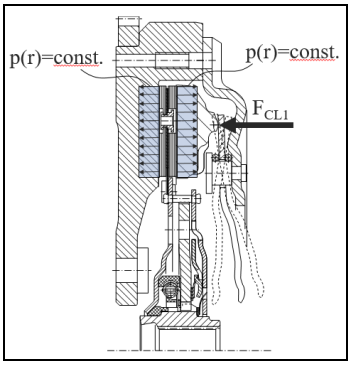

Figure 4. a) Uniform pressure

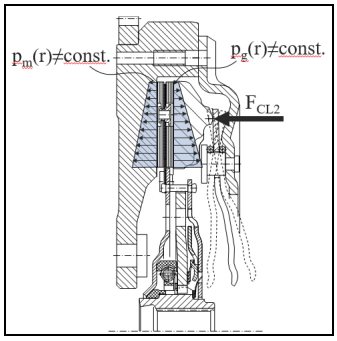

Figure 4. b) Inhomogeneous pressure

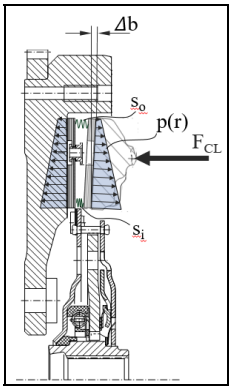

Figure 5. New model

In the model being used to determine the pressure distribution, we suppose the linings to be connected by two springs of known (and measurable) stiffness on

the inner- and outer diameter of the friction surface. Once the stiffness values of these springs are known, the function p(r) can be determined with a given parallelism (Δb_0) and clamp load (F_{CL}). This model is shown on fig. 5.

But this determination of the pressure distribution is still somewhat idealised, since in reality the flexible contact of linings is provided by the cushion segments, which are independent in the tangential direction and support the linings on their backs only at narrow strips, almost linear contact surfaces. The width of these local surfaces depends on the load of the cushion springs. The importance of the inhomogeneous support was described by S. Sfarni et. al. [12].

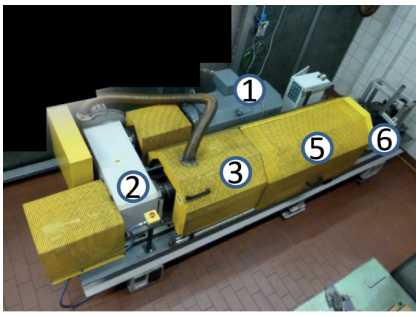

Figure 6. Clutch test rig

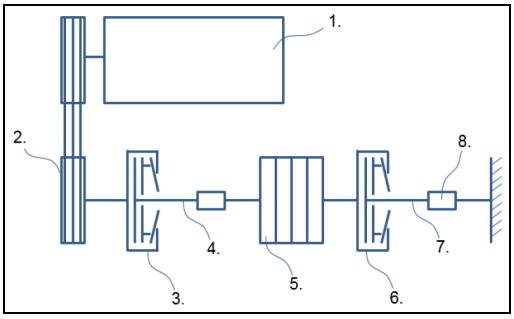

Figure 7. Kinematic scheme of the test rig

Figure 8. Torsional measurement bench

The equipment used for the investigations is one specifically built for measurements on clutches. Its construction is shown on fig. 6. The test bench can accelerate a flywheel of given (and optional) mass and inertia, providing it a known amount of kinetic energy. The tested clutch disc has a common shaft with the flywheels (4.). The clutch mechanism is connected to a fixed shaft (7.). Latter is connected to the fundament of the rig through a torque sensor. The measurement process is the following:

- flywheels of the required inertia (5.) are assembled onto the shaft.
- the internal clutch (3.) is engaged, the tested clutch (6.) is disengaged.
- the electric motor (1.) accelerates the flywheel to the required rotational speed through the (2.) belt drive.
- the internal clutch (3.) is disengaged, thus separating the flywheels from the electric motor.
- the flywheels are decelerated to a standing position by engaging the tested clutch. In the process the torque being transmitted by the clutch is being measured by the torque sensor (8.).

In the last step the kinetic energy stored in the flywheels, will be converted into heat on the friction surfaces of the tested clutch. Thus, the amount of clutch energy and the temperature increase is governed by changing the flywheel inertia.

Since the friction surfaces are the same size on both the engine- and transmission sides of the disc, and the clamp load is symmetrical, the generated friction heat is considered to be equal on both sides. In some applications friction linings with different properties are used on the two sides of the disc, however since this is rather an exceptional practice, no such designs will be investigated.

For the broad usability of the results it is essential for the measurements' boundary conditions and the design parameters of the investigated clutch systems to be chosen very carefully.

The process of the investigation is as follows:

1.) Measurement of the friction coefficient (μ).

The friction coefficient is planned to be measured by two methods:

- A sample of the friction lining is clamped between parallel tool surfaces with a known force, and necessary force to overcome friction is being measured by a simple force meter.
- The assembled clutch disc is clamped between parallel tool surfaces with a known force, and the torque needed to overcome friction is measured on a torsional measurement bench.

Because of the static quality of the measurement, (1) may be used to calculate the friction coefficient. The equipment used for the measurement is shown on fig. 7.

2.) Measurement of spring stiffnesses (s_o, s_i).

The assembled clutch disc is compressed between ring shaped tools on the outer and inner diameter, the travel-load characteristics is registered, and the inner and outer stiffness of the cushion can be evaluated.

3.) Measurement of transmittable torque (M_0).

The transmittable torque of the clutch can be registered with the equipment shown on fig. 7. The clutch is mounted on the flywheel, and the assembly is clamped onto the measurement bench, and the torque needed to turn the friction disc can be measured.

4.) Fitting the flywheel for the current load cycle.

5.) Energy input in five consecutive cycles. Measurement of temperatures, rotational speed, clutch torque during the cycles, and maximal temperature, resulting deformation, and transmissible torque between the cycles (T(t), n(t), T_i, Δb_i, M_i).Measurement of the temperature is planned to be performed on four diameters: as close as possible to the inner-and outer diameters, and at 1/3 and 2/3 of the distance between them. The reason for this is that, presumably the pressure plate deformation cannot be put in correlation with the temperature of only one diameter, but also it depends on the temperature difference between the outer and inner diameters.

The conicity and shape profile of the pressure plate can be measured by a height gage. To do this, the clutch has to be removed from the test bench. The measurement result will be different from the conicity during the flywheel deceleration, which is changing constantly with the temperature, but is impossible to measure directly. The most information that is to get regarding this is the height difference between the inner- and outer diameters that is to be measured indirectly by applying a rod on the pressure plate to make position measurement possible on the outside of the clutch cover.

6.) Measurement of friction coefficient and cushion spring stiffness curves after the fifth load cycle (μ, s_o, s_i).

Values of s_o, s_i cannot be measured between the individual load cycles, since the clutch has to be removed from the bench to perform the measurement on a different machine. Thus the measurements cannot be performed at room temperature and not on that resulting at the end of a particular load cycle. Thus it might be necessary to calculate the values of μ, s_o, s_i for the individual load cycles by interpolation, if the measured values are significantly different from those measured before the last five load cycles. Of course we do not know if these are linearly dependent on the temperature and the transmitted heat. The possible error depends on the difference of the measurement values before and after the five load cycles.

7.) Repeating the series of measurements with the next b and F_{CL} values.

During deceleration of the flywheel the clutch torque is being measured as a function of time. Any change of the torque is supposed to occur due to changes of the surface pressure and thus that of the equivalent friction radius. Since the friction linings are clamped between non-parallel surfaces during the measurement, they experience different amount of wear on different diameters.

This wear is of comparable magnitude to the cast iron part's conicity; thus it has a significant influence on the pressure distribution. Therefore, it is necessary to measure the lining thickness both on the inner and outer diameter.

5. Expected results

Measuring pressure plate conicity, and transmittable torque parallel to the temperature following results can be obtained:

a) effect of the friction surface temperature on the potting of pressure plate,
b) influence of the resulting deformation on the clutch torque,
c) by having these, the function shown on fig. 3. can be obtained,
d) given the friction coefficient and the equivalent friction radius the (supposedly linear) pressure distribution can be calculated,
e) knowing the correlation of the calculated pressure distribution and the inner- and outer cushion stiffness, influence of the latter can be obtained on a) and b).

6. Further tasks

The laws governing the clutch torque in a specific state can be further developed, if the change of friction coefficient over the radius is considered. To decide the error caused by neglecting this, measurement of different friction materials at different speeds is necessary.

The model shown on fig. 5. cannot consider that the potting of the flywheel and that of the pressure plate might be different. The chance of this however is significant, since the flywheel usually has a higher mass (and a higher stiffness), than the pressure plate. Supposed that the induced heat is distributed equally between the two friction surfaces, we can expect to have higher resulting temperatures and deformation on the pressure plate. Thus a difference in pressure distribution of the both sides can be expected too, that must be validated by further measurements.

7. Summary

These days most of our motorized vehicles are propelled by internal combustion engines, through manual transmissions. A key element of these is the clutch that can cause problems in different driving conditions in case of its failure, or any design related defects. There are many controversial aspects that clutch designers have to deal with. Clutches must have a robust construction in order to provide the sufficient torque capacity under the most extreme temperatures. The continuous increase of engine torques over the last decades increased this challenge even further. At the same time they have to be easy to operate and provide comfortable characteristics, as well as a good NVH performance. Not only dimensioning to uniform strength, but simply to find the necessary compromises is getting harder and harder due to the above boundary conditions. The loads acting on the parts and the resulting stresses get more and more complex, so we cannot settle for the accuracy provided by many experience-based methods and formulae any more – even though the basic working

principle of the clutches remained unchanged in the last half of a century. An under dimensioning of the clutch mechanism causes mechanical failure, their over dimensioning leads to insufficient ergonomics and higher costs, thus both of them must be avoided, if possible. To enable the design of clutches fitting the exact application, more detailed knowledge is needed with regard to the transmittable torque of a particular clutch under given circumstances. A more detailed view of the correlations between the temperature-, pressure distribution on the friction surfaces and the torque transmissibility of the clutch, will enable a more precise dimensioning. Result is a uniform lifetime of the clutch parts as well as less cases of over dimensioning, and thus better ergonomics. With the presented series of measurements this correlation can be described. While applying known amount of frictional heat on the clutch, we measure the temperature at a given distance behind the friction surfaces, the deformation of the friction surfaces and the transmitted torque. Knowing these the pressure distribution can be defined as a function of the radial position. With this the transmittable torque of a given clutch can be calculated as a function of the temperature and the conicity of the friction surfaces.

8. List of notations

Δb_0	initial conicity of the pressure plate friction surface	[mm]
Δbi	conicity of the pressure plate at the end of a particular load cycle i	[mm]
μ	friction coefficient acting between lining and pressure plate	[-]
F_{CL}	clamp load (force compressing the friction surfaces)	[N]
M_c	clutch torque (transmitted torque)	[Nm]
M_e	engine torque	[Nm]
Mi	clutch torque after a particular load cycle i	[Nm]
M_0	initial value of the clutch torque (at the beginning of a particular measurement)	[Nm]
n_e	engine speed	[1/min]
n(t)	clutch rotation speed as a function of time	[1/min]
p(r)	radius dependent surface pressure on the friction lining	[MPa]
r_m	mean friction radius	[mm]
s_i	stiffness of the imaginary inner spring between the two sides of the friction linings	[N/mm]
s_o	stiffness of the imaginary outer spring between the two sides of the friction linings	[N/mm]
Ti	temperature of the friction surface at the end of a particular load cycle i	[°C]
T(t)	temperature of the friction surface as a function of time	[°C]

References

[1] M. Zink, M. Hausner, R. Welter, R. Shead: Clutch and release system, 8. LuK Symposium 2006, LuK GmbH & Co. KG 2006

[2] LuK Clutch Course – An introduction to clutch technology for passenger cars, Schaeffler Automotive Aftermarket GmbH & Co. KG, 2012, 999 6000 960 2385/1.0/5.2012/BB-GB
[3] Z. Ternai: Dimensioning of motor vehicle structures, Technical Publisher, Budapest, 1972
[4] L. Ilosvai: Dimensioning of motor vehicle structures, Technical University Publisher, Budapest, 1994
[5] F. Vasca, L. Iannelli, A. Senatore, G. Reale: Torque Transmissibility Assessment for Automotive Dry-Clutch Engagement, IEEE/ASME Transactions On Mechatronics, Vol. 16, No. 3, 2011
[6] M. El-Sherbiny, T. P. Newcomb: Temperature distributions in automotive dry clutches, Proceedings Instn Mech Engrs Vol. 190 34 – 76, IMechE 1976
[7] Oday I. Abdullah, J. Schlattmann: Finite Element Analysis for Grooved Dry Friction Clutch, Advances in Mechanical Engineering and its Applications (AMEA) Vol. 2., No. 1., 2012, ISSN 2167-6380
[8] O. I. Abdullah, J. Schlattmann: Finite Element Analysis of Temperature Field in Automotive Dry Friction Clutch, Tribology in Industry Vol. 34, No. 4 (2012) 206-216
[9] Oday I. Abdullah, J. Schlattmann: Contact analysis of a dry friction clutch system, ISRN Mechanical Engineering, Volume 2013 Article ID 495918
[10] Oday I. Abdullah, J. Schlattmann: Effect of Band Contact on the Temperature distribution for dry friction clutch, World Academy of Science, Engineering and Technology Vol:6 2012-09-29
[11] Z. Terplán, G. Nagy, I. Herczeg: Mechanical clutches, Technical Publisher, Budapest, 1966
[12] Samir Sfarni, Emmanuel Bellenger, Jerome Fortin, Matthieu Malley: Numerical and experimental study of automotive riveted clutch discs with contact pressure analysis for the prediction of facing wear, Finite Elements in Analysis and Design 47 (2011) 129–141

Survey: Effect of bulk density and moisture content of soil on the penetration resistance and penetration depth

Nihal D. SALMAN, Péter KISS
Department of Automotive Technology,
Institute for Process Engineering

Abstract

This paper presents a review about the effecting of mechanical properties of soil on the penetration depth (plate-sinkage test) and penetration resistance (Penetrometer cone index CI). Relationships between cone penetration resistance, bulk density, and soil moisture discussed. Soil penetration resistance rises with increasing density and drops with increasing soil moisture content. If bulk density remains constant, penetration resistance increases with depth. The stress from applied load (plate test) increase with an increase in dry bulk density and decrease with the increase in the moisture content.

Keywords

Sinkage, penetration, soil bulk density, moisture content

1. Introduction

The mechanical behaviour of soil under the external loading affected by many factors such as soil type, moisture content, bulk density, loading type and loading rate. (Mouazen, Ramon and Baerdemaeker, 2002). Some of the physical and mechanical properties of soil are subject to frictions, deformations, and combined action of various stresses, are less precisely defined (Sitkei *et al.*, 2018). The bulk density is generally pointed as the most beneficial parameter of soil structure. It is used as a measure of soil compaction or looseness since it is related to total soil porosity. The bulk density of the soil demonstrate the relationship between its mass and the volume it occupies (Hernanz *et al.*, 2000). Bulk density measurements extensively studied in agricultural research to evaluate soil compaction by vehicular traffic and to evaluate the soil physical condition observed with different tillage systems. Soil moisture content is the most critical factor in the compaction process and soil compatibility (Mosaddeghi *et al.*, 2000).

Soil response to mechanical forces may include compaction, shear, plastic flow and tension failure (Bailey, Johnson and Schafer, 1986). Equipment type, load per unit area (pressure on soil at the tire-soil interface), soil type, soil water content, number of passes influence the depth to which soil density and penetration

resistance where raise (Unger, 1996). Penetration tests applied for obtaining information on in situ soil strength. The cone penetrometer used to predict the tractive capability of an off-road vehicle also used to determine the effect of wheel size and vehicle weight on soil compaction (Ayers and Perumpral, 1982). The penetrometer is the apparatus that allows the value of soil penetration resistance or cone index to be obtained. This is the force per unit of surface required to insert a cone base to a given depth in the soil (Hernanz *et al.*, 2000). The soil penetration resistance increases with increasing density and decreases with increasing soil moisture content. If bulk density remains constant, penetration resistance increases with depth, since the value of the load supported by the soil increases (Elbanna and Witney, 1987). Also, for field soils, applied load cause loading (stress) and compaction. The relationship between applied load on a soil, volumetric water content and initial dry bulk density can be obtained by using the plate sinkage test with a mechanism for monitoring the sinkage. (Alexandrou and Earl, 1998). This work includes a review of some literature to demonstrate the effect of bulk density and water content on the penetration resistance and sinkage.

2. Penetration resistance

(Pillinger *et al.*, 2018) studied relation between the moisture content, soil density and the cone penetration (Cone Index – CI) and proposed empirical approach to finding the bulk density directly from the reading of CI. Classical bulk density determination methods require sampling of the soil, which result in interfering and changing the original soil states. Soil bin (1.8, 1.0 and 0.7 m) filled with sandy adobe stubble, husked stubble and cultivated stubble used through the experiment. The results (Figure 1) of penetration experiments for soil with different moisture content and different densities showed the cone resistance was linearly raising until 10 cm depth, then stabilised at a maximal value. Besides, the penetration depth increased as the moisture content raised.

(Gao *et al.*, 2016) Proved that a relatively simple model for penetrometer resistance could be used to characterise the effects of soil drying, bulk density, and depth. The experiments placed in a field with total area 195 m × 194 m, divided into 27 plots. The no-tillage (NT) and ridge tillage (RT) with continuous corn systems were used to investigate the changes of penetrometer resistance. The depth of soil for experiments ranged 0-50 cm and divided to four layers 0–5, 5–10, 10–20, and 20–50 cm. Figure 2 reveals how the depth effect on soil bulk density under NT and RT. Where the bulk density for top 50 cm soil reached 1.3 to 1.57 g.cm-3 and 1.19 to 1.52 g cm-3 for NT and RT. Soil bulk density of NT practice was remarkably higher than that of RT with a layer of 0–20. This means lower soil bulk density under conventional tillage (RT) than that under no-tillage. The soil compaction caused a reduction of large pores and an increase of small pores. So, for compact soil observed lower water contents with higher matric potentials and higher water contents at lower matric potential. (Antille *et al.*, 2013) This study explored the changes in soil bulk density from soil

displacement data created by combine harvester tires (680/85R32, 800/65R32, and 900/60R32) with a vertical load (10.5 ton) and inflation pressures (0.19 to 0.25 MPa). The soil utilised was a Cottenham series sandy loam (66% sand, 17% silt, and 17% clay) with two different soil bulk densities (γ): low (γ = 1.20 g cm^{-3}) and high (γ =1.60 g cm^{-3}).

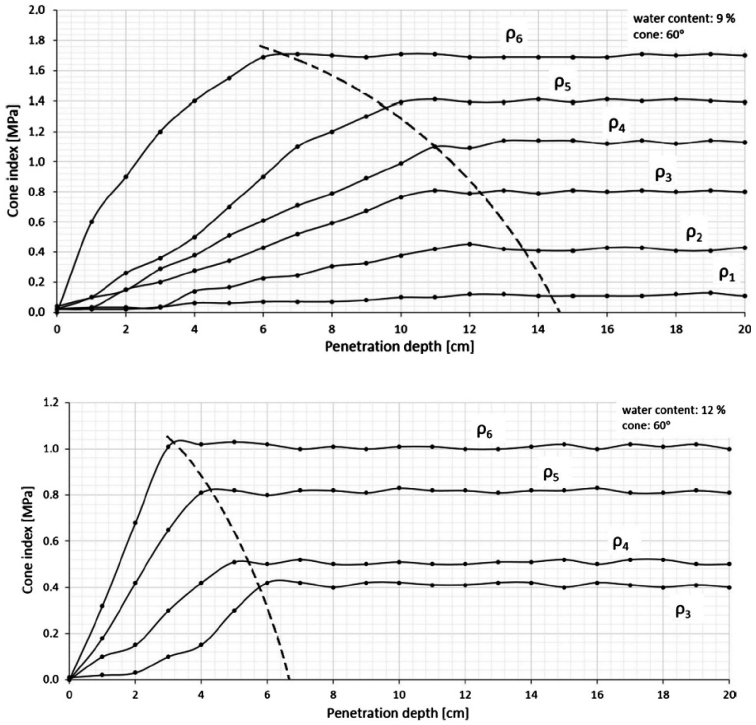

Figure 1. Relationship of CI and penetration depth with different densities and water content: 9 % and 12 %(Pillinger *et al.*, 2018)

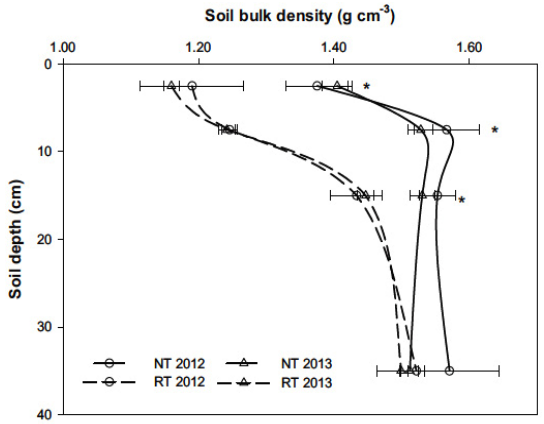

Figure 2. Effect of the depth (0–50 cm) soil profile on the soil bulk density between no-tillage (NT) and ridge tillage(RT) for 2012 and 2013 (Gao *et al.*, 2016)

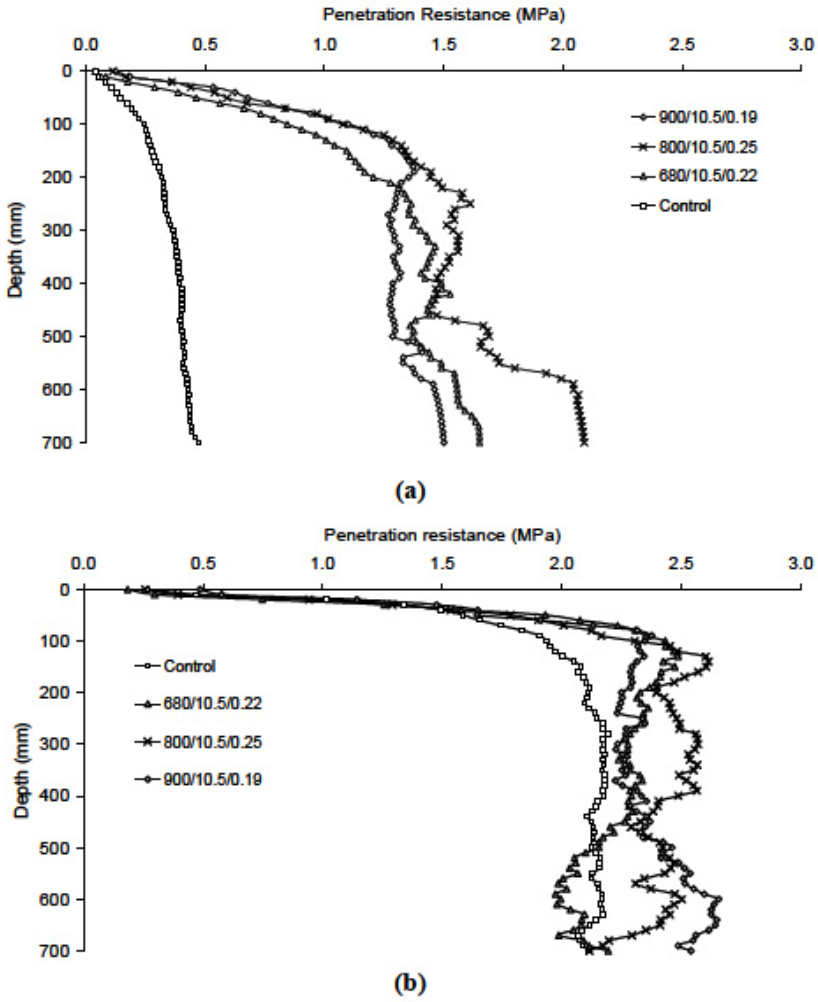

Figure 3. The penetration resistance of soil with respect to depth
(a) low (γ = 1.20 g cm-3) and (b) high (γ = 1.60 g cm-3) initial bulk density soils
(Antille *et al.*, 2013)

The soil was ensured at 10% (w w^{-1}) moisture content throughout the tests. The drop cone penetrometer is used to give a quick indication of the potential soil compaction because of machinery traffic. Linear relationships were determined between the initial soil bulk density and the resultant increase in soil bulk density calculated

from the vertical soil displacement data. The initial soil bulk density was the main feature influencing the range of vertical soil displacement, increase in soil bulk density, increase in soil penetration resistance. For all the tire configurations, the total increases in soil bulk density calculated from soil displacement data were 26% for the low (γ = 1.20 g cm^{-3}), 17.5% for the

medium (γ = 1.40 g cm^{-3}), and 4% for the high (γ =1.60 g cm^{-3}) initial bulk density soil conditions. Additionally, increased tire size and low inflation pressure reduced soil displacement and the resultant increase in soil bulk density (Figure 3 a and b). The usefulness of increasing tire size and lowering inflation pressure discussed as a result obtained from the cone penetrometer resistance data. The tire with the highest inflation pressure (0.25 MPa) produced a significantly higher increase in soil cone index (0 to 700 mm depth range) compared with the tires with lower inflation pressures (0.19 and 0.22 MPa). In the above relationships for a range of initial soil conditions, this appears to be a promising and practical way to predict potential damage to the soil before harvesting operations are conducted.

3. Penetration depth

(Jang, Lee and Lee, 2016) Modelled the plate-sinkage test based on Discrete Element Method (DEM) and produced the soil characteristic properties of the virtual soils to reveal effects of the DEM parameters on the vertical bearing capacity of the soil. Nominal model results compared with experimental data of actual dry sand. The effects of the particle density on soil conditions besides the bulk density were studied. A parametric study with different particle densities (1000 $kg \cdot m^{-3}$, 2000 $kg \cdot m^{-3}$, 3300 $kg \cdot m^{-3}$, 4000 $kg \cdot m^{-3}$ and 5000 $kg \cdot m^{-3}$) conducted for each model by simulating ten individual cases. Figure 4(a) reveals that normal stresses (σ) (plate size is 100 mm) with different particle densities change with sinkage (z). Normal stress clearly decreases with a small particle density and showing a linear proportion between normal stress and particle density. Figure 4(b) and (c) shows the changes in the soil characteristic properties due to the variation of particle density.

The cohesion modulus k_c and the frictional modulus k_φ are affected by the particle density because the vertical bearing capacity is boosted by the increase in soil density. In addition, the exponent of soil deformation (n) approaching (1) indicates that the curves of normal stress vs sinkage appear to be linearly related with high particle densities like those of compact dry sand.

(Malý *et al.*, 2015) Presented the relationship between pressure and depth for compressed and non-pressed soil under laboratory conditions by using Bevameter test. The soil was moistened to the desired moisture before the experiment and then placed in a container with dimensions 640 × 440 × 400 mm up to a height of 370 mm. Compression of the tested soil was carried out using a pressure of 100 kPa (1 bar) for 3 seconds. Tables 1 and 2 reveal the soil samples used for the laboratory measurements, Different plate diameter used (25, 38, 50, 70 mm).

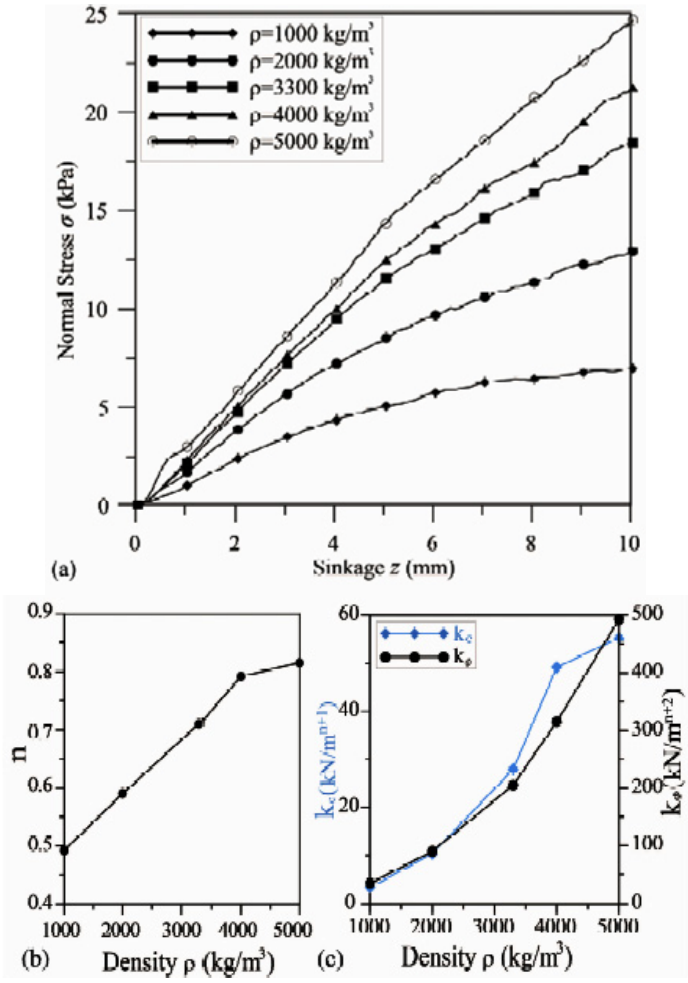

Figure 4. (a) Pressure (Normal stresses) under the 100 mm plate; (b) the soil deformation exponents; (c) frictional moduli and the cohesive moduli for different particle densities (Jang, Lee and Lee, 2016)

Table 1. The soil samples used

Type of soil	Granularity	Moisture content
Non- pressed and pressed	Z1	4.81 %
		16.03 %
	Z2	5.7 %
		17.03 %
Pressed	Z1	4.81 %
		16.03 %
	Z2	5.7 %
		17.03 %

Table 2. The granularity of soil samples (Malý *et al.*, 2015)

Symbol of soil sample	Content of soil particules according to size in percentage				
	>0.25 mm	0.25-0.05 mm	0.05-0.01 mm	0.01-0.001 mm	<0.001 mm
Z1	6.16	5.57	53.8	17.92	16.55
Z2	40.49	13.52	25.67	10.61	9.71

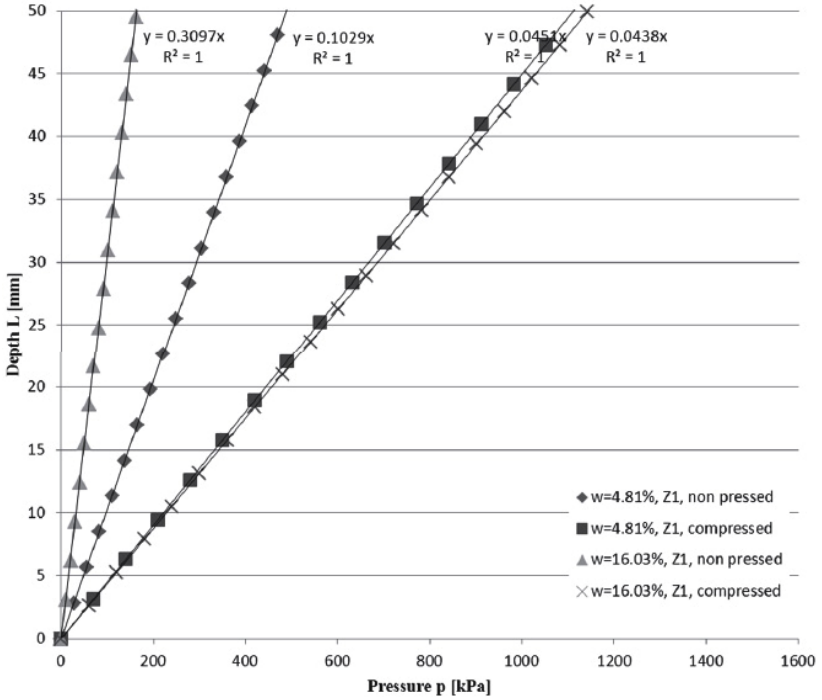

Figure 5. The relationship between pressure and depth after regression analyse for various soil granularity Z1 (non-pressed and compressed soil) and moisture (Malý *et al.*, 2015)

Figure 5 graphically explains the relationship between pressure and depth after regression analyses for various soil moisture and granularity Z1 of the non-pressed and the compressed soil. There is a high difference for the same soil moisture and granularity in the case of non-pressed and compressed soil. Similar differences are shown in Figure 6, however for the granularity Z2 and approximately the same soil moisture.

Based on of obtained results the dry soil with a moisture level about 5% does not change its mechanical properties expressively, not even after compression and regardless of granularity. However, at a level of soil moisture of 16–17% the change in mechanical soil properties after compression is highest of all.

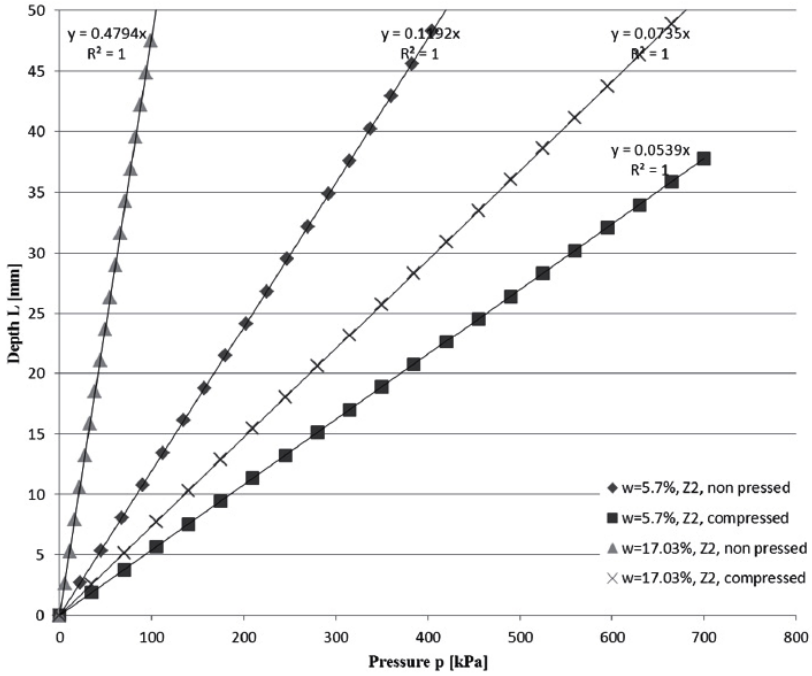

Figure 6. The relationship between pressure and depth after regression analyte for soil (non-pressed and compressed soil)with granularity Z2 and various soil moisture (Malý *et al.*, 2015)

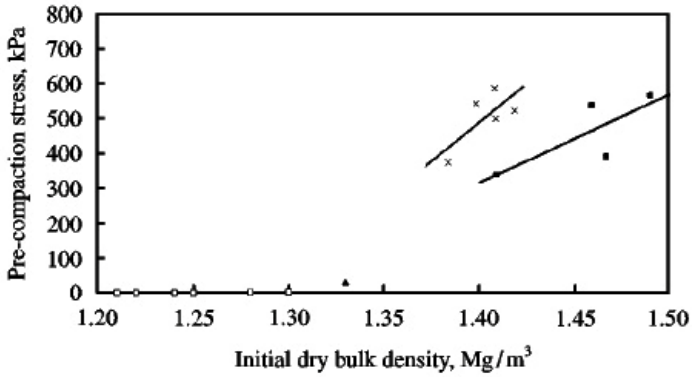

Figure 7. Pre-compaction stress relation with initial dry bulk density for sandy loam soil in the field. (× volumetric water content 10-15%, ■ volumetric water content 16- 17%, ▲ volumetric water content 21%, Δ zero pre-compacted soil, ─ regression lines (Alexandrou and Earl, 1998)

(Alexandrou and Earl, 1998) studied Pre-compaction stress, by limiting stress to below that which determined the pre-compaction, the risk of further collapse to the soil through additional compaction can be decreased. The relationship between pre-compaction stress determined by using the plate

sinkage test, volumetric water content and initial dry bulk density is examined. Two types of soil tested sandy loam and clay soil. For the clay and sandy loam soil, the range of dry bulk density from 0.99 to 1.36 Mg/m^3 and 1.30 to 1.50 Mg/m^3, with volumetric water content from 25.1 to 51.6 and 10.2 to 21.2%, respectively. A total of 16 plate sinkage tests were carried out on each soil. Pre-compaction stress for sandy loam soil (Figure 7) was found to increase with increasing dry bulk density and decreasing volumetric water content which is characteristic of the domination of frictional resistance within this soil. For clay soil (Figure 8) increases in pre-compaction stress were found closely correlated with decreases in volumetric water content which influences the cohesive nature of this soil type but mostly independent of dry bulk density.

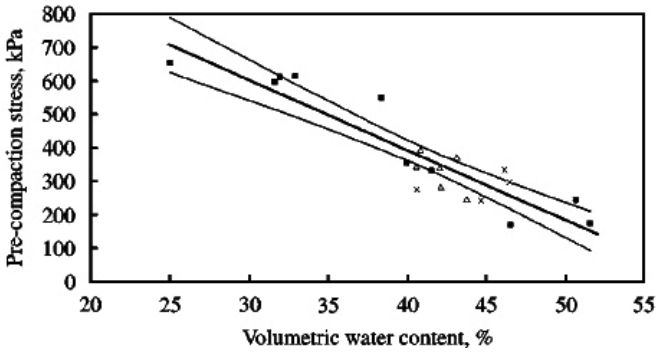

Figure 8. Pre-compaction stress relative with volumetric water content for clay soil in the field for (■ dry bulk density 0.99-1.12 Mg/m^3, × dry bulk density 1.23-1.28 Mg/m^3, ▲ dry bulk density 1.30-1.36 Mg/m^3, ── regression lines) (Alexandrou and Earl, 1998)

Conclusion

The main conclusions got from this survey are the soil bulk density is the factor influencing the extent of vertical soil displacement. Soil density, moisture content, and soil type effect on the penetration resistance of Cone Index (CI). The resistance of penetrometer increases with soil depth even when soil water content and density stay constant. The strength of the soil is dependent on soil moisture where the rise in moisture content in unsaturated soils cause a decrease in soil strength progressively. Low bulk density soils have naturally low strength to bear the load, where greater deformation and compaction occur compared with high bulk density soils. The stress of clay soil decreases as water content increases, the bonds between the soil particles are a weakness. That means the cohesive forces reduce when more water is absorbed. Inversely, for sandy soil, the stress goes up as the bulk density increase, as the frictional resistance increase.

Acknowledgement

This work was supported by the Stipendium Hungaricum Programme and by the Mechanical Engineering Doctoral School, Szent István University, Gödöllő, Hungary.

References

[1] Alexandrou, A. and Earl, R. (1998) 'The Relationship among the Pre-compaction Stress , Volumetric Water Content and Initial Dry Bulk Density of Soil', *Journal of Agricultural and Engineering Research*, 71(1), pp. 75–80.
[2] Antille, D. L. *et al.* (2013) 'Soil displacement and soil bulk density changes as affected by tire size', *American Society of Agricultural and Biological Engineers*, 56(5), pp. 1683–1693.
[3] Ayers, D. and Perumpral, J. V (1982) 'Moisture and Density Effect on Cone Index', *American Society of Agricultural Engineers*, pp. 1169–1172.
[4] Bailey, A. C., Johnson, C. E. and Schafer, R. L. (1986) 'A model for agricultural soil compaction', *Journal of Agricultural Engineering Research*, 33(4), pp. 257–262.
[5] Elbanna, E. B. and Witney, B. D. (1987) 'Cone penetration resistance equation as a function of the clay ratio, soil moisture content and specific weight', *Journal of Terramechanics*, 24(1), pp. 41–56.
[6] Gao, W. *et al.* (2016) 'Soil & Tillage Research A simple model to predict soil penetrometer resistance as a function of density , drying and depth in the field', *Soil & Tillage Research*. Elsevier B.V., 155, pp. 190–198.
[7] Hernanz, J. L. *et al.* (2000) 'An empirical model to predict soil bulk density profiles in field conditions using penetration resistance , moisture content and soil depth', *Journal of Terramechanics*, 37, pp. 167–184.
[8] Jang, G., Lee, S. and Lee, K. (2016) 'Discrete element method for the characterization of soil properties in', *Journal of Mechanical Science and Technology*, 30(6), pp. 2743–2751.
[9] Malý, V. *et al.* (2015) 'Laboratory test of the soil compaction', *Acta Universitatis Agriculturae*, 63(1).
[10] Mosaddeghi, M. R. *et al.* (2000) 'Soil compactibility as affected by soil moisture content and farmyard manure in central Iran', *Soil & Tillage Research*, 55, pp. 87–97.
[11] Mouazen, A. M., Ramon, H. and Baerdemaeker, J. De (2002) 'Effects of Bulk Density and Moisture Content on Selected Mechanical Properties of Sandy Loam Soil', *Biosystems Engineering*, 83(2), pp. 217–224.
[12] Pillinger, G. *et al.* (2018) 'Determination of soil density by cone index data', *Journal of Terramechanics*, 77, pp. 69–74.
[13] Sitkei, G. *et al.* (2018) 'Methods for generalization of experimental results in terramechanics', *Journal of Terramechanics*. ISTVS.
[14] Unger, P. W. (1996) 'Soil bulk density , penetration resistance , and hydraulic conductivity under controlled traffic conditions '', *Soil & Tillage Research*, 37, pp. 67–75.

Institute for Mechanics and Machinery

Professor Dr. István SZABÓ,
Director of the Institute

Dear Reader,

The Institute for Mechanics and Machinery (IMM) is one of the key units of the Faculty of Mechanical engineering in Szent István University. Its focus area represents a wide range of scientific interests from fundamental engineering disciplines to the more practical applications in machinery design and technology development. As of today the Institute consists of 3 departments:

- Department of Mechanics
- Department of Machine construction
- Department of Agricultural and food Industrial Machines

Services provided by IMM is supported by two further so called "external departments": Department of Biotechnics hosted by Oncotherm Ltd. and Department of Farm Machinery set up by Hungarian National Institute of Agricultural Engineering. The Institute is also housing the Computer Aided Engineering Center, a research and training unit dedicated to IT applications used in engineering procedures. This orientation gives emphases to the use of IT technologies in all areas of engineering activities, but lately it is extremely visible in the field of agriculture and its related fields.

Also, a University-Industry Cooperation Center (FIEK) is connected to the Institute with rapidly developing research infrastructure in the area of informatics and agriculture. This new unit is a key player in providing industry-generated research and establishing direct link between our University and the interested companies

Selected papers published in the following chapter of this journal may give the cross section of the work done by our staff during 2018. In case you may have questions regarding our work please feel free to visit our website at www. gepeszmernok.hu.

Agroinformatics researches at the Institute of Mechanics and Machinery, SZIU

István SZABÓ[1], László BENSE[2]
[1]Department of Machine construction,
Institute for Mechanics and Machinery
[2]Department of Agricultural and food Industrial Machines,
Institute for Mechanics and Machinery

Abstract

Agroinformatics is a rapidly developing field of agriculture focusing on large scale data acquisition and analyses. Communication platforms are already established, however databased decision-making systems are with limited capacities only. A large-scale project aiming at developing new IT applications for agricultural machinery has been initiated at SZIU. In this article preliminary research results and capacity building activities are demonstrated.

Keywords

agroinformatics, ISOBUS, digital production system, sensors, AgIT-FIEK

1. Introduction

Agroinformatics is undoubtedly the most intensively developing sector of agriculture. The goal for which improvements are carried out is to create a single digital system that monitors all aspects of production. However, designing the direction of development is not in a centralized way with systemic thinking, but is organized spontaneously from the bottom, determined by free market processes. Operators involved in development:

- Machine manufacturers and machine distributors also providing repair service. Powered by advanced diagnostics, power machines not only make fault detection easier, but also make their maintenance and repair workable by their data service.
- IT providers are finding a new, fast-growing market for their products. From telephone applications to complete corporate management systems, a wide range of products are available.
- It may become easier for the government or managing authority to verify the legality of granting and use of agricultural subsidies through data sharing.
- Farmers, who would benefit most from the realisation of a well-functioning, easy-to-use, automatic data-recording system, are looking at developments with a certain distance because of the issue of data

security. This situation is well characterized by the fact that customers have activated this service only for 28% of remote monitored power machines*.

The Institute of Mechanics and Machinery of Szent István University undertakes to attempt to influence development trends with basic research by setting up a Higher Education and Industrial Cooperation Centre, exploiting the potential of the *FIEK_16-1-2016-0008* research project and by using applied research to help solve existing system compatibility problems, to build and to operate the laboratory building, Gödöllő Agroinformatics Centre, used as a basis for research. The most important elements of the development program are presented below.

2. Digital Production System (DPS)

Plant cultivation technology can basically be considered developed. The procedure accepted today is an information-based feedback system that operates on the basis of the intuitions of agricultural professionals. According to the principles of the Digital Agri-Strategy, without the creation of at least a partially automated Digital Production System (DPS) based on digital data transmission and processing, mechanized agricultural production cannot be economically continued. DPS does not mean the digitalization of the technology description, but rather the search for combinations of test parameters that can be easily measured and replace lengthy laboratory tests that serve as a basis for intervention decisions. The more data we collect from the tested area with sensors placed on machines, sensors installed in the production area, or remote sensing, and the longer we collect the data, the more accurate and faster decision preparation we can offer for farmers. There are three research teams at the Institute of Mechanics and Machinery working on the task. Data collection is carried out by the sensor technology research team, data processing is assisted by the Big Data research team. The DPS work team creates a system description and an algorithm and designs compatible modules for managing inputs and outputs of production. This activity can serve as the basis for programming. Modelling should be done separately for each field (crop site) because of crop rotation and for each crop due to the applied technology. As a result of the part of the task, the following findings have emerged:

1. A 4D model including space and time coordinates to describe DPS system. In the model, a well-defined central event space is the real process of plant growth. The process does not begin with sowing, but with the selection of the biological basis and the provision of appropriate conditions (eg. soil preparation). Plant growth lasts from sowing to harvesting, which can be continuously registered and compared to the production potential. The space of probable events (eg. precipitation, temperature) plays an important role.

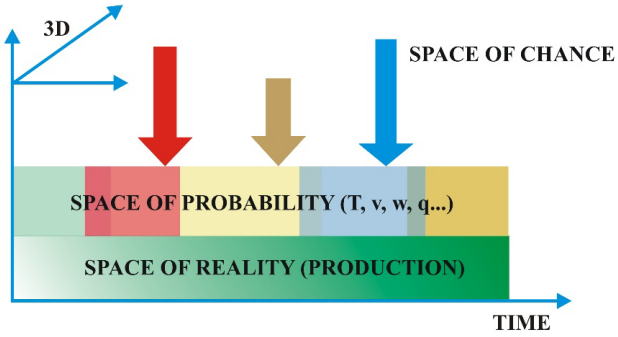

Figure 1. Precision model of cultivation technology

Their value can be estimated with time series statistical analysis. There are production factors that occur randomly (eg. frost, hail, storm, insect invasion, non-identifiable diseases). We follow a model strategy that can be adopted to minimize the impact of these, and to reduce the losses by taking advantage of healing skills. However, the possible outcome of the model is the decision that it is not worth making further investments in the interest of this year's production, but the establishment of the following production year should be concentrated on.

2. Soil, plant, weather and vegetation index database collected in two different regions, on crop sites with different territorial and climatic features. SZIU experts cooperated with Asseco PLC. during the examination of the sample areas. Collaboration allows nutrient utilization decision support software developed by Asseco to be in harmony with SZIU DPS model. In order to ensure the accuracy of the model, data must be collected annually in the designated areas during the continuation of the project. The sensors to be developed later in the project will also be advisable to be tested in the same areas. The data collected from the same area employing multiple methods also helps validate the instruments. The higher resolution of automatic data collection further refines the estimation of expert systems.
   In the first stage of work, the first version of the modules of DPS model developed for a selected plant (rapeseed) to be expanded in every production year was completed. The modules of the model, linked to production dates, describe the individual phases of production. The modules were formulated as flow charts, selecting the decision nodes.

Decisions can be automated if selecting options is possible from the stored data and the input requirements with a simple pairing algorithm. The hit accuracy of the process, similarly to donor search, depends on the size of the database. The project cannot undertake the software implementation of DPS algorithm because there is no large database for a given area and culture, structured according to the currently developed model.

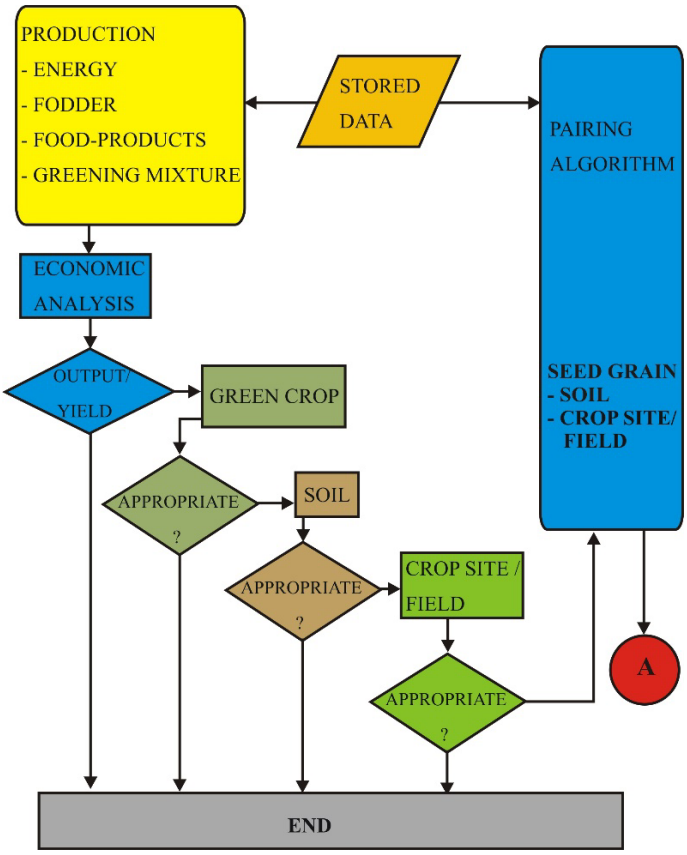

Figure 2. Flow chart of variety selection

3. Examining the agricultural applications of Big Data collection system

Big Data processing enables the representation of large amounts of data generated in agriculture, the search for patterns, relationships, and based on these, the development of new types of decision-making mechanisms. The agricultural applications of Big Data systems were studied in the following areas:

1. Mathematical interpretation of Big Data management. Intelligent agents.
2. Big Data processing methods.
3. Big Data type data storage and analysis methods.
4. The application of data mining methods.
5. GIS aspects of precision agriculture.

Suggested Big Data analysis methods:

- Grouping procedures
- Cluster analysis
- Wilks' λ Statistics

- Discriminant analysis
- Combined cluster and discriminant analysis (CCDA)
- Periodicity testing with averages, with Lomb-Scargle periodogram or wavelet transformation
- Identifying background processes by main component analysis (PCA)
- Applying machine learning tools for predicting and estimating environmental variables

Suggested Big Data analysis software:
Oracle NoSQL also supports multiple storage modes (key-value pairs, Avro, table) for large amounts of data. Data is distributed on multiple computers, even with copies, using distributed storage that guarantees high speed and security with scalability and transaction management.

The *Apache*-developed *Hadoop* system, which is a Java-based (open source) framework for processing and analysing large amounts of data, includes/implements the MapReduce programming model. Its own file system is HDFS (Hadoop Distributed File System), which is a distributed, scalable and portable file system written in Java. It supports the creation of server clusters consisting of low-cost hardware components.

To comprehensive data analysis, *Microsoft's* cloud-based service platform, *Azure*, is an excellent tool which now offers over 100 different service and tooling systems. Regarding the project, artificial intelligence-based solutions can be the most significant.

Oracle R is recommended from data analysis software. This software extends the open source statistical programming environment to Big Data, which allows statistical queries and graphical analysis of data stored in large amounts in Oracle databases. The relationship between Oracle R and Hadoop is implemented by Oracle R Advanced Analytics for Hadoop, a software that provides a general computing framework, enabling multiple map and reduce functions with the help of R language to be implemented in parallel in an HDFS environment. Software for high-level space and graph analysis services for the above-mentioned Hadoop and NoSQL environments is Oracle Big Data Spatial and Graph.

Correlations obtained as a result of data mining should again be interpreted by the appropriate experts from whom the task and the data are derived. Data miner cannot be an expert on all topics. It may well be that the obtained correlations are good, but they are worthless to the customer. For example, there is a strong correlation between the year of birth and age; the data miner obviously notices and finds it worthless, but for example, the vulnerability of a pest they cannot know.

4. Development of on-board IT systems

ISO 11783 (ISOBUS) is a communications protocol for the agricultural industry that is designed to ensure the standardization of communications between

tractors and machines. The range of ISOBUS users is constantly expanding, so the AEF (Agricultural Industry Electronics Foundation) has established certification laboratories worldwide that test the compatibility of products launched by machine manufacturers. One of the most important results of the Agroinformatics Technology FIEK product approach development can be the successful establishment of a test centre recognized by the AEF during the term in Gödöllő.

The first task of the research team is to get acquainted with the requirements and data coding system of ISO 11783 standard, and to compile a list of laboratory tools necessary for testing the conformity of agricultural machines to the ISOBUS standard, and to develop test methods. The University has obtained the ISOBUS conformity testing tools and software recommended by the AEF from its own resources, including on-line access to the AEF database for the duration of the first stage of work. Our staff completed a preparatory training course for studying ISOBUS systems organized by RO-SYS Ltd. and performed tasks applying the intelligent agricultural tools of the Faculty of Mechanical Engineering.

Figure 3. SZIU's retrofit system

ISOBUS is based on the CAN protocol developed for the automotive industry and the SAE J1939 standard describing the internal network of trucks, which allows reliable data transfer under extreme conditions, but the amount of communicated data is limited. ISOBUS network therefore only transmits data that is called by a subsystem. The development of the system and the adaptation of new sensors assume bit-level knowledge of data traffic. Our research team has developed a method and a tool that can read and save its data traffic connected to ISOBUS network. The device has been manufactured in several copies as it

replaces the coupling element of ISOBUS conformity testing system, so it is not necessary to shake the expensive tool in the tractor cab for field tests.

Our goal is to develop a minimum ISOBUS-compatible configuration (retrofit system) for used power machines in the country that do not have intelligent technology.

This also makes machines work with older tractors that do not work without ISOBUS connection or malfunction with an error code. The system has been installed in a Claas Ares 567 land-utility tractor of the year 2006, but it can also be used to make any of the simple East European (MTZ, Zetor) or Asian (Chinese, Indian) tractors "smart". It does not require any servo steering system in this installation. The device includes a universal terminal (ÚT), a 10-channel machine phase controller (iECU), a GPS navigation system, a travelling speed sensor, and an ISOBUS wired network.

5. Infrastructure development

Szent István University has also undertaken to establish a contact and cooperation centre in the project "Establishment of Agroinformatics, Higher Education and Industrial Cooperation Centre". The objective of the project is to develop the building of the AgIT FIEK research centre as a new investment, in SZIU area with its seat in Gödöllő. According to the plans the building will include an industrial hall in which the largest agricultural machinery will also be able to be examined indoor in a tempered environment. The centre will provide place for an engineering development office, electronics and prototype workshops, an ISOBUS and sensor technology testing laboratory with anti-static flooring, and a properly arranged instrument warehouse for equipment purchased in the project. There will be two rooms for adult training courses on the upper floor of the building. Being built within the framework of the project, the Agroinformatics Centre will be connected to the Engineering Information Centre of SZIU Faculty of Mechanical Engineering with a covered-way, which allows the project to use the University's IT infrastructure.

References

[1] I. SZABÓ; M. HUSHKI; Z. BÁRTFAI; L. KÁTAI: Operator’s behaviour measuring methodology inside off-road vehicle cabin operator’s focusing scheme
In: Agronomy Research, Volume 15. No. 5. 2017. p. 2172-2182**.** ISSN 1406-894X, https://doi.org/10.15159/AR.17.033

[2] SZABÓ I.; M. HUSHKI; BÁRTFAI Z.; KÁTAI L.: THE CHANGE ON OPERATOR’S FOCUSING SCHEME INSIDE A MULTI- TASKING OFF-ROAD VEHICLE ALONG WORKING HOURS
In: Hungarian Agricultural Engineering, No. 33/2018 p. 30-37. HU ISSN

0864-7410, DOI: 10.17676/HAE.2018.32.30
[3] I. SZABÓ; M. HUSHKI; Z. BÁRTFAI; A. LÁGYMÁNYOSI; L. KÁTAI: Modelling of operator's focusing scheme along working hours: Windrowing and cultivating operations
In: Agronomy Research, Volume 16. No. 4. 2018. p. 1885-1895. ISSN 1406-894X, https://doi.org/10.15159/AR.18.155
[4] I. SZABÓ, M. HUSHKI, Z. BÁRTFAI, L. KÁTAI (2017): The change on Operator's focusing scheme inside a multi-tasking off-road vehicle along working hours, Towards Sustainable Agricultural and Biosystems Engineering, Győr, Hungary, pp. 191-206. ISBN 978-615-5776-03-8

This research has been supported by the NKFIH *FIEK_16-1-2016-0008* project.

Development of 3D printing raw materials from plastic waste

OUSSAI Alaeddine[1], Zoltán BÁRTFAI[1], László KÁTAI[2], István SZALKAI[3]
[1]Department of Agricultural and food Industrial Machines,
Institute for Mechanics and Machinery
[2]Department of Machine construction,
Institute for Mechanics and Machinery
[3]FKF Nonprofit ZRT

Abstract

40 years ago, re-utilization of post-buyer bundling as glass containers and jugs was normal. There are restrictions to the excessive and extensive usage of inflexible compartment re-utilization; which are at any rate usually estimated. The dissemination and accumulation focus are generally far away from unified item filling manufacturing plants and would bring about impressive back-pull separations.

Also, the extensive variety of compartments and packs for marking and promoting purposes makes coordinate reclaim and refilling less practical. Reclaim and refilling plans do exist in a few European nations (Institute for Local Self-Reliance 2002), including PET containers and also glass, however they are somewhere else for the most part considered a specialty movement for neighbourhood organizations as opposed to a sensible vast scale procedure to lessen bundling waste.(Saikia & de Brito, 2014).

Plastic aggregates used in many studies prepared from plastic waste obtained from different sources. As example plastic bottles were grinded in the laboratory by using a grinding machine and then sieved to get the suitable size fraction. (Frigione, 2010).

Keywords

3D printing, plastic, recycling, extrusion, filament

1. Introduction

3D technologies, design, additive manufacturing and modelling have been studied at length at the Institute of Mechanics and Machinery (Szabó et. al., 2011, 2012) for a decade. Having studied the applied plastic recycling technologies, materials for 3D printing and the 3D printing technologies it is realized that the quantity and quality of plastic waste differs from country to country and from company to other. In the case of waste plastics that are

recyclable and reusable, the most widely used are polyethylene terephthalate (PET, used for synthetic fibres and water bottles), and second high-density polyethylene (HDPE, used for jugs, bottle caps, water pipes).

The current applications for using recycled plastics in fabrication and design are fairly limited, on a small scale, plastics (such as ABS, HDPE, or PET) are shredded and formed into pellets, and then either extruded into filament to be used in existing 3D printers, or injection moulded into small parts and pieces of larger components. At a large scale, recycled HDPE is melted into sheets and either used directly as sheets in construction, or then heat formed from a sheet into components for construction. These methods of fabrication using recycled plastics are the norm because of their affordability and straightforward processes, yet each method leaves some complexity to be desired (Al-Salem, Lettieri, & Baeyens, 2009).

Regarding to the recycling technology, the previous methods of recycling and recovery routes for solid plastic waste are detailed and discussed covering:

- re-extrusion
- mechanical treatment
- chemical treatment
- energy recovery

Based on the previous research I performed on this field, the main objective of my project is the contribution to the development of sustainable, effective technologies on the field of plastic recycling, both from the economic and ecological point of view

Plastics recycling is complex and sometimes confusing because of the wide range of recycling technologies and recovery activities(Hopewell, Dvorak, & Kosior, 2009).

These include the following categories:

- mechanical reprocessing into a product with equivalent properties,
- secondary mechanical reprocessing into products requiring lower properties,
- recovery of chemical constituents (Flores, 2008) and
- quaternary recovery of energy .

Recycling technology, the work will be on Polyethylene terephthalate PET and polylactic acid as mixed polymers PLA.

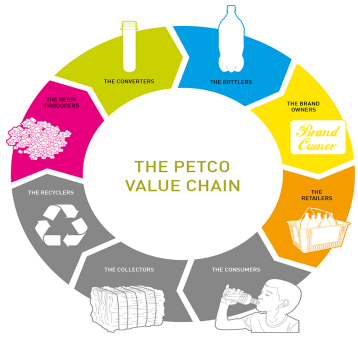

Figujre 1. PET recycling circle

2. Recycling PET

The main production for PET is for the applicability of synthetic fibres (in excess of 60%) with bottle production accounting for around 30% of global demand. In terms of textile applications, PET is generally referred to as simply "polyester". The terminology “PET" is used generally used for packaging applications. The polyester industry makes up about 18% of world polymer production and is third largest industry after polyethylene (PE) and polypropylene (PP). (Rahmani et al., 2013).

PET composes of polymerized units of the monomer ethylene terephthalate, with repeating C10H8O4 units. PET is recycled quite frequently and has the number "1" as its recycling symbol. The first PET was patented in 1941 by John Rex Winfield, James Tennant Dickson and their employer the Calico Printers' Association of Manchester and the PET bottle was patented in 1973 by Nathaniel Wyeth. PET is also used as substrate in thin film and solar cell (Bornak, 2013).

As, PET is an excellent barrier material, it is commonly used for producing plastic bottles; especially for the soft drinks. For some special bottles, the PET also sandwiches an additional polyvinyl alcohol for further reducing its oxygen permeability.

Table 1.: End markets for PET recirculates in Europe and in the USA (*Petcore, 2011; Napcor, 2011*).

Year	Percentage fibre	Sheet	Bottle (food, non-food)	Strapping	Other
2001					
EU	62	16	7	10	5
USA	62.1	5.3	17.3	11.7	3.6
2005					
EU	57.0	16.2	15.2	7.8	3.8
USA	53.6	8.2	20.6	15.2	2.4
2009					
EU	40.5	27.0	22.0	7.0	3.5
USA	36.7	17.0	28.6	12.2	5.5

Bi-axially oriented PET film (often known by one of its trade names, "Mylar") can be aluminized by evaporating a thin film of metal onto it to reduce its permeability, and to make it reflective and opaque (MPET). The above-mentioned properties hold applications in many domains like the flexible food packaging, thermal insulation for instance for the “space blankets“. As, it has a high mechanical strength; the PET film is also commonly used in tape applications for example for the carrier of the magnetic tape or backing for the

pressure sensitive adhesive tapes.(Welle, 2011).(Tafheem, Islam Rakib, Esharuhullah, Reduanul Alam, & Mashfiqul Islam, 2018).

The non-oriented PET sheet can undergo thermoforming and used to make packaging trays and blisters. If the crystallisable form of PET is used, it can be used to prepare frozen dinners as they have the capability to withstand the freezing and the oven baking temperatures. Filling these with glass particles or fibres makes them stiffer and durable. (Hopewell et al., 2009)

3. Recycling mixed polimeres

Polylactic acid (PLA) and its systems PLA are one of the most vital biodegradable polyesters derived from renewable sources i.e. starch and sugar. Till the last decade, the main applications of PLA were limited to biomedical and pharmaceutical applications such as implant devices, tissue scaffolds, and internal sutures due to its high cost and low molecular weight. Since, the existence of both hydroxyl and a carboxyl group in lactic acid allows it to be converted directly into polyesters via a polycondensation reaction; a considerable amount of interest has been paid to the academic research associated with PLA polymer and its copolymers (3e5). Although PLA is a biodegradable material, which would significantly reduce environmental pollution associated with its waste, the knowledge behind this material recycling and changes in the properties of PLA upon its multiple processing is a very important subject of discussion (Wasan Ismail Khalil & Khalaf Jumaa Khalaf, 2017).

Polyvinyl chloride (PVC) and its systems along with the low cost and high performance of PVC products combined together with its wide range of properties that can be obtained from different formulations has contributed to the widespread use of PVC in construction products. There has been a long time-lag between PVC consumption and the amassing of PVC waste arising from the long life of PVC products, which can be up to 50 years. It is quite clear that all produced PVC will eventually become waste in a few days' time. The European Association of Plastics Converters (EuPC) has estimated that the PVC waste for the periods between 2010 and 2020 will arise from the following sources. Many works have documented the recycling of PVC and its systems since the beginning of the last decade.(Kou et al., 2009).

Polyethylene's PE's are one of the most widely used plastics characterized by a density in the range 0.918e0.965 g/cm3 resulting in a range of toughness and flexibility. Their major application is in packaging film although their outstanding dielectric properties. Chemical recycling of PLA/PE and PLA/PBS blends.

4. Recycling technologies

Recent research points the way towards chemical recycling methods with lower energy requirements, compatibilization of mixed plastic wastes to avoid the need

for sorting, and expanding recycling technologies to traditionally non-recyclable polymers.

We mentioned the recycling technologies from which we concluded that mechanical recycling is the only widely adopted technology for large-scale treatment of plastic solid waste. The main steps were the removal of organic residue through washing, followed by shredding, melting, and remoulding of the polymer, which is often blended with virgin plastic of the same type to produce a material with suitable properties for manufacturing.

There are limitations to mechanical recycling technologies because each type of plastic responds differently to the process depending on its chemical makeup, mechanical behaviour, and thermal properties. Temperature-sensitive plastics, composites, and plastics that do not flow at elevated temperatures (as in the case of thermosets) cannot be processed mechanically. Consequently, only two types of plastic are recovered and recycled with mechanical processes: poly (ethylene terephthalate) (PET) and polyethylene, which represent 9 and 37% of the annual plastic produced, respectively. All other plastic solid waste is either not recovered or in amounts representing less than 1% of production. According to the most recent U.S. Environmental Protection Agency report, a mere 8.8% of all plastic produced in the U.S. annually is recovered from municipal solid waste and then incinerated, recycled, or industrially composted. The recycling rate is slightly higher in Europe, at ~ 30% for plastic waste.

In a previous research we found solution for grinding and extruding plastic in small scale, using machines with two different parts: crusher, extruder and mixed it together.

The crusher consisted of 12 blades twelve anvil-blades, right axis, left axis, cover, sieve, fourteen casing spacers, four nuts, two pins and crank. (Oussai, Bártfai, & Kátai, 2018).

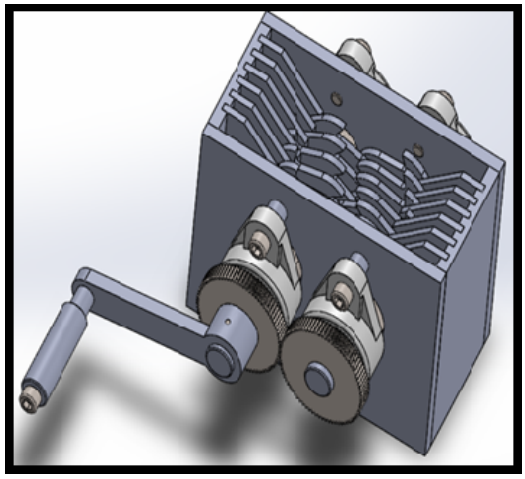

Figure 2. Overview of the complete design of the crusher

The extruder consisted of: hopper, room of extrusion, heating collar, chain transmission, nozzle, engine support, engine, control panel and the extruder support. The component which was most important in the extruder was the extrusion screw that acts like a screw pump, fits in the room.

The function of the screw was to move the pieces of plastic inserted through the hopper along the length of the room

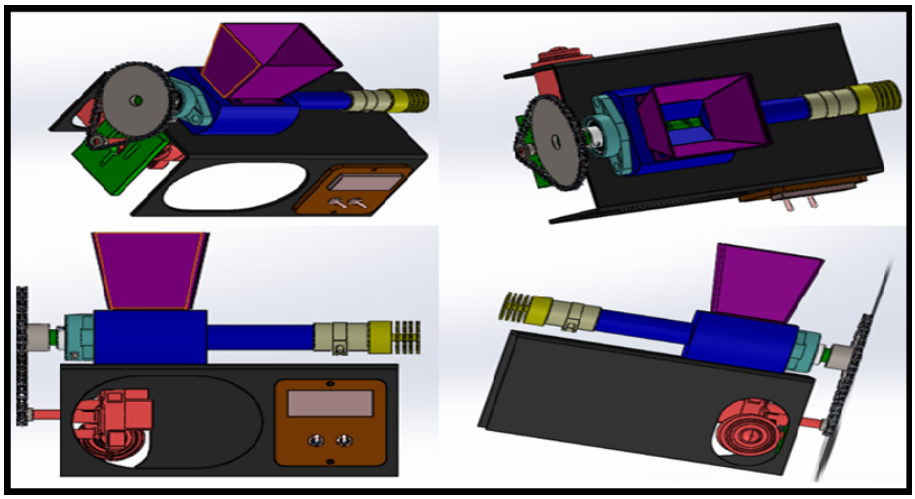

Figure 3. Overview of the complete design of the extruder

Current technologies that move beyond mechanical recycling include pyrolysis (thermolysis) to selectively produce gases, fuels, or waxes through the use of catalysts; are referred to as chemical recycling. Chemical recycling is not a widespread recycling practice, mainly because of energy costs. A further option is the incineration of materials and collection of energy in the form of heat. Incineration is convenient for the treatment of mixed waste because it avoids the need for sorting, but it does not allow for the recovery and reuse of the starting components once burned. It also does not save as much energy as recycling.

Conclusion

The environmental consequences of plastic solid waste are visible in the ever-increasing levels of global plastic pollution both on land and in the oceans. But, although there are important economic and environmental incentives for plastics recycling, end-of-life treatment options for plastic solid waste are quite limited in practice. Pre-sorting of plastics before recycling is costly and time-intensive, recycling requires large amounts of energy and often leads to low-quality

polymers, and current technologies cannot be applied to many polymeric materials. In the current scenario there is growing demand and interest towards chemical recycling methods with low energy demand along with compatibility of mixed plastic waste to overcome the need for sorting and expanding the recycling technologies to traditional non-recyclable polymers

References

[1] Al-Salem, S. M., Lettieri, P., & Baeyens, J. (2009). Recycling and recovery routes of plastic solid waste (PSW): A review. Waste Management, 29(10), 2625–2643. https://doi.org/10.1016/J.WASMAN.2009.06.004

[2] Bornak, R. (2013). Different Methods of PET Production and Its Economy Different Methods of PET Production and Its Economy. *European Journal of Scientific Research*, (December), 2–3.

[3] Flores, M. C. (2008). Plastic Materials and Environmental Externalities Plastic Materials and Environmental Externalities : Structural Causes and Corrective Policy Table of Contents Plastic Materials and Environmental Externalities Plastics Recycling : Law and Economics. *Lethbridge Undergraduate Research Journal*, *3*, 2–7.

[4] Frigione, M. (2010). Recycling of PET bottles as fine aggregate in concrete. *Waste Management*, *30*(6), 1101–1106. https://doi.org/10.1016/J.WASMAN.2010.01.030

[5] Hopewell, J., Dvorak, R., & Kosior, E. (2009). Plastics recycling: challenges and opportunities. *Philosophical Transactions of the Royal Society B: Biological Sciences*, *364*(1), 2115–2126. https://doi.org/10.1098/rstb.2008.0311

[6] Kátai L., Szabó I., Lágymányosi A., Lágymányosi P., Szakál Z.: Additív gyártástechnológiában alkalmazott anyag szilárdsági jellemzőinek vizsgálata a 3D nyomtatás paramétereinek függvényében In: Gép, LXIX. évf. 4. szám, Miskolc, 2018, 45-48. o., ISSN 0016-8572

[7] Kou, S. C., Lee, G., Poon, C. S., & Lai, W. L. (2009). Properties of lightweight aggregate concrete prepared with PVC granules derived from scraped PVC pipes. *Waste Management*, *29*(2), 621–628. https://doi.org/10.1016/J.WASMAN.2008.06.014

[8] Oussai, A., & Bártfai Z. (2017). DESIGN AND SIZING OF A PLASTIC RECYCLING STATION INTO FILAMENTS FOR 3D PRINTER. In *Engineering, Agriculture and Green Industry Innovation* (pp. 1–6). budapest: synergy international conferences.

[9] Rahmani, E., Dehestani, M., Beygi, M. H. A., Allahyari, H., & Nikbin, I. M. (2013). On the mechanical properties of concrete containing waste PET particles. *Construction and Building Materials*, *47*, 1302–1308. https://doi.org/10.1016/J.CONBUILDMAT.2013.06.041

[10] Saikia, N., & de Brito, J. (2014). Mechanical properties and abrasion behaviour of concrete containing shredded PET bottle waste as a partial

substitution of natural aggregate. *Construction and Building Materials*, *52*, 236–244. https://doi.org/10.1016/J.CONBUILDMAT.2013.11.049

[11] Szabó I. – Kátai L.: Construction Design and Analysis with Computer Aided Engineering Tools.
In: Proceedings of Annual Session of Scientific Papers „IMT Oradea – 2012", Editura Universitatii din Oradea 2012., CD ROM Edition, Volume XI., NR 1/ 2. 135-141. ISSN 1583-0691

[12] Szabó, I. – Kátai, L. – Csomai, R.: 3D Scanning and Computer Analysis of Morphological Aspects for Agricultural Applications.
In: Hungarian Agricultural Engineering, 23/2011 December p.105-108. HU ISSN 0864-7410

[13] Szabó, I. – Kátai, L. – Csomai, R.: Application of 3D Scanning in Engineering Design and Analysis
In: Mechanical Engineering Research, Volume 7. 2012. p. 81-91. HU ISSN 2060-3789

[14] Tafheem, Z., Islam Rakib, R., Esharuhullah, M. D., Reduanul Alam, S. M., & Mashfiqul Islam, M. (2018). Experimental investigation on the properties of concrete containing post-consumer plastic waste as coarse aggregate replacement | Request PDF. *Journal of Mater Ials and Engineering Structures*, *5*(March), 23–31

[15] Wasan Ismail Khalil, & Khalaf Jumaa Khalaf. (2017). Eco-Friendly Concrete Containing Pet Plastic Waste Aggregate. *Diyala Journal of Engineering Sciences*, *10*(01), 92–105. Retrieved from https://www.iasj.net/iasj?func=fulltext&aId=126163

[16] Welle, F. (2011). Twenty years of PET bottle to bottle recycling–An overview. *Resources, Conservation and Recycling*, *55*(11), 865–875. https://doi.org/10.1016/J.RESCONREC.2011.04.009

Thermal analysis and improvement of pulley

Muath S. TALAFHA, István OLDAL
Department of Mechanics, Institute for Mechanics and Machinery

Abstract

The primary function of a transmission is to transmit mechanical power from a power source to some form of useful output device. Since the invention of the internal combustion engine, it has been the goal of transmission designers to develop more efficient methods of coupling the output of an engine to a load while allowing the engine to operate in its most efficient or highest power range. Therefore, it has been making a thermal study on the pulley and belt mechanism because it's the most effective problem is the rise in temperature because it leads to slipping problem and wear out in the belt.
Therefor its suggested to modify the design of the pulley by adding a fins to increase the heat transfer area to reduce the temperature of the pulley.

Therefore, it has been created a model first one without fins and the second one with fins and we examine these model by using Ansys program, and after making the simulation, we got a good result showing after we add the fins we decrease the temperature by[24˚C] so found that our model is working and we expected to increase the lifetime of belt and we expected to reduce the problems which occurs in high temperature.

Keywords

Pulley and belt, thermal analysis, friction, belt lifetime, pulley design, Ansys software

1. Introduction

A research will develop to study the pulley and belt Transmission mechanisms and to Analyze the project by plotting the graph and to study the design and the thermal effect of friction on the mechanism and how to solve the high temperature problem on it to avoid the slipping problem and wear out in the belt and pulleys due to rise in temperature.

By using Ansys software, it has been made a study for the design and thermal effect on the pulley and belt mechanism under different operation situations:

A\ At normal operation condition without using fins.

B\ The thermal analysis of the mechanism by using fins.

C\ To compare the performance of the mechanism before and after putting the fins.

D\ Analyze the project by adding the graph.

The CVT was first used in an automobile at the end of 19th century and a V-belt type was used. By 1958, the Dutch company, DAF had manufactured more than a million rubber V-belt type CVTs but could not improve the product due to technical limitations in the movement for a higher output engine. However, this experiment is said to have spurred the development of a chain type (Borg Warner) CVT or a metal V-belt type (Van Doorne) CVT [1] The Van Doorne metal V-belt is a push type belt, which differs from the chain type in that the drive side pushes the follower side to transmit power. This belt was introduced into the market for the first time when it was mounted in Subaru JUSTY in 1987 [1] Subsequently, the Van Doorne metal V-belt has been used in many other types of vehicles and now constitutes approximately 10% of automatic transmissions.

Now in this paper, we want work on a rubber v belt to a chive the optimum operating circumstances for the rubber v belt as has been discussed by:[2] High belt temperature guides to Decomposing in polymer molecule chains and as a result of aging of rubber material, which highly effects on the V-belt lifetime. V-belt temperature above 70 °C creates a significant decline of expected belt lifetime. In (figure 1) it can be seen that in case of 10 °C rises in temperature the lifetime falls to half of its original value:

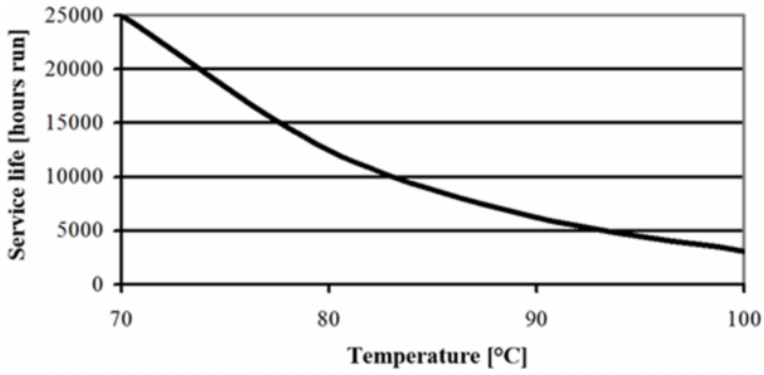

Figure 1. Correlation between temperature and service life [2]

According to[3]the power loss happening in V-belt drive can be essentially divided within two sides, the loss happens by external friction (Slip between the belt and the pulley) as well as the loss happens by internal friction (Slip among the molecules, hysteresis).

The heat generated in the V-belt can be described by the Baule-Mitscherlich saturation function (figure 2), in which the measured parameters change along a decreasing gradient going toward the saturation maximum. The steady operational temperature was precisely estimated through the mathematical model. This was necessary because each adjustment converged to different

Saturation during different times, and the duration of the experiments was decided to be 10 minutes. [4]

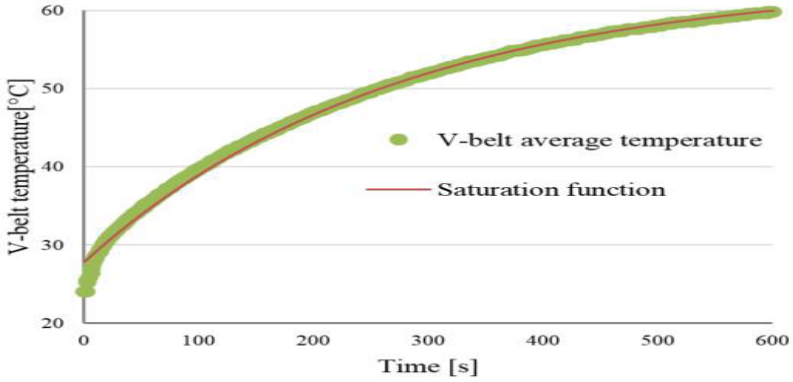

Figure 2. Measurement data and the saturation function [4]

As shownin figure (2) the temperature can be reach 60c˚within 10 minutes so in this paper, we are going to solve the raise in v belt temperature by making some modification in the pulley design by aaddingcooling fins on the pulley to increase the heat transfer area so in this case we trying to maintain the temperature of the v belt in the optimum working temperature.

2. Materials and methods

Introduction

Our task is to simulate a pulley and belt mechanism and study, the temperature of belt and heat transfer between the pulleys and the surrounding environment temperature and we want try to decrease the temperature of the pulley to decrease the temperature of the belt in order to increase the life of the belt and to reach the optimum working environment for the belt, because of that we want make a simulation in computer for this mechanism, and to make the simulation we want use the ansys program to implement the simulation.

Equipment and tools

We use a drive and brake units which were located on the grooved table of the test bench offer many opportunities. The drive parameters of motor units can be measured accurately with the transmitters shown in (Figure 22). For the belt tests the drive unit is equipped with a tensioning unit guided by a linear bearing. The pretension of the belt can be adjusted with a screw spindle, whose line of action coincides with that of the shaft pulling force. This arrangement is used to measure the shaft pulling force directly.

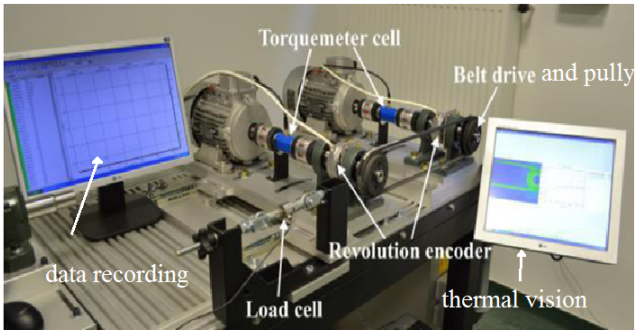

Figure 3. The arrangement of the test bench to test belt drives [4]

The temperature of the V-belt is determined by the equilibrium of the generated heat and heat loss. This is affected by several not easily controllable factors, such as air temperature, humidity, the temperature and heat capacity of the contacting parts, etc. During the experiments the mentioned not easily controllable factors were considered constant as the measurements were taken under the same circumstances. The temperature rise of the V-belt was chosen as the test parameter, which means the power loss between the two equilibria – between the steady state of the workshop temperature and operating temperature[4]

Numerical model

Ansys develops and markets finite element analysis software used to simulate engineering problems. The software creates simulated computer models of structures, electronics, or machine components to simulate strength, toughness, elasticity, temperature distribution, electromagnetism, fluid flow, and other attributes. Ansys is used to determine how a product will function with different specifications, without building test products or conducting crash tests.

Therefore. it has been built a two mechanical model to cover the two situations the first situation the mechanism without the fins and the second model is the mechanism after adding the cooling fins.

Geometry

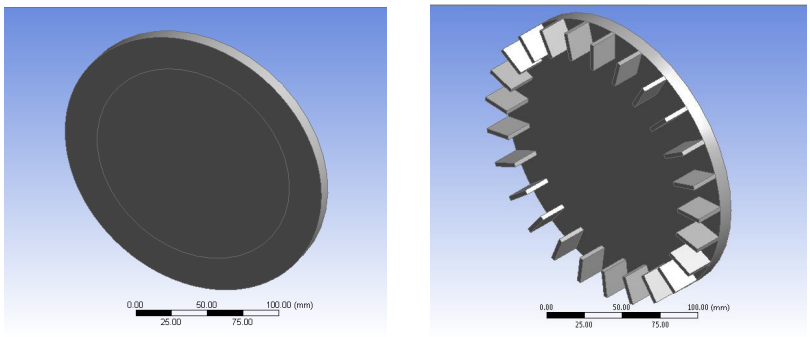

Figure 4. Both models with and without cooling fins

Now, after the model has been drew it can add the rotating zone and the open zone to simulate the operation conditions.

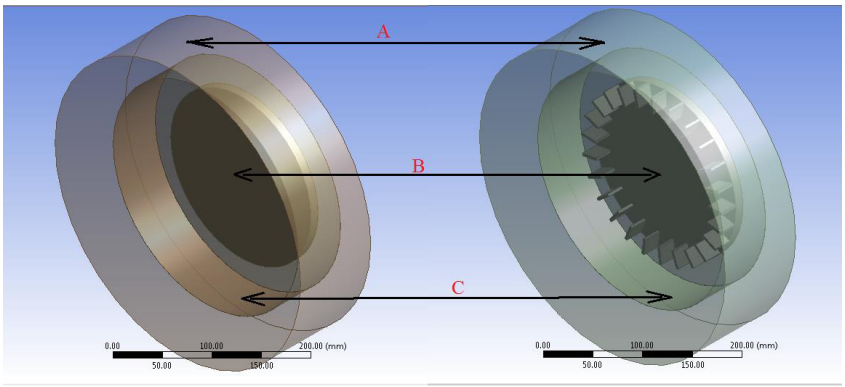

Figure 5. Two Models:(A open zone)(B solid part)
(C rotating zone)

As it shown in figure (5) it has been drown the three domains first one is the solid model it will simulate the model conditions the second one is the rotating zone, which will simulate the air around the model and the outer zone will simulate the surrounding environment.

It has been made a CFX MODEL to analyze the pulley and the meshing information for the model the solid part has a (5994) nodes and (23382) elements and the hall model contain the solid part and rotating zone and the open zone have a (103310) nodes and (486271) elements, solid part is a steel structure with rotating speed (2000 RPM), the rotating zone is a fluid domain air at 25℃ and 1 bar and the open zone is an fluid domain air at the same operation conditions and for boundary condition the solid part is contact the rotating zone in a solid fluid interface and heat transfer with (6000 w\m²) heat flux and the rotating zone is contact with the open zone in fluid fluid interface and the heat transfer is Conservative Interface Flux and for open zone is contact with the surrounding in fluid fluid interface with heat transfer opening temperature

3. Result and discussion

The simulations deal with two models normal one without fins and modified one with cooling fins and after making the examination of the two models its record these results.

Temperature of the model

As shown in (figure 6) we can see the distribution of the temperature for the pulley and we can see the maximum temperature is located at the outer area of the pulley

and the minimum temperature is at the inner (center) of the pulley, and this result is realistic result because the heat generate at the outer area which is the region where the belt have frictional contact with the pulley and after adding the fins we reduce the temperature from [60˚c to 40.7˚c], so the modification we make in this model is working, and the reduction in the temperature happen because we increase the heat transfer area and the air velocity by adding the fins.

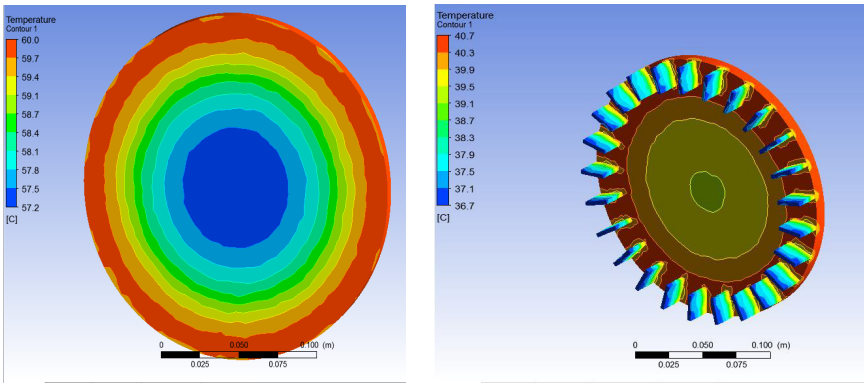

Figure 6. Temperature of the pulley for the both models

Air velocity

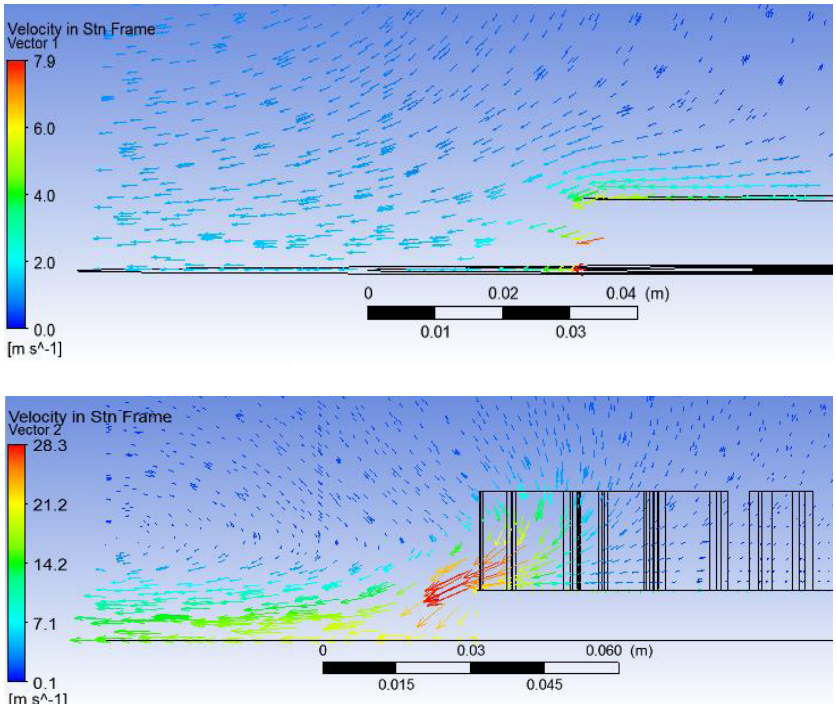

F*igure 7.* Air velocity for the both models

And here in (figure 7) it shown the distribution of the air around the pulley which caused by the rotation movement of the pulley , and as we can see here from the vector flow diagram the velocity of the air is relatively have small value because of that the heat transfer between the pulley and the surrounding will have small value, because the convectional heat transfer depend on the turbulence of the air _which we will see it in the streamline figure_ as the air have high value the turbulence will increase which makes the boundary layer between the pulley and the surrounding decreased so the heat transfer will be fast and the reduction of the temperature will be fast as will.and after adding the finsthe velocity of the air is have high value almost 4 times larger than the first model because of that we have a smaller temperature value than the first model even we run the second model with the same conditions for the first model, but we got less temperature value.

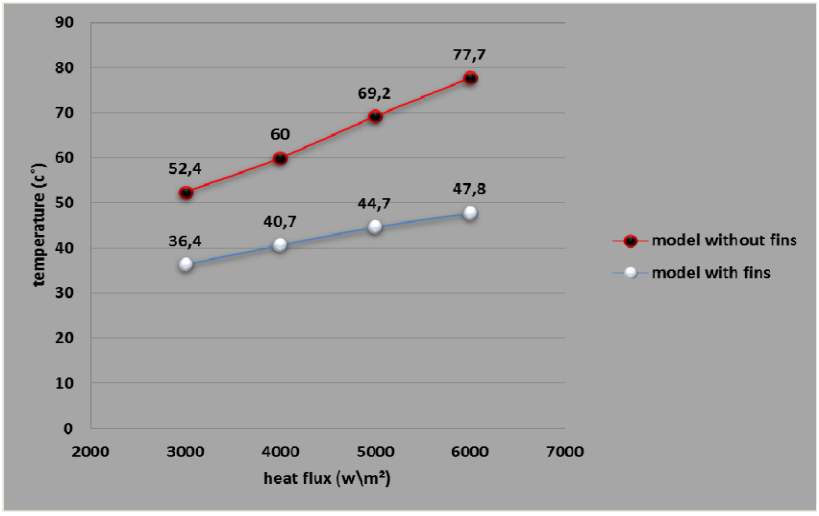

Figure 8. Temperature vs heat flux

Conclusion

After making the experiment and examination on the pulley we can summarize our result by these conclusions:

1. After making the modification by adding the fins to our model we almost increase the velocity of air around the pulley [4times].
2. The convectional heat transfer increase because we increase the turbulence in the air by increasing the velocity of the air, because the convectional heat transfer coefficient depends on it.
3. We reduce the average temperature of the pulley by [22.5˚c].
4. According to the [figure 1] which show the working environment circumstances for the belt and to [figure 8] which show our results, we can

say after adding the cooling fins we reach the optimum working environment for the belt.

5. According to [2]it have been mentioned that if the temperature of the belt increase 10 degree the life time of belt will decline by the half.so in our case we reduce the temperature by [22˚c]so we expected to increase the lifetime of belt by double.

So, we can summarize the conclusion by saying after adding the cooling fins to the pulley we increase the velocity of the air around the pulley and by increasing the velocity of air we increase the turbulence of air and by that we increase the Reynolds and Nusselt number, so the convectional heat transfer coefficient will increase and by that the convection heat transfer will increase and the temperature of the pulley will decrease.

References

[1] K. Asano, "Koyo's approach to continuously variable transmissions (CVT) for automobiles," *Koyo Eng. J. English edn*, vol. 1, no. 5, pp. 14–18, 2004.

[2] L. Kátai, P. Szendrő, and P. Gárdonyi, "The power transmission stability and efficiency of V-belts," *Prog. Agric. Eng. Sci.*, vol. 12, no. 1, pp. 25–49, 2016.

[3] L. Kátai and I. Szabó, "Identification of V-belt power losses with temperature measurement," *J. Mech. Sci. Technol.*, vol. 29, no. 8, pp. 3195–3203, 2015.

[4] P. Gárdonyi, L. Kátai, and I. Szabó, "EXAMINATION OF DRIVE MISALIGNMENT AND V-BELT TEMPERATURE CONDITIONS," 2016.

Invited Papers

1. Jozef RÉDL, Dušan PÁLEŠ, Juraj MAGA, Gábor KALÁCSKA:
Comparison rain-flow and range count of stress data processing methods

The authors' team is research partner of the faculty in the field of agricultural and mechanical engineering.

2. Dani RUSIRAWAN, Bill A. HAKAMA, Ari HADIWINOTO, Muhammad P. N. SIRODZ, Liman HARTAWAN, Mohammad A. MAHARDIKA, István FARKAS:
Effect of cooling on the performance of a small-scale solar power plant system

The authors' team is research partner of the faculty in the field of energetic research and process modelling.

Comparison rain-flow and range count of stress data processing methods

Jozef RÉDL[1], Dušan PÁLEŠ[1], Juraj MAGA[2], Gábor KALÁCSKA[3]
[1]Department of Machine Design, Faculty of Engineering,
Slovak University of Agriculture in Nitra, Slovakia
[2]Department of Machines and Production Systems, Faculty of Engineering,
Slovak University of Agriculture in Nitra, Slovakia
[3]Institute for Mechanical Engineering Technology, Faculty of Mechanical Engineering,
Szent István University, Gödöllő, Hungary

Abstract

The paper discusses the using of the range count method for processing of experimental stress data. We measured the vibration of the plow frame with an acceleration sensor mounted on its frame. The obtained data was transformed into the time depend stresses data set. A mathematical model of the range count method has been created and used in the environment of PTC® Mathcad Prime® 4. The Microsoft™ Excel® spread sheet helped us to prepare the input data from which we exported data to the Mathcad Prime® 4 software. We have compared the results of raw and filtered data from the record as well as the published results of the rain-flow method with the range count method.

Keywords

plough vibration, signal processing, stress counting methods

1. Introduction

In many application of constructions life analysis were used the strain gauges to measure the stress in the materials under the random loading. The measurement is complicated because the gauges must be glued to the whole construction in the certain points and directions. Fatigue analysis methods was analysed by[8]. The time-domain approach was defined by [1,2] in which the response time history is calculated by static stress analysis by superimposing all stress influences from the applied loads at each time step, lacks the dynamics of the structure especially for vibration-based problems when a loading excites the natural frequencies of the structure. The use of strain gauges is possible for limited locations only and moreover requires early knowledge of critical fatigue locations. On the other hand, using the sensors of acceleration is very useful in measurement of vibrations of beams, where the beams are the components of the framed structures. Mathematical definition of Rain Flow Cycle (RFC) was first time defined by [4]. The method presented by [4] attaches to each maximum of the

strain function the amplitude of a corresponding cycle or two half cycles, which are evaluated independently from each other. Algorithm of RFC was applied by [3]. Practical application of RFC in fatigue life prediction was published by many authors. Between major work we can include [3,6,7,8].

2. Material and methods

Measurement system and object

Object for measurement was a plough Pottinger depicted on Figure 1. The basic parameters of plough are listed in the Table 1. [5]. Measurement on plough was realized on deep plow. The plowed ground was planar without rough parts. The plough was mounted on tractor Fendt Vario 930.

Table1. Parameters of plough

Parameter	Value	Unit
Manufacturer	Pottinger	
Type	Servo 65 Plus	
Mass (m_P)	3085	kg
Distance between bodies	1	m
Bodies	7	m
Beam ($a \times a \times t$)	0,16x0,16x0,005	m

Figure 1. Plough Pottinger

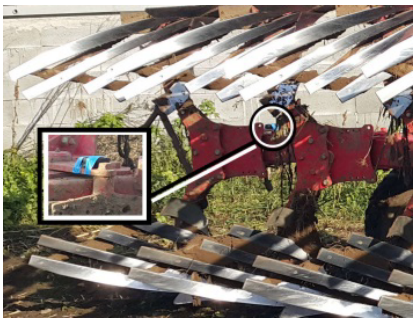

Figure 2. Detail of sensor location

Figure 3. Sensor Eval - ADXL 345Z-DB

For measurement of plough vibration was used the Eval - ADXL 345Z-DB data acquisition board. The board measured accelerations in the XYZ axes. Measured data was recorded to the MiniSD card. The relevant direction for us was the accelerations in Z axis direction.

Mathematical model

The mathematical and basic data processing is based on the work [8]. As mentioned below, the measured vibration data were transformed to the stress data set. For the transformation we designed the simple mathematical model based on the theory of cantilever beam design theory. We substituted the real plough with model as depicted on Figure 4. For utilizing the designed model we set up the basic assumption as follows:

- three-point linkage stiffness is similar as a fixed connection of the cantilever beam,
- for bending moment is used the effective length of plough,
- plough support wheel damping is contained in the acceleration data,
- used loading is the weight of the plough,
- neutral axis of the beam lay to the beam axis of symmetry,
- neglecting the shear deformation.

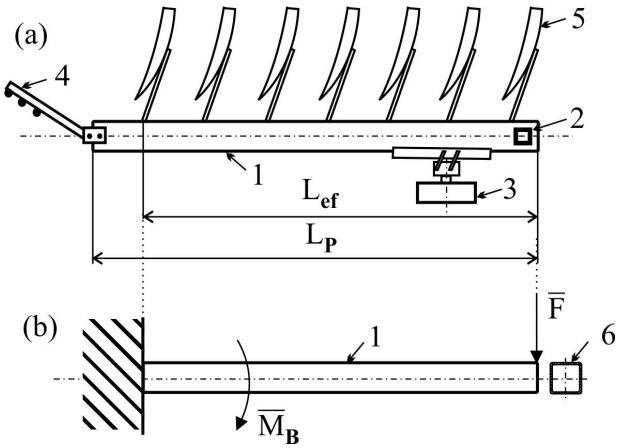

Figure 4. Plough and its model
a: 1-plough beam, 2-acceleration gauge, 3-wheel,
4-three point linkage mechanism, 5-body
b: 1-plough beam,6-beam profile, F -force, M_B - bending moment

The algorithm was designed for computer processing and all variables are indexed. Bending moments dataset solving was realized with Equation 1. The beam cross section modulus was derived from equation of moment of inertia for square tube. Final Equation is 2. Stress formula was derived from stiffness condition equation for simple bending. Combination of Equations 1,2 we get the Equation 3.

$$M_{B(i)} = m_P.ac_{(i)}.L_{ef} \tag{1}$$

where:

$M_{B(i)}$ – bending moment of the plough beam,

m_P – plough mass,

$ac_{(i)}$ – measured acceleration array,

L_{ef} – effective length of plough $= 6m$

Bending section modulus was solved by Equation 2.

$$W_B = \frac{a_1^4 - a_2^4}{6a_1} = \frac{1}{6}\left(a_1^3 - \frac{a_2^4}{a_1} \right) \tag{2}$$

where:

$$a_1 = a \text{ , } a_2 = a - 2t \text{ .}$$

For purpose of processing the experimental data we transformed acceleration dataset to the stress data set. Finally we get a formula for stress of beam with Equation 3.

$$\sigma_{B(i)} = \frac{6.a_1 m_P.ac_{(i)}.L_{ef}}{a_1^4 - a_2^4} \tag{3}$$

We processed the raw accelerations data set and filtered data set. Stress dataset from raw data is depicted on Figure 5. The raw accelerations data was filtered with Butterworth maximally flat magnitude filter, see Equations (4). The transformed data from filtered dataset is depicted on Figure 6.

$$B_n(s) = \prod_{k=1}^{\frac{n}{2}} \left[s^2 - 2.s.\cos\left(\frac{2k+n-1}{2n}.\pi \right) + 1 \right], n = even$$

$$B_n(s) = (s+1) \prod_{k=1}^{\frac{n-1}{2}} \left[s^2 - 2.s.\cos\left(\frac{2k+n-1}{2n}.\pi \right) + 1 \right], n = odd \tag{4}$$

where :

n – order of filter

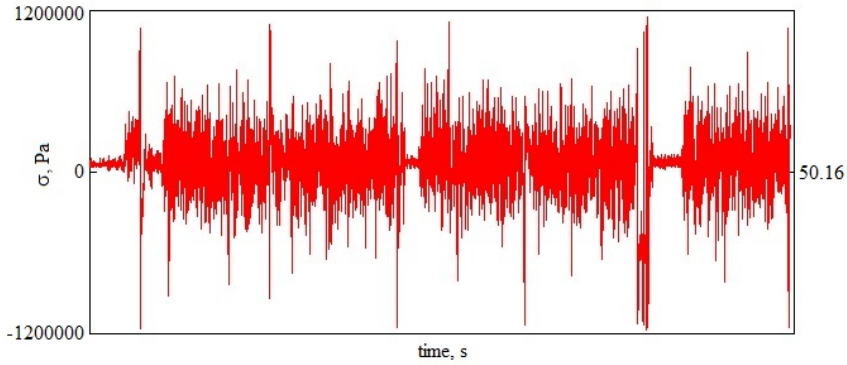

Figure 5. Stress from raw data

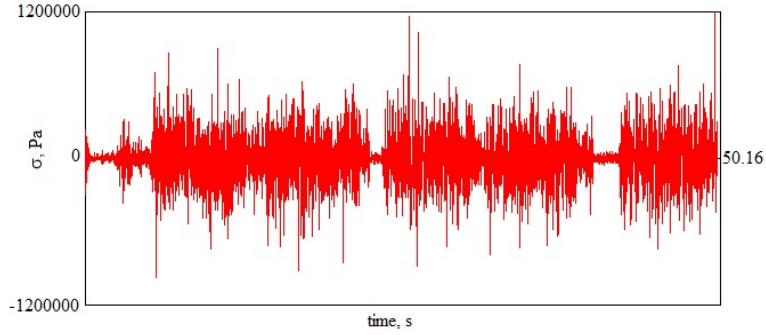

Figure 6. Stress from filtered data

Range count and rain-flow counting methods

The rain-flow counting method was applied on the same data set and the results were published in [6]. As defined in [4] the range count method (RCM) is the one-parametric counting method. Applied loads vectors are separated to the half oscillations. The total damage is defined as a sum of all damages in all half oscillations. The amplitude of the stress is defined as an absolute value of the difference of consecutive stress extremes.

$$\Delta\sigma_j = \left|\sigma_{j+1} - \sigma_j\right| \tag{5}$$

3. Results and discussion

Applying the RFC methodical steps published in [6] we got the dependency chart of the mean and amplitude from the raw data set. The chart is depicted in the figure 7. The same data set were processed with the RC method using the equation 5. The

result is depicted in figure 8. Comparison the means distribution in the charts 7, 8 we can assume that the RC method (from raw data) has widely stowed the means from data like the RFC method, but the data interval is the same.

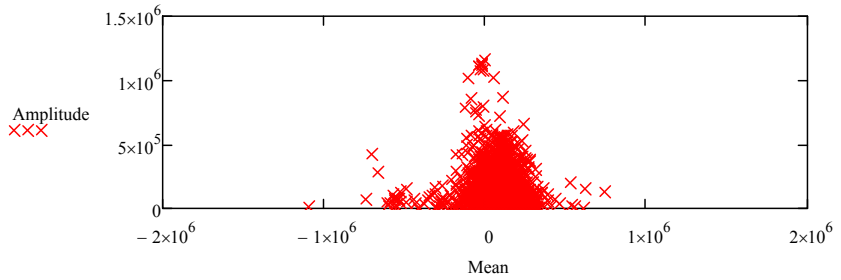

Figure 7. Stress raw data with RFC method

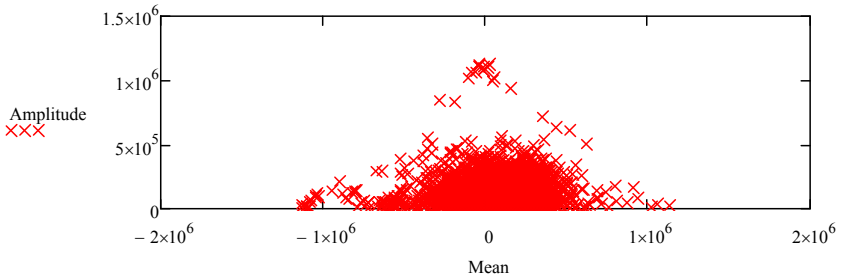

Figure 8. Stress raw data, RC method

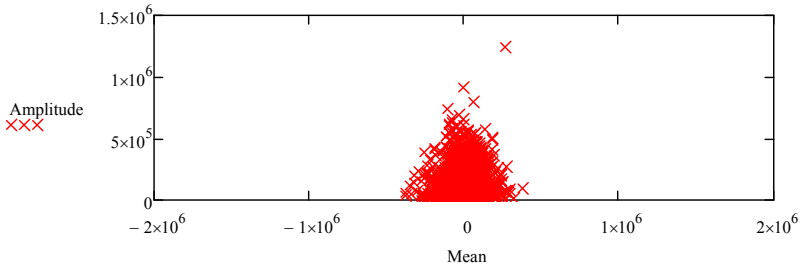

Figure 9. Stress filter data, RFC method

Comparison of the RC and RFC charts gives us the opinion, that the RFC method (form filtered data) gives us the means concentrated near to the zero and dispersion of the data is reduced to the minimum level. RFC method gives the analysts the information about the concentrating the stress values in materials. On the other hand, the filtered data processed with RC method are spread near to the interval $\langle -0, 9.10^6, 1.10^6 \rangle$. The negative values means that the loading is

pressure and the positive values means that the loading is tension. With RFC algorithm we removed the no relevant values from stress data set. Another significant parameter about distribution of data is histogram. In Figure 11 we can see counts histogram of means and amplitudes for stress data processed with RFC method. In Figure 12 we can see counts histogram of means and amplitudes for stress data processed with RC method. The distribution data in rain-flow matrix (Figure 11) is more uniformly as on Figure 12.

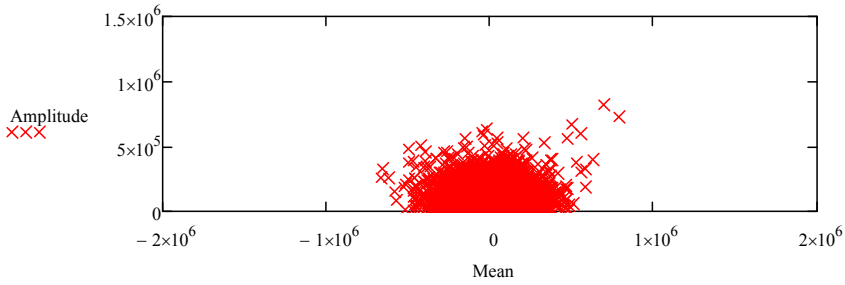

Figure 10. Stress filter data RC method

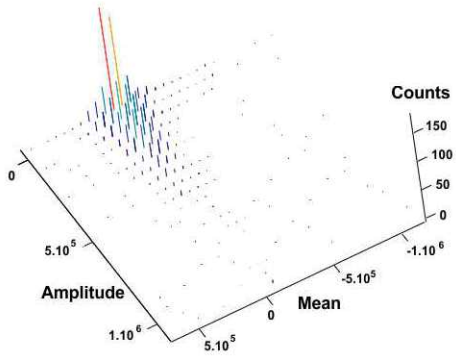

Figure 11. RFC matrix histogram

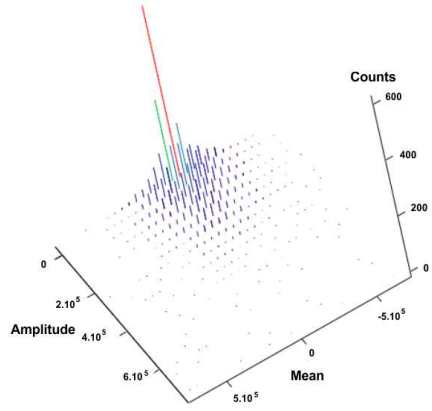

Figure 12. RC matrix histogram

Conclusions

In this paper we are dealing with comparison of stress data processing methods. We were used the rain-flow counting algorithm and range-count algorithm. Data was obtained from experimental measurement of vibration on plough frame. The accelerations were converted to the stress time series. For signal processing we used the Butterworth maximally flat magnitude filter. In software Mathcad Prime 4 we were designed the algorithm for establishing the relevant stress dataset by RFC method and RC method. We were processed the raw and filtered

data. Result of RFC is rain-flow histogram matrix. Result of RC is range-count histogram matrix. From analysis we get the result that the raw data gives more irrelevant range of values than filtered data in both methods. The distribution of filtered data is more evenly distributed. For the stress data processing is more usable the RFC method than RC method. The means in RFC are distributed more closely to each other than in RC method.

References

[1] Burák J., Semrád K. (2013). Základy navrhovania konštrukcií technických, technologických a energetických zariadení, Letecká fakulta, Technická univerzita, Košice, university textbook, 1st ed., 350 pp.

[2] Downing S. D., Socie D. F. (1982). Simple rainflow counting algorithms, International Journal of Fatigue,Vol. 4, No. 1, pp. 31-40, ISSN 0142-1123, Doi: https://doi.org/10.1016/0142-1123(82)90018-4.

[3] Han J., Moon S., Lee G., Kang D. (2017). Experimental Method for Durability Evaluation of a Chisel Mounted on a Composite Working Implement, Journal of Biosystems Engineering, Vol. 42, No. 4, 1982, pp. 251- 257, eISSN 2234-1862, pISSN 1738-1266, doi: https://doi.org/10.5307/JBE.2017.42.4.251

[4] Hudák J. (2003). Únavové namáhanie oceľových konštrukcií, ManaCon, Prešov, 134 pp., monograph, ISBN 80-89040-20-9.

[5] Poettinger, ploughs SERVO 6.50, Availiable at http://www.poettinger.at/landtechnik/download/servo65_cz.pdf

[6] Rédl J., Páleš D. (2018). Processing of stress dataset with rain-flow counting method, Mathematics in Education, Research and Applications (MERAA), Vol. 4, No. 1, pp. 9 – 17, Slovak University of Agriculture in Nitra, , ISSN 2453-6881, doi: https://doi.org/10.15414/meraa.2018.04.01.9-17

[7] Rychlik I. (1987). A new definition of the rainflow cycle counting method,International Journal of Fatigue, Vol. 9, No. 2, pp. 119-121, ISSN: 0142-1123.

[8] Šesták, J. 2002. Predikcia životnosti rámových konštrukcií: Monografia.(Life prediction of framed structures : Monograph) .1. vyd. SPU Nitra , 2002, s.62. ISBN 80-8069-100-2

Effect of cooling on the performance of a small-scale solar power plant system

Dani RUSIRAWAN[1], Bill A. HAKAMA[1], Ari HADIWINOTO[1],
Muhammad P. N. SIRODZ[1], Liman HARTAWAN[1],
Mohammad A. MAHARDIKA[1], István FARKAS[2]
[1]Department of Mechanical Engineering,
Institut Teknologi Nasional (ITENAS) Bandung, Indonesia
[2]Department of Physics and Process Control,
Institute for Environmental Engineering Systems

Abstract

In this research, the cooling system of the 1 kWp solar power plant have been realized and tested in order to maintain the cell temperature of the PV module. The type of the PV module is monocrystalline silicone. The principle of the PV module cooling is performed by flowing the water, as a cooling medium, on the surface of the PV modules. The cooling system installation is an open cycle system using pumps, reservoirs, hoses and control system based arduino uno, and all this system is installed on the SPP installation. The test was carried out during two days, September 2-3, 2018, starting at 6:00 a.m. until 6:00 p.m. Based on the test, it shown that the efficiency of PV without cooling system is lower than the system with cooling system. It is found also that the average efficiency of PV without cooling was 9.21% with an average cell temperature 32.17 ^{o}C. In other side, the average efficiency of the PV with cooling was 10.64 % with an average cell temperature of 31.34 ^{o}C.

Keywords

crystalline silicone technology, nominal operating cell temperature (NOCT), cooling system, PV efficiency.

1. Introduction

Since the beginning of 2018, a small scale solar power plant (SPP) system has been installed at the campus of ITENAS Bandung, West Java - Indonesia, with geographic location 06°54'S latitude and 107°36'E longitude. The type of the SPP system is grid connected with capacity 1000 Watt peak (1 kWp). The main components of the SPP system consist of a set PV modules (4 pieces @ 265 kWp/PV module) and inverter model UNO 2.0 TL OUTD (Hidayat et al., 2019). The main components of the 1 kWp SPP system (PV modules and inverter) can be seen in the Fig. 1. The PV modules had a 12^{o} tilt referring to the Earth's surface and facing to North.

a)

b)

Figure 1. The PV modules and inverter at small scale SPP

The PV modules technology used is monocrystalline silicone and the inverter is grid tie inverter. A main parameters of the PV module (based on manufacturer catalogue) and inverter specification are shown in Table 1.

Table 1. Main specification of PV modules - Monocrystalline Silicone type JAM6 60-265 and Inverter model UNO 2.0 TL OUTD specifications

PV module electrical parameters			
Reted Maximum Power at STC (W)		265	
Open Circuit Voltage (Voc/V)		38.26	
Maximum Power Voltage (Vmp/V)		31.11	
Short Circuit Current (Isc/A)		9.00	
Maximum Power Current (Imp/A)		8.52	
Modul Efficiency (%)		16.21	
PV module operation condition			
Max. system voltage		DC 1000 V (IEC)	
Operating temperature		-40^{o}C - +85^{o}C	
NOCT (Nominal Operating Cell Temperature)		45 ± 2^{o}C	
Input Inverter specification		**Output Inverter specification**	
Maximum Input voltage (DC)	600 V	Output voltage (AC)	230 V
Input start-up voltage (DC)	100 – 300 V	Output Current Maximum (AC)	12.5 A
Input Current Maximum (DC)	12.5 A	Output Power Maximum	2200 W
Input Power Maximum (DC)	2200 W		

Daily operation data of 1 kWp SPP is monitored by online data logger system (monitoring logger system: VSN300 WIFI Logger Card). At the existing data logger system, the data acquisitions are emphasized on the power (Watt) and energy (kWh). The operation data monitoring results are shown in Figs 2-4.

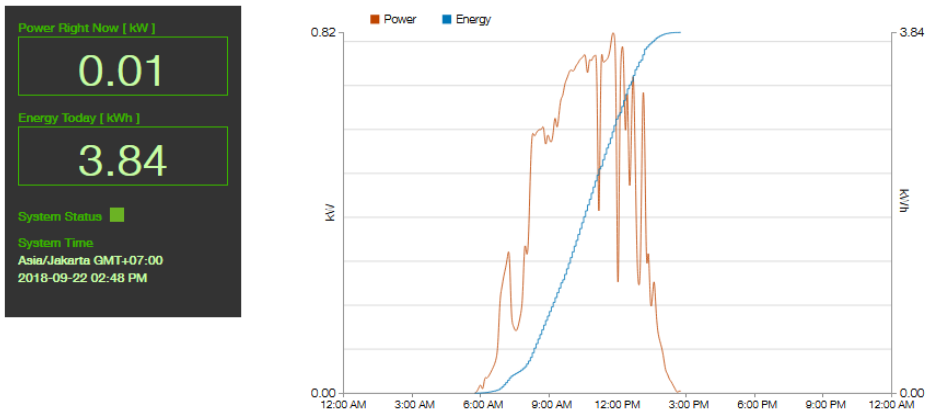

Figure 2. The feature of daily operation of 1 kWp SPP (data for September 22, 2018)

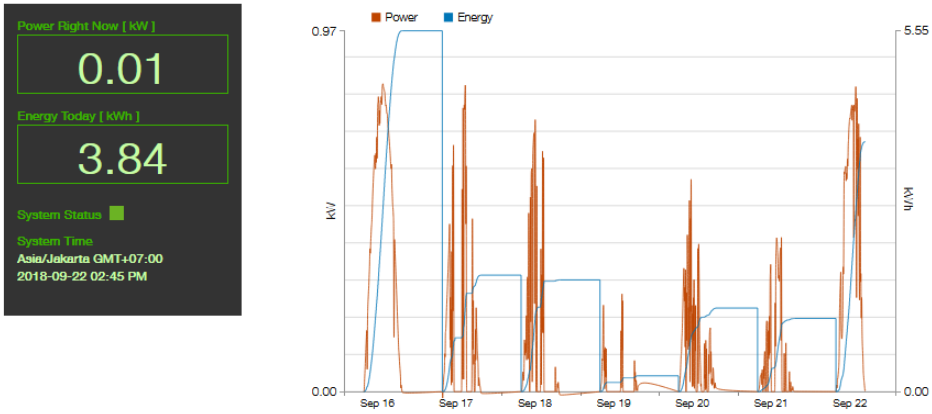

Figure 3. The feature of weekly operation of 1 kWp SPP (data for September 16-22, 2018)

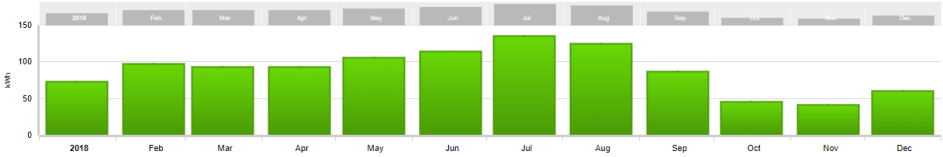

Figure 4. The monthly energy yield over the year 2018 (January – December)

Over the year 2018, the operation of 1 kWp SPS has generated of energy 1.2 MWh. The SPP system was installed on the flat roof one of ITENAS building (Building 1) and at the present used for the lighting the 4th-floor corridor of that building.

As a general characteristics of PV module, in principle increasing of the cell/module temperature at the constant irradiance will affect to the power capability, in this case decreasing of the power (Rusirawan and Farkas, 2011).

Based on daily operation monitoring, sometimes it is found that the temperature ambient in the area of 1 kWP SPP is high and it directly will affect to the cell temperature. Theoretically, there are several correlations related to the ambient and cell temperatures.

It is fact that high operating temperatures of PV cells/modules cause degradation in the performance, especial on the conversion efficiency, significantly (Sato and Yamada, 2019). An effective way to improve efficiency and reduce the rate of thermal degradation of a photovoltaic (PV) module can be done by reducing the operating surface cell/modules temperature (Odeh and Behnia, 2009).

The objectives of this research is realizing and testing of the cooling system on the 1 kWp solar power plant (SPP) installation. The outcome of this research is try to increase the 1 kWp SPP performances (i.e. PV efficiency) by maintain the cell temperature of the PV module.

2. System description of the PV cooling

The PV cooling system has been made and constructed, and basically consisted of the equipment as follow: (1) Temperature sensor, (2) water spray, (3) water reservoir (4) flexible house, and (5) water collector. The schematic diagram of the experimental set-up of the cooling system and the flow and control diagram of the cooling system is shown in Fig. 5.

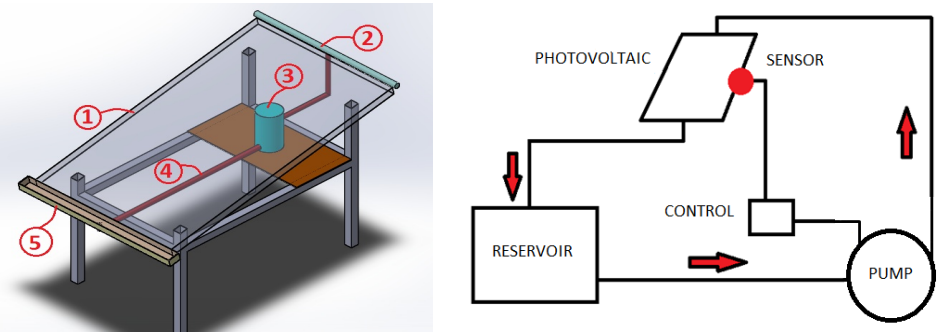

Figure 5. The schematic diagram system and flow - control diagram of the PV cooling system

The control system of the cooling system installed in the 1 kWp SPP installation consists of the following components: arduino UNO, temperature sensor LM35, relay module, water pump, and adapter. Fig. 6 shows a schematic of the control system.

The cooling system installation is an open cycle system using pumps, reservoirs, hoses and control system based arduino UNO. The control system works based on temperature setting. The principle of the pump ON and pump OFF

are created based on higher and upper limit of temperature. In this control system, the temperature is setting between 33-39^{o}.

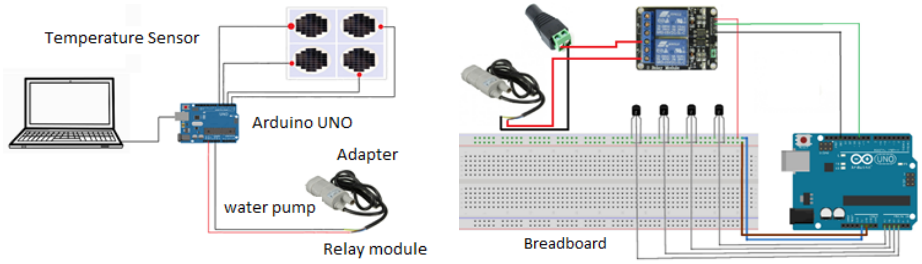

Figure 6. The schematic diagram of the control PV cooling system

In order to check the performance of the control system, the test of the control of the cooling system has been carried out and the results are shown in Figs 7-8.

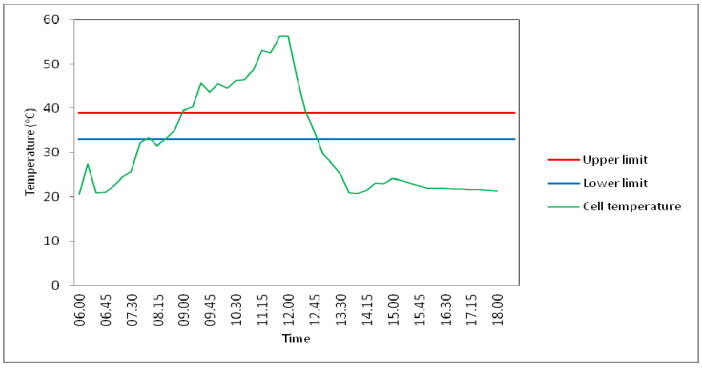

Figure 7. The profile of cell temperature without control system

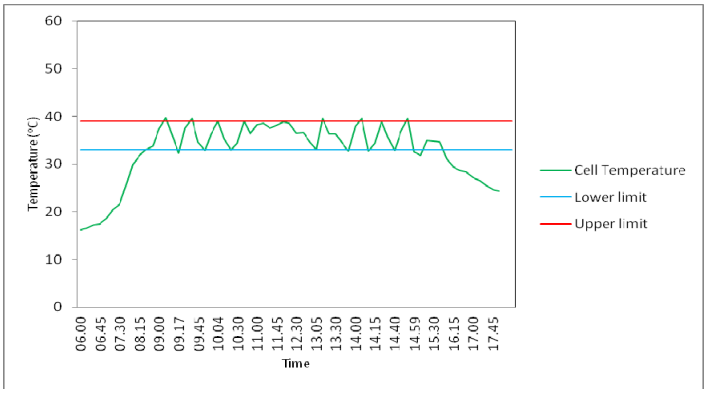

Figure 8. The profile of cell temperature with control system

Based on the profile of cell temperature, it can be shown that the profile of cell temperature with a control cooling system working properly referring to the temperature setting. If the cell temperature reached the upper limit condition the pump ON (work) and circulating the water to cool the PV module temperature, and if the cell temperature decrease until the lower limit condition, the pump OFF (stop).

3. The experimental results

The experiments were performed for two days, September 2-3, 2018, from 6 a.m. to 6 p.m. The objectives of the experiments are to measure the input and output parameters of the 1 kWp SPP, without and with the cooling system, and compare its performances. Figs 9-13 show the relationship all measured parameters during the experiments.

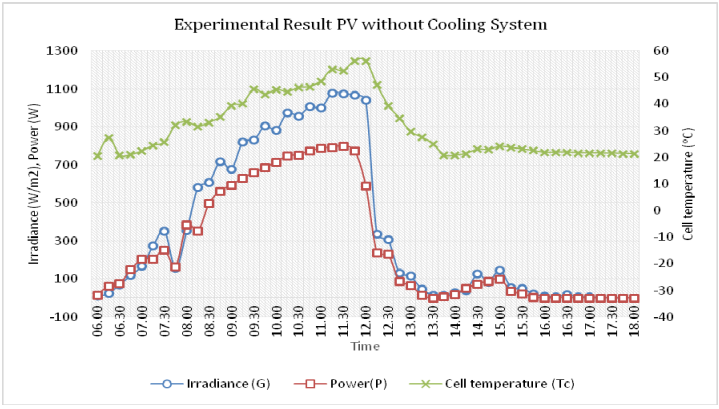

Figure 9. The profile of irradiance and cell temperature without cooling system (Sept. 2, 2018)

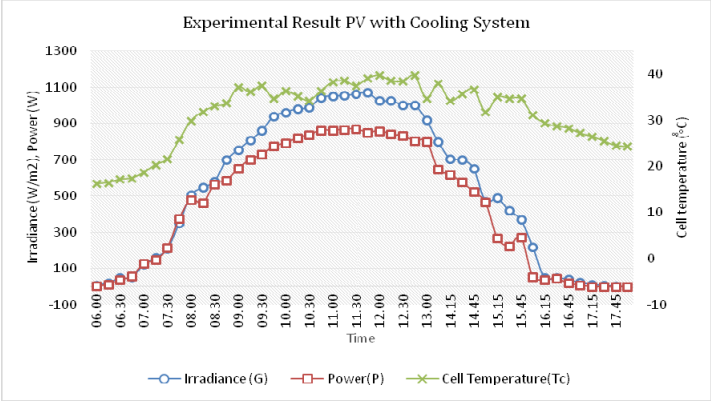

Figure 10. The profile of irradiance and cell temperature with cooling system (Sept. 3, 2018)

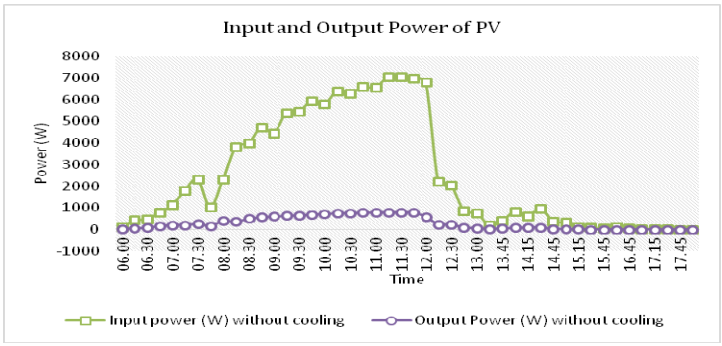

Figure 11. The profile of power of SPP without cooling system (Sept. 2, 2018)

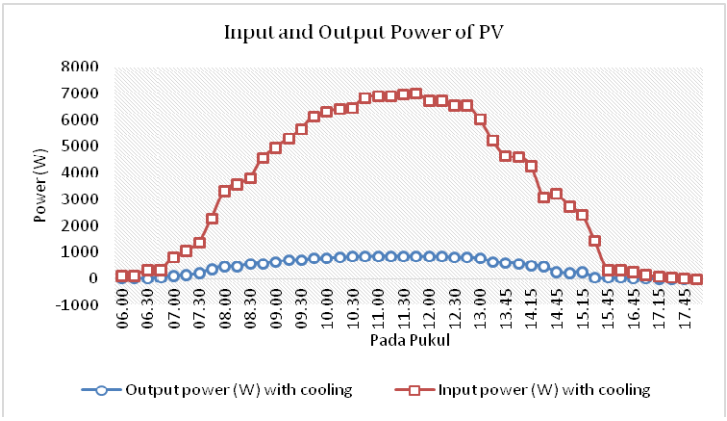

Figure 12. The profile of power of SPP with cooling system (Sept. 3, 2018)

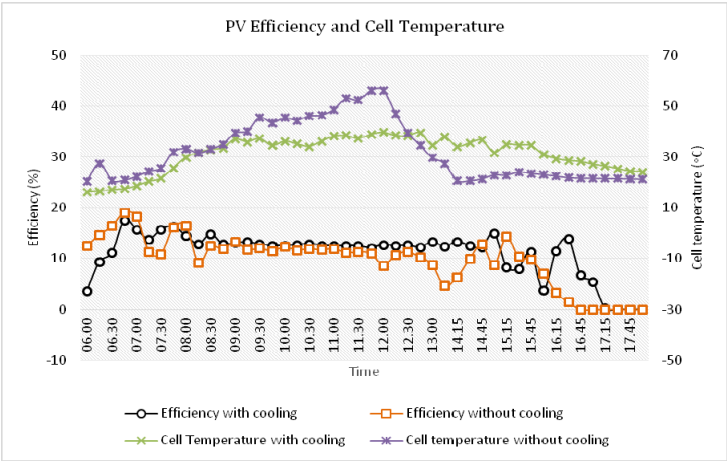

Figure 13. The profile of PV efficiency without and with cooling as a function cell temperature

Figs 9-13 show that there are real benefits by implementing the cooling system on the SPP system. It can be seen clearly that by providing a cooling system, the efficiency of the SPP system increasing significantly. In figure 9, it is found that the cell temperature operation approached to 60 ^{o}C (over the NOCT 45 ^{o}C) especially in peak sun hours (PSH) range (9 a.m. – 2 p.m) and this condition followed by decreasing of the PV power. Based on Fig. 10, the cell temperature during an operation did not exceed 39 ^{o}C, as an upper limit of the temperature control system.

Conclusion

The cooling system has been installed at the 1 kWp SPP at ITENAS campus. The series of test was carried out during two days, September 2-3, 2018, starting at 6:00 a.m. until 6:00 p.m. As the results, it is shown that the efficiency of PV without a cooling system is lower than the system with cooling system. During the test period, the average efficiency and average cell temperature of PV without and with cooling were 9.21% and 10.64%, and 32.17 ^{o}C and 31.34 ^{o}C, respectively. It can be concluded that in conditions of lower temperature or close to NOCT temperature, the PV efficiency tends to increase.

Acknowledgements

This research is carried out with the support of the Ministry of Research, Technology and Higher Education of the Republic Indonesia (Kemenristekdikti) and Institute for Research and Community Services (LPPM) ITENAS through the contract No. 146/B.05/LPPM-ITENAS/VI/2016.

References

[1] Hidayat, F., Rusirawan, D. and Tanjung, I.R.F. (2019): Evaluasi kinerja PLTS 1000 Wp di Itenas Bandung, Elkomika, 7 (1), pp. 195-208.

[2] Odeh, Saad and Behnia, M. (2009): Improving photovoltaic module efficiency using water cooling, Heat Transfer Engineering, 30(6), pp. 499-505.

[3] Rusirawan, D. & Farkas, I. (2011). Simulation of Electrical Characteristic of Polycrystalline and Amorphous PV Modules. EEA Electrotehnica Electronica Automatica, 59(2), pp. 9-15.

[4] Sato, D. and Yamada, N. (2019). Review of photovoltaic module cooling methods and performance evaluation of the radiative cooling method. Renewable and Sustainable Energy Reviews, 104, pp. 151-166.